A BRIDGMAN FURNACE FRONT TRACKING MODEL

UNIVERSITY OF DUBLIN, TRINITY COLLEGE
SCHOOL OF ENGINEERING, MECHANICAL AND MANUFACTURING DEPARTMENT

A thesis submitted to the University of Dublin in partial fulfilment of the requirements for the degree of Ph.D

by

Robin Patrick Mooney, BE, MENG
February 2015

Abstract

A Bridgman Furnace Front Tracking Model

Thesis by   *Project Supervisor*

Robin Patrick Mooney   **Dr. Shaun McFadden**

The Bridgman furnace is widely used in industry and research, mainly because it provides a means to directionally solidify materials in a controlled manner, so that the resulting microstructure, and hence material properties, can be manipulated. This thesis details, firstly, the development and verification of a numerical Front Tracking Model (FTM) to track the position of, and growth conditions at, the columnar front during transient directional solidification in a Bridgman furnace; and, secondly, its application to experiments investigating Columnar to Equiaxed Transition (CET) in a gamma TiAl multicomponent hypoperitectic alloy. Previous FTMs have been applied in fixed grid numerical domains where the solidifying material—normally of hypoeutectic composition—is contained within that domain throughout simulations; the model demonstrated here accounts for movement of material through the domain and is adapted for hypoperitectic solidification. The model is applied, firstly, to characterise a Bridgman furnace in terms of heat transfer coefficients and, secondly, to simulate solidification conditions at, and ahead of, the growing columnar front during a unique set of experiments where Bridgman and power down modes of furnace operation are combined in series. The simulations carried out provide valuable insight, specifically, into the growth conditions that lead to CET in a multicomponent gamma TiAl alloy currently of interest to the aerospace industry; and, more generally, into the dynamics of the transient power down solidification process. The results from this work will be used in preparations for planned directional solidification experiments, using a similar gamma TiAl multicomponent alloy, on-board the European Space Agency MAXUS-9 sounding rocket (in microgravity) where a power down technique is employed. The model can be applied elsewhere, in industry and research, to provide insight into solidification conditions occurring in existing Bridgman processes and in the design of new furnaces.

A wise man begins in the end; a fool ends in the beginning.

Declaration

I declare that this thesis has not been submitted as an exercise for a degree at this or any other University and it is entirely my own work.

I agree to deposit this thesis in the University's open access institutional repository or allow the Library to do so on my behalf, subject to Irish Copyright Legislation and Trinity College Library conditions of use and acknowledgement.

Signature: _____   Date: 4th February 2015

Summary

The 'Bridgman' furnace is widely used in industry and research to directionally solidify pure materials and alloys. The Bridgman process (for alloys) involves movement of the material through a tubular furnace consisting of hot and cold zones that are separated by a baffle or adiabatic gap. The hot zone is held at some temperature above the alloy liquidus, and the cold zone at some temperature below the alloy solidus, so that the material solidifies in a controlled manner in the space between. The sample is typically pulled through the furnace at a fixed rate to give steady solidification in a fixed temperature gradient (traditional 'Bridgman' mode); in this case, pulling rate changes can invoke transient solidification. In the Bridgman furnace 'power down' mode, the sample is stationary and the temperature of hot and cold zones is decreased at a fixed cooling rate. Steady solidification is achieved where both zone temperatures are decreased at the same cooling rate; transient solidification is achieved by applying different cooling rates in each zone.

The overall objective of this thesis has been to gain a better understanding of the solidification conditions, in particular, growth rate and temperature gradient, leading to Columnar to Equiaxed Transition (CET) in directionally solidified castings of gamma titanium alloys (TiAl) using a Bridgman furnace apparatus through mathematical modelling. Currently, TiAl alloys have the potential to replace nickel superalloys in the aerospace and automotive industries on account of their comparatively low density (≈50%) and equivalent strength and stiffness properties at high temperatures. Applications for TiAl alloys include: aero-engine turbine blades, turbocharger rotors and high performance engine valves. CET is an unwanted phenomenon that can occur in castings that adversely affects mechanical properties of cast components. Knowledge of the conditions that lead to CET in castings is therefore imperative. Experimental data for a TiAl multicomponent hypoperitectic alloy, directionally solidified in a Bridgman furnace procedure that involved transient Bridgman and transient power down modes of solidification (in series), was provided to the author of this thesis (by others) for the purposes of numerical modelling. Given this data, the overall thesis objective was broken down into five more manageable sub-objectives.

The first objective was to develop a numerical model suitable for transient Bridgman furnace solidification using an established Front Tracking Model (FTM) from the literature. A FTM refers to a numerical model that estimates and follows the growth of a solidification interface or grain envelope. A suitable FTM was adapted accordingly for transient Bridgman solidification where columnar growth of a hypoeutectic alloy was tracked. A hybrid 1-dimensional axial heat flow model, appropriate for low Biot number processes (<0.1), was numerically implemented that accounts for radial heat flow at the sample circumference. The approach is advantageous since the temperature profile is not assumed *a priori*. Two simulations were performed: the first demonstrated a method for estimating the starting temperature profile and columnar front position in a Bridgman experiment, and the second simulation showed the evolution of the temperature profile and front position over time as two step changes in pulling rate were applied.

The second objective was to verify the numerical model with an analytical model from the literature. Verification was achieved for the case of steady Bridgman solidification of a pure material (in this case pure titanium). Verification for transient Bridgman solidification of an alloy was not possible due to a lack of analytical models in the literature. The simulation results showed that the numerical model was first order accurate in space.

The third objective was to characterise a real Bridgman furnace apparatus in terms of heat transfer coefficients. The model was implemented in series with a discrete Proportional Integral Derivative (PID) controller to solve an inverse heat transfer problem using experimental data from static Bridgman furnace experiments performed with a hypoperitectic TiAl alloy. The model was adapted, in terms of latent heat release, for hypoperitectic growth. Simulation results showed that the furnace heat transfer coefficient at the sample circumference varied with axial position. The method applied is useful to other experimentalists, and to industry, since it avoids the difficult task of calculating heat transfer coefficients in the traditional manner where uncertainty exists in estimating the thermal emissivity values for the surfaces exchanging radiated heat. Further simulations were performed using the results without the PID controller to corroborate the method.

The fourth objective was to model unique experiments carried out in the same furnace where the transient 'Bridgman' and transient 'power down' modes were used in series to directionally solidify the same alloy at four different cooling rates. The model was used to simulate these experiments; one of which displayed CET in the sample microstructure; the others displayed 'axial' columnar to 'radial' columnar transition microstructures. Radial growth is an unwanted occurrence in CET experiments that tends to choke the undercooled region preventing the possibility of CET.

The fifth objective was to explain these microstructural observations using the model. The solidification conditions at the location of CET were estimated, namely; temperature gradient, growth rate, undercooling and undercooled region width. Comparisons were made with the other results. The simulation results highlight an important consideration for CET experiment designers; conditions that favour CET, e.g., low temperature gradient, also support radial columnar growth which can eliminate the possibility of CET. Reversal of radial heat flow at the sample circumference is proposed as a precursor for radial columnar growth.

A discussion is provided that focuses on a sensitivity analysis of dendrite kinetics. The model is practically insensitive to changes in the growth kinetics parameters in terms of temperature gradient and growth rate. However, columnar dendrite tip undercooling is substantially effected. It is concluded that a CET prediction criterion based on undercooling is preferable to one based on growth rate for transient directional solidification. Convection in the melt is not treated in the current model; however, it is considered as a logical next step in its development. Potential improvements to dendrite kinetics in the model are suggested, amongst others. The numerical results, contained herein, will be used in preparation for microgravity experiments on-board the European Space Agency MAXUS-9 sounding rocket, planned for launch in 2016, investigating CET in TiAl alloys.

Acknowledgements

I would like to sincerely thank my supervisor, Assistant Professor Shaun McFadden, for his helpful guidance and support throughout this work. Shaun is an excellent supervisor. I would also like to thank Dr. Marek Rebow of Dublin Institute of Technology, and Dr. David Browne of University College Dublin, for offering their expert knowledge and opinion upon request.

Thank you to my family, specifically to my parents, Maggi and Paraic, for their much appreciated assistance and encouragement. Finally—and most importantly—I would like to thank my wife, Victoria, for her continuous support and attention since the beginning of this work.

I dedicate this thesis to my 1-year old son, Mason, and new-born daughter, Daisy.

Preface

The work described in this thesis has been carried out by the author under the supervision of Dr Shaun McFadden in the School of Engineering at Trinity College Dublin. This work has been completed with financial assistance from the European Space Agency PRODEX programme, as part of the project: GRADECET (GRAvity DEpendence of Columnar to Equiaxed Transition in TiAl alloys). This work began on the 1st October 2010. The research described herein is original. The work of others has been drawn upon in places throughout the thesis, where this is so, acknowledgement is given to those other authors by way of reference. Some of the original material contained herein has already been published (or is submitted for publication). A list of these articles is given in the 'Published Work' section.

In accordance with Section 1.34.3 of the University of Dublin, Trinity College Calendar: Part II, this work has been written as a '*Thesis by Publication*'. That is, published work by the author—carried out whilst the author was on the PhD register at the University—is fully integrated into the body of the thesis. Chapter 1 gives the thesis introduction. Chapter 2 is a review of relevant literature. Chapter 3, Chapter 4 and Chapter 5 have been individually published; whilst Chapter 6 has been submitted for publication. At the beginning of these main chapters, the publication upon which the chapter is based is cited accordingly. Each main chapter contains its own method, results and discussion section. Chapter 7 contains a discussion (currently accepted for publication) and Chapter 8 provides final conclusions and suggestions for future work.

Table of Contents

List of Figures

List of Tables

Nomenclature

A	cross sectional area [m^2]
b	dendrite growth rate undercooling exponent [–]
Bi	Biot Number [–]
c	specific heat capacity at constant pressure [J/kg·°C]
C	dendrite growth rate coefficient [m/s·°C^b]
C_0	original alloy composition [wt.%]
C_{tip}	composition of the liquid at the tip [wt.%]
d	captured volume of mush in a control volume [m^3]
D	derivative controller signal [–]
D_{solute}	diffusivity of solute in the liquid [m^2/s]
e	error [°C]
E	latent heat generated per unit volume [W/m^3]
f	heat flow [W]
F	radiation view factor [–]
g_S	volumetric solid fraction [–]
G	temperature gradient [°C/m]
G_C	concentration gradient [wt.%/m]
h	heat transfer coefficient [W/m^2·°C]
H	enthalpy [J]
I	integral controller signal [–]
I_{ex}	equiaxed index [m^2·°C]
k	thermal conductivity [W/m·°C]
k_{part}	partition coefficient [–]
K_c	controller gain [–]
ℓ	domain length [m]
L_A	adiabatic zone length, or baffle thickness [m]
L_{char}	characteristic length [m]
L_M	latent heat of fusion per unit mass [J/kg]
L_{mol}	molar latent heat of fusion [J/mol]
L_V	latent heat of fusion per unit volume [J/m^3]
m_l	alloy liquidus slope [°C/wt.%]
n	order of numerical error [–]
N	low pass filter variable [–]
N_{CVs}	number of control volumes [–]
NE	numerical error [°C]
p	perimeter [m]
p_o	observed order of accuracy [–]
P	proportional controller signal [–]

Pe, Pe_T thermal Péclet number [–]

Pe_C solutal Péclet number [–]

q heat flux [kW/m^2]

Q heat flow [W]

r radius [m]

R dendrite tip radius [m]

$\Re$ molar gas constant, 8.314 [J/mol·K]

t time [s]

T temperature [°C]

u pulling rate [m/s]

U_b bulk undercooling [°C]

v growth rate [m/s]

V volume [m^3]

V_α growth velocity of peritectic α-phase [m/s]

x axial position, or Cartesian abscissa [m]

x' axial position with respect to the columnar dendrite tip [m]

X dimensionless axial position [–]

y Cartesian ordinate [m]

α thermal diffusivity [m^2/s]

γ solid–liquid interface energy [J/m^2]

Γ Gibbs–Thomson coefficient [m·K]

$\Delta\ell$ elemental volume thickness [m]

ΔS_f^m molar entropy of fusion [J/mol·K]

Δt numerical time step [s]

ΔT bath undercooling [°C]

ΔT_C solutal undercooling [°C]

ΔT_K kinetic undercooling [°C]

ΔT_R curvature undercooling [°C]

ΔT_T thermal undercooling [°C]

ΔT_{tip} dendrite tip undercooling [°C]

Δx control volume thickness [m]

Δy control volume height [m]

ε crystalline anisotropy strength [–]

λ refinement ratio [–]

μ_K attachment kinetics coefficient [m/s·°C]

ξ_C function of solutal Péclet number [–]

ρ density [kg/m^3]

σ Stefan–Boltzmann constant, $5.6703732 \times 10{-8}$ [W/m^2·K^4]

σ^* dendrite tip stability parameter [–]

τ_D derivative time constant [s]

τ_I integral time constant [s]

Ω_C solutal supersaturation [–]

Ω_T thermal supersaturation [–]

$\in$ thermal range [°C]

Sub-scripts

1	at the sample axis, or baffle boundary (when used as subscript to x)
2	at the sample crucible boundary, or baffle boundary (when used as subscript to x)
3	at the exposed crucible wall
4	at a reference position
5	at the heater (or crystalliser) surface
a	advancement
adv	advection
c	conduction (net)
cru	crucible
C	cold zone
CV	control volume
e	east face
euc	eutectic
exp	experimental
H	hot zone
i	spatial label
j	element label in a multicomponent alloy
l	liquidus
L	liquid
m	melting
nuc	nucleation
per	peritectic
rad	radial
s	solidus
S	solid
sim	simulated
t	thickening
tip	dendrite tip
w	west face
x	axial direction
∞	infinity (far away)

Super-scripts

ord	order

m	temporal label
num	numerical
p	iteration index

Published Work

Journal Articles

R. P. Mooney, U. Hecht, Z. Gabalcová, J. Lapin, and S. McFadden, "Directional solidification of a TiAl alloy using a combined Bridgman & power down technique," 2014. (Submitted.)

R. P. Mooney and S. McFadden, "Order verification of a Bridgman furnace front tracking model in steady state," *Simulation Modelling Practice and Theory*, vol. 48, pp. 24–34, 2014.

R. P. Mooney, S. McFadden, Z. Gabalcová, and J. Lapin, "An experimental–numerical method for estimating heat transfer in a Bridgman furnace," *Applied Thermal Engineering*, vol. 67, no. 1–2, pp. 61–71, 2014.

R. P. Mooney, S. McFadden, M. Rebow, and D. J. Browne, "A Front Tracking Model for Transient Solidification of Al–7wt%Si in a Bridgman Furnace," *Transactions of the Indian Institute of Metals*, vol. 65, no. 6, pp. 527–530, 2012.

Conference Proceedings

R. P. Mooney and S. McFadden, "Sensitivity analysis of dendritic growth kinetics in a Bridgman furnace front tracking model," in *4th International Conference on Advances in Solidification Processes*, 2014.

R. P. Mooney and S. McFadden, "The Role of Verification in Computer Modelling: A Case Study in Solidification Processing," in *31st International Manufacturing Conference*, 2014, pp. 173–180.

J. Lapin, Z. Gabalcová, U. Hecht, **R. P. Mooney**, and S. McFadden, "Columnar to Equiaxed Transition in Peritectic TiAl Based Alloy Studied by a Power-Down Technique," *Materials Science Forum*, vol. 790–791, pp. 193–198, 2014.

R. P. Mooney and S. McFadden, "An investigation into Bridgman furnace solidification," in *30th International Manufacturing Conference*, 2013, pp. 375–383.

R. P. Mooney, S. McFadden, M. Rebow, and D. J. Browne, "A front tracking model of the MAXUS-8 microgravity solidification experiment on a Ti-45.5at.% Al-8at.%Nb alloy," *IOP Conference Series: Materials Science and Engineering*, vol. 27, no. 1, p. 12020, 2012.

R. Mooney, D. Browne, O. Budenkova, Y. Fautrelle, L. Froyen, A. Kartavykh, S. McFadden, S. Rex, B. Schmitz, and D. Voss, "Review of the MAXUS 8 sounding rocket experiment to investigate solidification in a Ti-Al-Nb alloy," in *European Space Agency, (Special Publication) ESA SP*, 2011, vol. 700 SP, pp. 453–458.

Chapter 1

Introduction

In this chapter the Bridgman furnace is introduced, its operation explained in detail, and examples of its applications in industry and in research are given. Particular focus is given to examples of the Bridgman furnace in research. The thesis aims and objectives are outlined. This is followed by a description of the thesis chapter structure in the context of the aims and objectives given.

1.1 The Bridgman Furnace

1.1.1 Origin, history, and operation

The 'Bridgman Furnace' takes its name from the 1946 Nobel Prize winning Physicist; Percy W. Bridgman. In the 1920's, Bridgman developed a technique of lowering a cylindrical crucible at a fixed rate along the axis of a vertical tubular furnace, held at a fixed temperature, to produce single crystal materials [1]. The technique was later modified by Donald C. Stockbarger, in the 1930's, to produce large single crystals of lithium fluoride [2], where a high temperature gradient was required for successful growth. To achieve higher gradients, a second tubular heat sink is employed, separated from the furnace heater by a thin annular baffle. The resulting solidification procedure is known as the Bridgman-Stockbarger technique, Bridgman solidification, or the Bridgman method. Many variations of the original set-up have since been developed, however, the principle of operation has remained the same.

Figure 1.1 shows a schematic of a typical Bridgman furnace with the characteristic temperature profile in the sample material. The arrangement allows for solidification to occur primarily in one direction (in this case, in the direction of the sample axis), and in a positive temperature gradient, i.e., $dT/dx>0$. Any such procedure can be referred to as directional solidification. The material, contained in a crucible or ampoule, is lowered through the furnace from the hot zone into the cold zone at some pulling rate, u. The heater is maintained at a temperature, T_H, above the equilibrium liquidus temperature for the material, T_l; and the heat sink is held at a temperature, T_C, below the material equilibrium solidus temperature, T_s. The heater and heat sink are separated by a baffle of thickness, L_A, thereby establishing a temperature gradient in the material, $\sim (T_H{-}T_C)/L_A$. The key advantage of the method is that solidification can be performed in a controlled manner by adjustment of the either temperature gradient or pulling rate (or both).
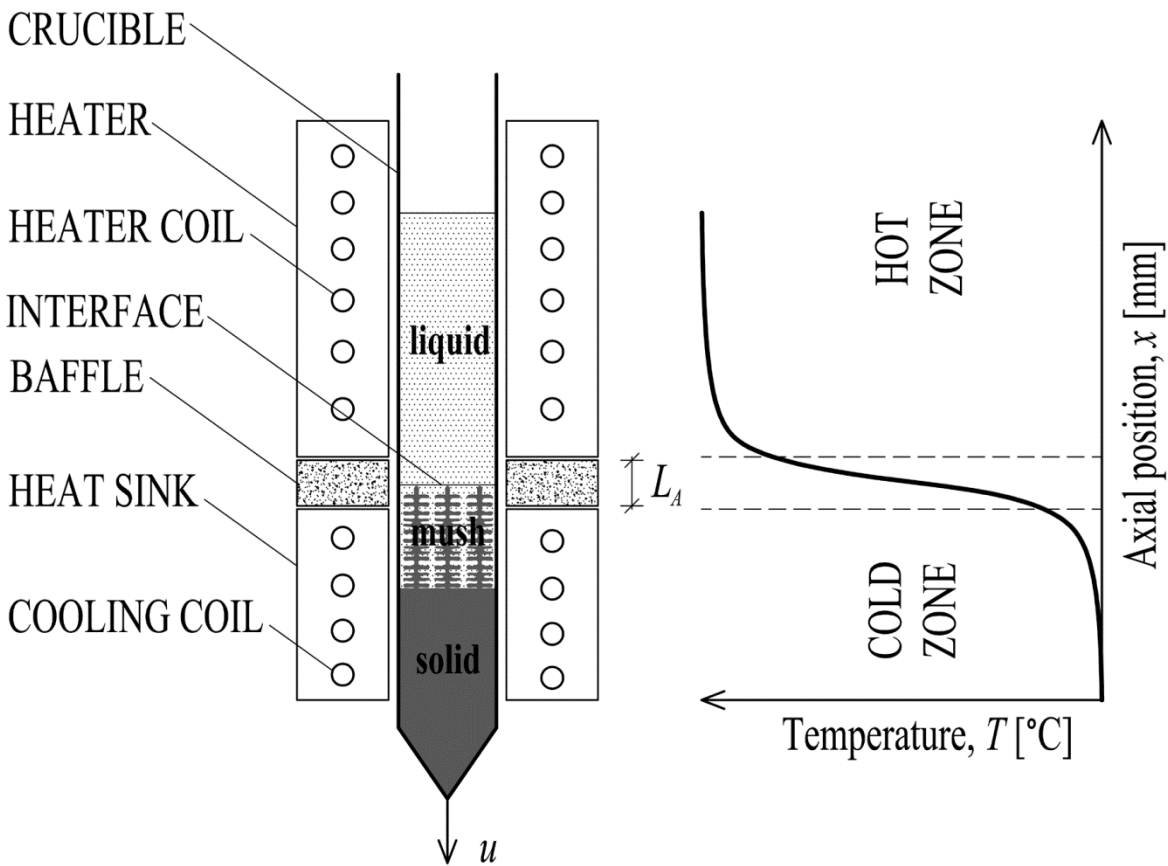
Fig. 1.1 Schematic of a typical Bridgman furnace and temperature profile.

When very large temperature gradients are required, the heat sink is sometimes achieved by surrounding the crucible in a liquid metal bath or via water cooling methods. The size of the temperature gradient in the sample is adjusted by changing the baffle thickness, L_A, or by varying the heater temperature, T_H, and heat sink temperature, T_C, appropriately.

Where it is desirable to grow a single crystal, the crucible usually has a sharp pointed bottom. In pure materials, normally a planar (flat) solid–liquid interface forms. With alloys, however, the solidification interface can take on a planar, cellular (curved) or dendritic (treelike) shape; the latter of which is most common [3]. In dendritic solidification the material forms a 'mushy' zone (a combination of solid and liquid). The directional solidification occurring in the figure is typical for that of an alloy, i.e., the fully solid part of the sample is separated from the fully liquid part by a mushy region made up of dendritic solid and interdendritic liquid [4]. The interface in the figure is given by the mush–liquid boundary. During steady growth, the interface forms somewhere between the hot and cold zones and moves at the same rate (but in the opposing direction) as the pulling rate.

The Bridgman furnace can be used in 'power down' mode to achieve directional solidification. This is similar to the Bridgman method, however the sample is not translated through the furnace, rather the sample is fixed and controlled cooling is applied to the sample by adjustment of the heater and heat sink temperatures. In this case, steady solidification is difficult to achieve. The process is inherently transient in nature unless a fixed temperature gradient can be maintained

2

at the interface; in other words, the cooling rate applied by the heater must equal the cooling rate applied by the heat sink for steady growth to occur.

1.1.2 Applications in industry

The Bridgman method can be used to produce single crystal materials; via careful crucible design or alternatively, by placement of a seed crystal at the crucible tip [5]. By 'single crystal' (or mono-crystal) it is meant that the entire material sample is made up from one continuous crystal lattice throughout; there are no grain boundaries. Careful control of the cooling process, possible using the Bridgman method, can ensure that the crystal lattices align and solidify. Such materials benefit from exceptional properties that are desirable for use in industry. The most common application is in the semiconductor industry where single crystal silicon is used in the production of microprocessors and wiring where extremely low electrical and thermal resistance is desirable. Silicon mono-crystals are widely used in the photovoltaics industry where the material is used to maximise energy conversion efficiency in solar panels [6]. Single crystal lithium fluoride is used in the optics industry (for UV transmission windows) and also in X-ray detectors, on account of its transparency to shortwave ultra-violet radiation [7]. It is possible to cast some alloys (nickel-based superalloys, or titanium alloys) using the Bridgman method as single crystals, for example, in the manufacture high pressure turbine blades. The resultant casting offers superior resistance to creep needed to endure the harsh centrifugal forces of the application at high temperature [8].

Bridgman solidification can be effective in metal purification [9]. This is because most impurities are more soluble in the liquid phase than in the solid phase, therefore, the solidification front pushes the impurities out into the liquid melt during growth. The solidification procedure is carried out a number of times, each time the top section of the sample (containing all the impurities) is cut off before repeating the procedure.

1.1.3 Applications in research

Experiments with transparent materials

In 1965 Jackson and Hunt first published details about experiments on transparent compounds as analogues for freezing metals [10]. Using the Bridgman method they observe that the existence of transparent materials provide an opportunity to make direct observations of the phenomena that determine the structure of cast metals. For example, it was previously impossible to examine criteria for dendrite growth kinetics by direct observation.

Twenty years later, Sato, Kurz, and Ikawa [11] presented results from direct observations, of a similar experiment, using transparent succinonitrile–camphor alloys. They set out to achieve a quantitative evaluation of secondary dendrite arm detachment during directional solidification. It is found in this study that detachment of secondary dendrite arms occurs more easily for higher growth rates, and for high concentrations of camphor. At high growth rates the secondary dendrite arm diameter tends to decrease and hence facilitate detachment. High concentrations of solute gives

larger values of dendrite tip undercooling leading to thinner arm necks; a condition favourable for dendrite detachment.

The relationship of growth rate and primary dendrite arm spacing was investigated by Ding et al. [12] using ethanol and acetone transparent alloys of succinonitrile. The effect of step increments in growth rate (with a fixed temperature gradient), and changes in temperature gradient (at a fixed growth rate) are examined in this study. It is determined that primary dendrite arm spacing is heavily dependent on growth rate and temperature gradient, and that the historical values for these parameters have a major influence on the resulting arm spacing. In other words, the transient effects of varying the pulling rate or temperature gradient are notable.

A combined experimental–numerical study was performed by Simpson et al. [13] where convection in the melt is considered for growth of pure succinonitrile in a Bridgman furnace. Digital cameras are employed to observe planar growth and flow paths due to convection using suspended particles in the melt. The solid–liquid interface shape and velocity are measured which compares well with two and three dimensional numerical models.

Transparent material experiments using the Bridgman method have more recently been carried out in microgravity environments where convection effects in the melt are absent. Bergeon et al. [14] and Weiss et al. [15] give detailed accounts of a Bridgman solidification experiment using succinonitrile alloys carried out on the International Space Station (ISS) where three dimensional spatio–temporal evolution of solidification is observed. The aim of this experiment was to provide unique benchmark data for validation of numerical phase field models, and also to describe the physics of interface pattern selection, and to determine the criteria that govern planar to cellular, and cellular to dendritic transitions.

Recently, studies by Mogeritsch and Ludwig [16][17][18] describe in-situ observations of a peritectic transparent organic material during solidification in an experimental micro-Bridgman furnace. Interphase spacing of the α and β peritectic phases is measured as a function of growth velocity for a fixed composition, and as a function of composition for a fixed growth velocity.

Experiments with aerogel crucibles

The development of aerogel crucibles was first introduced by Alkemper [19]. Aerogels are unique materials; they are transparent to visible light (especially at the infrared end of the light spectrum [20]), and have an extremely low thermal conductivity, around 0.02 W/m·°C. This material offers the possibility to observe solidification of metals in real-time by seeing through the mould and recording the solidification process on a charged-couple device (CCD) infrared camera. Alkemper later carried out directional solidification experiments on Al–Ni and Al–Si metal alloys [21] using a 'power down' method of cooling.

Experiments with x-ray videomicroscopy

Mathiesen and Arnberg [22] have taken a major step further into the observation of the solidification process using the Bridgman method. Experiments were carried out at the European Synchotron Radiation Facility (ESRF) where samples of Al–30wt.%Cu were directionally solidified whilst undergoing high resolution fast acquisition x-ray imaging. Using this method, it was possible to examine the microstructure evolution and local liquid constitution during solidification through a 2-dimensional field of view (1.35×1.35 mm^2) at intervals of 0.45 s. The images were further analysed to extract information about interface morphology, dendrite tip growth rate at the solid–liquid interface and constitutional undercooling at the dendrite tip. Whilst steady dendrite growth is not realised in these experiments, they highlight the advantages of using x-ray radiography in understanding solidification phenomena, as well as providing important modelling data for dendritic growth models.

Using the same technique, a subsequent study [23] focuses on observations of dendritic fragmentation resulting from local solute enrichment during the directional solidification of Al–20wt.%Cu. It is found that the accumulation of solute at the root of tertiary dendrite arms can lead to a decrease in melting temperature of the solid–liquid interface, consequently resulting in remelting of the arm leading to detachment, i.e., fragmentation. This phenomenon is important in understating the problem of columnar to equiaxed transition (CET) in castings.

More recently, further work [24] has been done using x-ray radiography to investigate coarsening in the mushy zone in Bridgman solidification of Al–30wt.%Cu. In this study, secondary dendrite arm spacing (SDAS) is measured during acceleration and deceleration of the solidification front. The observations show that the proximity of primary dendrites does not affect SDAS during deceleration of the solidification front. On the contrary, during accelerations of the solidification front secondary dendrite arms coarsened more, and were more likely to produce tertiary dendrite arms.

A study by Reinhart et al. [25] was carried out where unrefined Al–3.5wt.%Ni and boron refined Al–5wt.%Ti–1wt.%B alloys were solidified in a vertical Bridgman furnace. In situ real-time imaging of the solidification behaviour of thin samples (40 mm in length, 6 mm in width, and 150 μm to 200 μm in thickness) of both materials is obtained by synchrotron x-ray radiography at the ESRF. A sharp jump in pulling rate is applied in order to provoke a CET in the sample. Several key observations in relation to the CET are made, for example; the evolution of undercooling ahead of the columnar tip, and the CET blocking mechanism. Importantly, this study outlines a method to calculate the evolution of nuclei density between successive images for equiaxed growth, a task only possible through x-ray radiography.

Analytical modelling

Chang and Wilcox [26] give an account of a 2-dimensional analytical model, using cylindrical coordinates, for vertical Bridgman furnace solidification where there is no adiabatic zone and

material properties are assumed constant in the liquid and the solid phases. Convection in the melt is assumed negligible. The model assumes a planar growth interface only. Latent heat is accounted for using a 1-dimesional analysis with the Stefan condition applied to solve for interface position. The heat transfer coefficients at both heaters are assumed equal.

Naumann [27] presents a similar model suitable for use with small sample diameters (less than 10 mm) with the addition of an adiabatic zone and separate thermophysical properties for solid and liquid. Naumann further extends this work as a hybrid analytical–numerical 2-dimensional model [28] valid for long thin samples and very low pulling velocities (~100 mm/h) which are suitable for single crystal growth. The effect of adiabatic zone length and curvature of isotherms is analysed.

Gandin, Schaefer and Rappaz [29] present an analytical model for predicting the growth of a single dendritic grain envelope solidifying in a Bridgman furnace where a fixed thermal gradient and isotherm velocity is assumed. The model is applied in two dimensions. The Kurz Giovanola and Trivedi [30] (KGT) model for dendritic growth is applied giving a quadratic relation of undercooling for growth rate. The model is limited because the growth kinetics are valid for low levels of undercooling, latent heat is assumed negligible, and the model cannot not cope with interactions of the single grain envelope with the mould wall or with another grain.

Numerical modelling

Brown and Kim [31] apply a fully implicit axisymmetric numerical model, to solve for heat transfer, melt convection and species transport in a vertical three zone Bridgman furnace. The purpose of the study is to accurately model crystal growth with a view to reducing radial segregation in the crystals. The model results are compared to experimental data for a dilute Ga–Ge alloy. The stagnant film model [32] and Scheil model [33] for solute transport at the solid–liquid interface are used in this analysis. It is found that the intensity of mixing in the melt has a strong bearing on the level of radial segregation observed.

An experimental study by Neugebauer and Wilcox [34] shows that a booster heater located between the hot zone and the adiabatic zone of a Bridgman furnace can be used to thermally stabilise (or destabilise) the effect of convection depending on the power applied to the booster. It is found that convection effects in vertical Bridgman solidification could be avoided by applying low pulling rates, using dilute alloys, or by operating in a microgravity environment.

Fu and Wilcox [35] use an explicit finite difference numerical scheme to investigate the effect of a sudden change in ampoule pulling rate in a three zone Bridgman furnace study. It is found that the freezing rate depends on three key factors: Biot number, latent heat of fusion, and adiabatic zone length. The numerical results are correlated to determine an equation to estimate the time required for the freezing rate to catch up with the new ampoule pulling rate, i.e., the transient settling time. However, this model assumes that the Stefan condition applies at the solid–liquid interface; so it is not appropriate for dendritic growth (with a mushy zone). Other important

assumptions include: equal heat capacity and density in the liquid and solid, fixed but separate thermal conductivity in the solid and liquid, fixed heat transfer coefficients at the hot and cold heaters, and large length-to-diameter ratio of the sample.

Su, Jemian and Overfelt [36] carried out an experimental study where sudden changes in pulling rate are investigated in Bridgman solidification of Al–Cu alloys. The model of Fu and Wilcox [35] is tested alongside a similar model by Saito and Hirata [37]. It is reported that the latter model is in better agreement with the experiments carried out.

Eiken et al. [38] have carried out a case study of phase field simulations of Bridgman solidification of a Ti–Al–Nb alloy to examine microstructure morphology in early peritectic growth. The effect of varying critical undercooling for growth and adding grain refiners is simulated and compared to experimental data for three different values of aluminium content. The study is considered qualitative given the lack of reliable data for diffusion coefficients in the melt and interfacial energies.

Li et al. [39][40] have carried out a two-part study where a fixed grid front tracking model was applied to Bridgman growth of succinonitrile. The model assumes a planar solidification front. The model considers buoyancy induced convection, applied moving boundary conditions to simulate the heater movement, and assumed fixed but separate thermophysical properties for the solid and liquid phases.

1.2   Thesis Objectives

The work presented in this thesis has been motivated by a need to understand the pertinent solidification conditions that may, or may not, produce a columnar to equiaxed transition in gamma titanium aluminide castings. The author is currently a member of a research group, GRADECET (described later in Section 2.5.2), that shares this motivation. One specific task, imparted by this research group to the author, emerged as follows:

'To numerically model terrestrial Bridgman furnace experiments for directional solidification in a gamma titanium aluminide alloy where the Bridgman method is combined in series with the power down technique; and to provide enlightenment into the experimental results obtained using the model'.

The above task is the overall objective of this thesis; however, it is appropriate to break this task down into several, more manageable, objectives as follows:

1. To develop a numerical model for transient Bridgman furnace solidification that incorporates a front tracking model from the literature.
2. Perform an order verification exercise on the numerical model using an analytical solution from the literature.

3. Characterise the Bridgman furnace experimental apparatus (in terms of heat transfer coefficients) using the numerical model and experimental data.

4. Apply the numerical model to the directional solidification experiments (carried out in the same furnace) where the Bridgman method is combined in series with a power down method.

5. Use the numerical model to explain microstructural observations in the experiment samples and to provide insight into the experiment process.

1.3   Thesis Structure

Chapter 1 introduces the Bridgman furnace and its applications. This is followed by a statement of the thesis objectives. Chapter 2 gives a detailed review of relevant literature. Chapter 3 addresses the first objective of this thesis: to develop a numerical model for Bridgman solidification using a front tracking model from the literature. Chapter 4 addresses the second objective: to perform an order verification exercise on the model. Chapter 5 deals with the third objective: to characterise a Bridgman furnace using the model and experimental data. Chapter 6 addresses objectives four and five: to apply the developed model to directional solidification experiments; and to assess the simulation results in respect of microstructural observations in samples. As mentioned in the preface, Chapters 3, 4, 5 and 6 contain bespoke discussion and conclusion sections; Chapter 7 provides further relevant discussion; and finally, Chapter 8 contains conclusions for the thesis and suggestions for future work.

Chapter 2

Literature Review

In this chapter a review of relevant literature is provided. Firstly, a summary of solidification morphologies commonly occurring in metallic systems is given (in Section 2.1). This is followed by a review of dendritic growth in metallic alloys (in Section 2.2). Eutectic and peritectic alloy solidification is explained (in Section 2.3 and Section 2.4, respectively). Peritectic gamma titanium aluminide alloys are then reviewed (in Section 2.5). This is followed by a detailed look at a front tracking model for dendritic solidification from the literature (in Section 2.6), and a short review of front tracking methods that account for convection (in Section 2.7). The chapter is concluded (in Section 2.8) and the scope of the current work, as part of this thesis, is given (in Section 2.9).

2.1   Solidification Morphologies

The morphology (shape) of the solid–liquid interface during solidification of metallic or non-metallic systems can be categorised into one of three commonly occurring types: planar, cellular, and dendritic, as shown in Fig. 2.1. In each case shown, growth occurs in the positive x-direction and the material temperature, T, is shown by a thick black line. The liquid regions (white areas labelled 'L') have a higher temperature than the solid regions (grey areas labelled 'S'). In other words, growth is occurring in a positive temperature gradient ($dT/dx>0$). This is known as directional solidification [3]. In metallic systems, the shape of the interface is primarily determined by the diffusion of heat and mass.
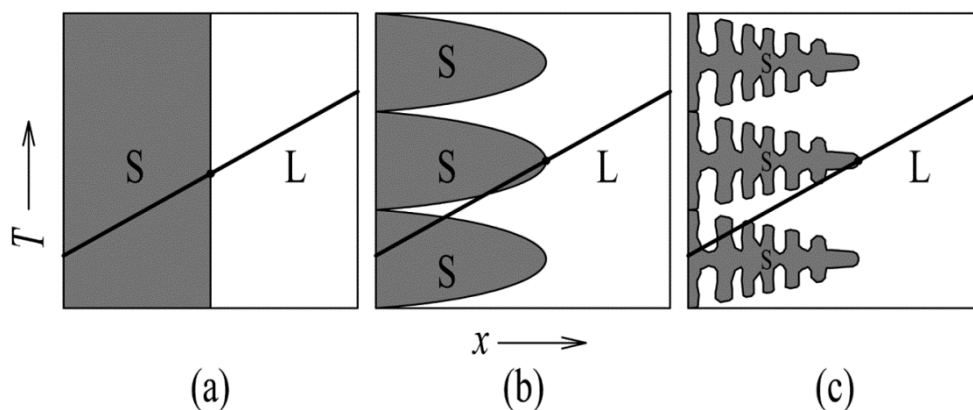
Fig. 2.1 Solid–liquid interface morphologies in directional solidification: (a) planar, (b) cellular and (c) dendritic.

For pure metallic materials, the diffusion of heat controls the interface shape. Pure materials solidify with a planar interface when directionally solidified. A perturbation, i.e., a disturbance in shape, on the planar surface in Fig. 2.1(a) will find itself in liquid hotter than the melting point of the pure material. The perturbation will therefore melt back; in this case, latent heat generated is extracted via the solid. Pure materials can take on a dendritic morphology (not shown here), for example, in the case of a thermal dendrite growing in an undercooled melt, where solidification occurs in a negative temperature gradient and latent heat is extracted via the liquid. Surface perturbations, in this case, find themselves in liquid at a lower temperature than the local solidus temperature of the alloy and therefore can grow (eventually into a dendritic shape).

In alloys, however, the interface morphology is mainly controlled by the diffusion of mass—specifically the diffusion of solute—such that all three interface types in Fig. 2.1 can occur. Tiller et al. [41] were the first to elucidate the link between the diffusion of solute and stability of a planar interface. In their analysis they determine the *constitutional supercooling criterion* to predict the stability of a planar interface in the directional solidification of binary alloys (having a partition coefficient $k_{part} < 1$), as follows:

$$G < m_l G_C \quad , \tag{2.1}$$

where G is the temperature gradient in the liquid, m_l is the slope of the liquidus line from the equilibrium phase diagram for the alloy, and G_C is the concentration (solute) gradient in the liquid. If $G > m_l G_C$ then a planar interface will remain stable, Fig. 2.1(a). If $G < m_l G_C$ then a planar interface is unstable and any perturbation on the planar surface will grow into a dendritic form, Fig. 2.1(c). In this case, the liquid near the interface is *constitutionally supercooled*. (Note that in the literature 'supercooled' is often replaced by 'undercooled' and 'constitutional undercooling' is equivalent to 'solutal undercooling'.) Finally, if $G \approx m_l G_C$, then a cellular interface may form, Fig. 2.1(b), which rapidly leads to dendritic form if G is decreased. Dendritic growth is the most common of the three interface morphologies for metallic alloy systems.

2.2   Dendritic Growth

Dendritic (from the Greek word *dendron*, meaning tree) growth refers to the formation and subsequent growth of treelike primary crystals during the solidification of a material where the solidifying shape is branched like a tree, with primary, secondary and tertiary dendrite arms [42]. The solid–liquid interface for most metallic alloy systems is *atomically rough*. The structure of the liquid phase is similar to that of the solid phase; so atoms in the liquid encounter an abundance of potential bonding sites. This leads to apparent random attachment of atoms during solidification giving a rough and uneven interface at the atomic scale, in other words, non-faceted growth. This occurs when $\Delta S_f^m < 2\,\mathfrak{R}$, where ΔS_f^m is the molar entropy of fusion and $\mathfrak{R}$ is the molar gas constant [3]. In this case, the kinetics of attachment of atoms at the interface is not significant and the shape of the interface is that which maximises the flow of heat and solute, and minimises the

solid–liquid interface energy, γ. The most successful interface shape in this case is dendritic. Two dendritic growth scenarios possible in metallic alloys systems are considered next: dendritic *columnar* growth and dendritic *equiaxed* growth. This is followed by a section dealing with the occurrence of both of these scenarios in a single casting, i.e., *columnar to equiaxed transition*.

2.2.1 Columnar growth

In a given casting, columnar dendrites begin growth at or near the mould wall, nucleating heterogeneously at the mould itself or emanating from chill grains. They grow with a preferred crystallographic direction—opposite to the direction of heat flow—into the liquid melt with a dendritic growth morphology. The latent heat generated (by solidification) is extracted via the solid columnar dendrite, to the mould wall. This can only occur when the temperature gradient at the solid–liquid interface, i.e., at the dendrite tip, is positive, as shown in Fig. 2.2(a). This means that the temperature of the liquid ahead of the columnar dendrite tip is higher than the temperature of the tip itself. Note the direction of the columnar growth rate, v_{tip}, is opposite to the direction of heat flow, Q. The equilibrium liquidus temperature, T_l, is plotted as a function of position, x. At the dendrite tip T_l is reduced, primarily due to local enrichment of the liquid by solute rejected at the tip (solutal undercooling), and secondly due to the capillarity effects given by the curvature of the solid–liquid interface (curvature undercooling). The total difference between the equilibrium liquidus temperature for the alloy and the temperature at the tip is known as the dendrite tip undercooling, ΔT_{tip}. This is the usually the primary driving force for growth in metallic alloys. At temperatures below the equilibrium solidus temperature, T_s, the columnar dendrite is fully solid. Columnar growth is also known as *constrained growth*, since the growth of the dendrites is constrained or fixed by the rate of heat extraction.
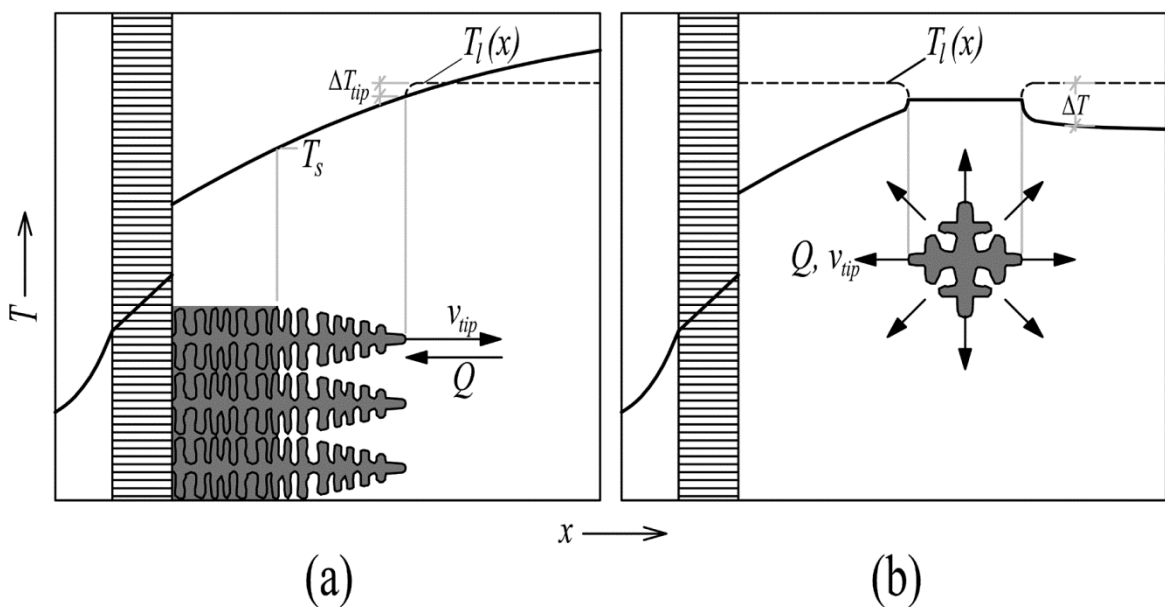
Fig. 2.2 Thermal fields for columnar (a) and equiaxed (b) dendrites in alloys, adapted from [3].
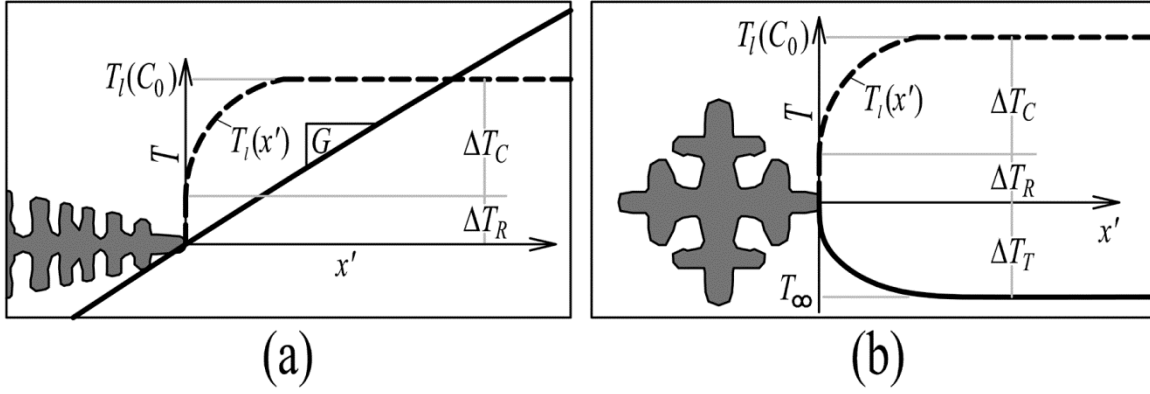
Fig. 2.3 (a) Columnar dendritic growth into a superheated liquid with imposed temperature gradient and (b) equiaxed dendritic growth into an undercooled melt with temperature T_∞.

Analytical modelling

Analytical models of columnar growth focus on steady-state solutions to the solutal diffusion equation from the point of view of an observer fixed at the dendrite tip. Consider the moving coordinate system, with the origin fixed at the dendrite tip, as shown in Fig. 2.3(a), where x' is the position within the moving reference frame. The thermal gradient at the dendrite tip, G, is imposed by the process. The cooling conditions (rate of heat extraction) constrain the growth rate of the dendrite, however, the temperature at which growth occurs is primarily a function of solute rejection and hence alloy composition. Solute is rejected at the tip during growth leading to a snowplough effect of solute so that a concentration gradient exists in the liquid ahead of the tip. This leads to a local decrease of equilibrium liquidus temperature of the liquid at the tip, increasing back to its original value for the alloy of $T_l(C_0)$ at some distance away, as shown in Fig. 2.3(a), where the dashed line shows T_l as a function of x' [9].

The curvature of the tip itself also creates a departure from equilibrium leading to step decrease of the local equilibrium liquidus temperature at the tip. Columnar growth is often considered a solute-diffusion-controlled process given that curvature effect is less significant at low solidification velocities [42], however, both are considered here. The dendrite tip undercooling, ΔT_{tip}, is made up by solutal undercooling, ΔT_C, and curvature undercooling, ΔT_R, such that;

$$\Delta T_{tip} = \Delta T_C + \Delta T_R \quad . \tag{2.2}$$

Considering solutal diffusion only, Ivantsov [43] found a solution to the steady-state diffusion equation for the growth of a dendrite tip having a paraboloid of revolution shape. Critically, this choice of shape is self-preserving during growth. The solution equates the dimensionless solutal supersaturation, Ω_C, to a function of the solutal Péclet number, $Iv(Pe_C)$, known as the Ivantsov function, as follows:

$$\Omega_C = Iv(Pe_C) \quad , \tag{2.3}$$

where $Pe_C=v_{tip}R/2D_{solute}$ is the solutal Péclet number (ratio of solutal advection rate to solutal diffusion rate), R is the dendrite tip radius and D_{solute} is the diffusivity of solute in the liquid, and where $\Omega_C=(C_{tip}-C_0)/(C_{tip}(1-k_{part}))$, C_{tip} is the composition of the liquid at the tip, C_0 is the original binary alloy composition and k_{part} is the alloy partition coefficient (assumed less than unity), and finally the Ivantsov function is defined as,

$$Iv(Pe_C) = Pe_C \exp(Pe_C)E_1(Pe_C) \quad , \qquad (2.4)$$

where $E_1(Pe_C)$ is the exponential integral function. Equation (2.3) can be rewritten in terms of solutal undercooling, ΔT_C, by rearranging for C_{tip} and assuming straight lines for liquidus and solidus on the alloy phase diagram to give,

$$\Delta T_C = \frac{k_{part}(T_l - T_s)Iv(Pe_C)}{1-(1-k_{part})Iv(Pe_C)} \quad . \qquad (2.5)$$

This analysis provides a set of Péclet numbers for a given level of solutal undercooling and, as a result, only pairs of values for growth rate and dendrite tip radius are determined.

The curvature undercooling is given by $\Delta T_R=2\Gamma/R$ where Γ is the Gibbs–Thomson coefficient (the ratio of the solid–liquid interface energy to the entropy of fusion). By substituting this expression and equation (2.5) into equation (2.2) yields the dendrite tip undercooling for columnar growth from the analytical model of Kurz et al. [30]. In this model—known as the KGT model—the authors use the *marginal stability criterion* of Langer and Müller-Krumbhaar [44], where it is assumed that dendrites grow at the critical wavelength of stability for a planar interface. The marginal stability criterion introduces a stability parameter (a constant) σ^* such that; $1/\sigma^*\propto v_{tip}R^2$, in this case $\sigma^*=1/(2\pi)^2$, thus providing a second relationship for growth rate and radius, and thereby permitting the calculation of explicit values of growth rate for any given dendrite tip undercooling. Under the KGT model, the solution to the following quadratic transcendental equation gives the columnar dendrite tip growth rate,

$$v_{tip}^2\left(\frac{\pi^2\Gamma}{Pe_C^2 D_{solute}^2}\right) + v_{tip}\frac{m_l C_0(1-k_{part})\xi_C}{D_{solute}\left[1-(1-k_{part})Iv(Pe_C)\right]} + G = 0 \quad , \qquad (2.6)$$

where m_l is the slope of the liquidus line from the phase diagram, ξ_C is a function of solutal Péclet number (that approaches unity at low Péclet numbers or $\pi^2/k_{part}Pe_C$ at high Péclet numbers), and G is the mean temperature gradient at the interface.

Where this model is to be used as part of a numerical simulation, it is sometimes convenient to pre-calculate a number of growth velocities over a range of undercooling values and fit a power law curve to the results, for example, $v_{tip}=C(\Delta T_{tip})^b$, as demonstrated by Rebow and Browne [45].

2.2.2 Equiaxed growth

Equiaxed growth in metallic alloys occurs from within an undercooled melt. That is, the melt has a temperature lower than the equilibrium liquidus temperature for the alloy. Once nucleation has occurred, an equiaxed dendrite (for cubic metallic systems) grows equally along all six crystallographic axes of the primary phase, hence the term equi-axed. Referring to Fig. 2.2(b), the growth direction in this case is the *same* as the direction of heat flow. Latent heat generated on solidification is transported away from the solid–liquid interface into the undercooled liquid and subsequently to the mould wall through the liquid. The temperature gradient at the dendrite tip must be negative for equiaxed growth. In a similar manner to the case of columnar growth, the liquidus temperature at the dendrite tip is reduced due to solute enrichment and because of capillarity effects. However, since the thermal gradient at the tip is negative, an additional contribution (thermal undercooling) is included in the overall bath undercooling, ΔT. Note that the equiaxed dendrite is isothermal during growth; however the thermal gradient in the liquid is not known *a priori*. Equiaxed growth is also referred to as *free growth* or *unconstrained growth* since the growth rate is limited only by the available undercooling, as opposed to the rate of heat extraction [42].

Analytical modelling

In equiaxed growth, modelling solutal diffusion, capillarity effects *and* thermal diffusion must be considered, since the latent heat generated is transported away from the dendrite tips via the liquid. Consider a moving coordinate system, fixed the tip of a growing equiaxed dendrite, as shown in Fig. 2.3(b). The undercooled melt provides an additional driving force for growth, i.e., thermal undercooling ΔT_T, not seen in columnar growth, such that the total bath undercooling is given by,

$$\Delta T = \Delta T_T + \Delta T_C + \Delta T_R \quad . \tag{2.7}$$

The solution to the thermal diffusion problem is analogous to that of solutal diffusion where the thermal Péclet number, Pe_T, and thermal supersaturation, Ω_T, replace the their solutal counterparts in the Ivantsov solution as follows:

$$\Omega_T = Iv(Pe_T) \quad , \tag{2.8}$$

where $Pe_T = v_{tip}R/2\alpha$ is the thermal Péclet number, α is the thermal diffusivity (ratio of thermal conductivity to volumetric heat capacity), $\Omega_T = (T_{tip} - T_\infty)/(L_V/c_L)$, T_∞ is the far field bath temperature, L_V is the latent heat of fusion per unit volume, and c_L is the specific heat capacity of the liquid. The thermal undercooling, ΔT_T, can then be calculated as,

$$\Delta T_T = \frac{L_V}{c_L} Iv(Pe_T) \quad . \tag{2.9}$$

Lipton et al. [46] demonstrate a model for equiaxed growth in an undercooled melt, known as the LGK model, that combined this result with the Ivantsov treatment of the solutal diffusion problem

14

and capillarity effects—already discussed for columnar growth—to get the following expression for total bath undercooling:

$$\Delta T = \frac{L_V}{c_L} Iv(Pe_T) + m_l C_0 \left\{ 1 - \frac{1}{1-(1-k_{part})Iv(Pe_C)} \right\} + \frac{2\Gamma}{R} \quad . \tag{2.10}$$

This equation fails to yield distinct values for growth rate and dendrite tip radius; rather, only pairs of their product are available by its solution. The LGK model applies the marginal stability criterion to give the following expression for dendrite tip radius,

$$R = \frac{\Gamma / \sigma^*}{\dfrac{Pe_T L_V}{c_L} - \dfrac{Pe_C m_l C_0 (1-k_{part})}{1-(1-k_{part})Iv(Pe_C)}} \quad , \tag{2.11}$$

where σ^* is introduced as the stability criterion parameter, equal to $1/4\pi^2$ (when using the marginal stability criterion). For a given value of bath undercooling, equation (2.10) and equation (2.11) can be solved using a numerical iteration method to determine explicit values for the growth rate and dendrite tip radius.

2.2.3 Columnar to equiaxed transition (CET)

In most castings either a columnar or equiaxed grain structure occurs. Sometimes, however, both columnar and equiaxed grain structures can be observed. This important phenomenon is known as columnar to equiaxed transition (CET). A CET is said to occur when the progress of constrained (columnar) grain growth is blocked by the nucleation and subsequent growth of unconstrained (equiaxed) grains [9]. Figure 2.4 shows an image of a CET in an aluminium–silicon alloy (Al–7wt.%Si), taken from a directional solidification study by Gandin [47]. The elongated columnar grains on the left hand side of the image are distinctive from the equiaxed grains on the right hand side. A detailed account of theory and models for CET is given by Spittle [48].

Fig. 2.4 Columnar to equiaxed transition visible in a longitudinal section of a cylindrical sample (70 mm in diameter and 150 mm in length) of Al–7wt.%Si [47].

15

Fully columnar or fully equiaxed grain structure is normally desired in completed cast components so that consistent mechanical properties are achieved throughout the casting. For example, castings with a columnar grain structure are used in directionally solidified turbine blades in order to reduce creep at high temperatures. Whereas, fully equiaxed cast components are used in applications where strength is important, to improve feeding, or reduce the possibility of hot tearing. It is therefore vital to understand the conditions that produce a CET in order to avoid it as necessary.

Theories for the origin of equiaxed growth

Hutt and St John [49] reviewed several theories regarding the mechanism by which equiaxed grains form and lead to a CET in castings.

The *Constitutional Supercooling* hypothesis is proposed by Winegard and Chalmers [50]. During columnar growth, a region of constitutionally undercooled (or 'supercooled') liquid forms ahead of the dendrite tips, i.e., the region enclosed by the dashed line and the temperature profile line in Fig. 2.3(a), due to an accumulation of solute in the liquid. It is assumed that, once a critical level of undercooling is exceeded, heterogeneous nucleation of equiaxed crystals can occur on unknown particles in the undercooled melt. If the equiaxed grains are sufficient in size or number the progress of the columnar growth will be stopped.

The *Big Bang* hypothesis of Chalmers [51] proposes that very large numbers of equiaxed crystals can nucleate in the supercooled region at or near the mould walls of a casting during pouring, in a manner similar to chill grain formation. However, the equiaxed grains are transported throughout the melt as a result of convection due to pouring. Equiaxed grains that survive remelting can then continue to grow when they encounter constitutionally undercooled regions in the melt.

The *Dendrite Arm Remelting* theory is proposed by Jackson et al. [52] in a study observing solidification experiments of transparent alloy analogues. They noticed necking (thinning) of secondary dendrite arms due to solute build up. Latent heat release, convection, or fluctuations in growth rate could lead to fragmentation of these secondary arms which subsequently get transported by buoyancy forces into the melt where they grow as equiaxed grains.

The *Showering of Dendrite Particles* theory is proposed by Southin [53] in a study that observed the solidified macrostructure of Al–Cu laboratory ingots. This theory suggests that dendritic crystals form at the free surface of an ingot could somehow break away and sink into the melt where upon they meet other grains growing from the mould wall. In this study, the observed equiaxed grains were comet shaped since they tended to grow in line with the columnar grains on impingement.

The *Separation* theory is proposed by Ohno et al. [54]. Optical microscopy was used to observe the beginning of solidification at the mould in the unidirectional solidification of Sn–Bi, Bi–Sn, Sn–Pb and Pb–Sn alloys. It is suggested that equiaxed crystals, formed at the mould walls

in a similar manner to the Big Bang hypothesis, have narrow necks that can be broken by thermal convection forces before they fully solidify. The broken equiaxed dendrite would separate and be transported into the melt where they may continue to grow as free dendrites in undercooled regions.

Hutt and St John conclude by stating that all of the above mechanisms can occur depending on alloy composition, casting conditions and the types of substrates available for nucleation of equiaxed grains in the melt. However, in the case of directional solidification of an alloy using the Bridgman method—with an imposed positive temperature gradient—and in the absence of convection effects or fluctuations in the cooling conditions, the origin of equiaxed grains is most likely to occur under the constitutional supercooling hypothesis.

CET models

A review of analytical and numerical models for predicting CET is given by Spittle [48]. Spittle helpfully states that one of two possibilities exist for the transition: either, columnar growth slows down allowing equiaxed grains to dominate; or, equiaxed grains take over and force the arrest of columnar grain growth. In any case, models for CET can use either *direct* or *indirect* prediction methods [55]. Direct prediction methods simulate the growth of both columnar and equiaxed grains, whereas indirect prediction methods simulate columnar growth only and analyse the condition at, or ahead of, the columnar growth front (e.g., temperature gradient and undercooled region size) with respect to the likelihood of equiaxed growth occurring. Some examples of indirect and direct CET modelling methods are given below.

McFadden et al. [56] present a comparison of three indirect CET prediction methods using experimental data from a directional solidification study with aluminium–silicon alloys by Gandin [47]. The first method: '*Constrained-to-Unconstrained*' criterion, proposed by Gandin [57], involves a 1-dimensional front tracking model that uses Landau transforms to estimate the growth rate and temperature gradient at dendrite tip. CET is predicted to occur when the cooling rate at the tip reaches a maximum and when the temperature gradient switches from a positive value to slightly negative value. The second method: '*Critical Cooling Rate*' criterion, proposed by Siqueira [58], shows how measured CET positions in aluminium–copper and tin–lead alloys coincided with a certain critical cooling rate. The cooling rate is calculated as the product of the modelled liquidus isotherm velocity and temperature gradient. (It is important to note that no information is known about conditions at the dendrite tip using this method.) The final method: '*Equiaxed Index*' criterion proposed by Browne [59], examines the conditions ahead of the columnar dendrite tip, specifically, in the bulk undercooled liquid. By application of an explicit control volume (CV) front tracking method, the Equiaxed Index, $I_{ex}(t)$, is proposed as an indicator of the likelihood of equiaxed growth, given by the following equation:

$$I_{ex}(t) = \sum_{i=1}^{ncols} \sum_{j=1}^{nrows} U_b(i,j) \Delta x_i \Delta y_j \quad , \tag{2.12}$$

17

where i and j are spatial labels of a 2-dimensional domain ($nrows \times ncols$) of CVs, Δx in width and Δy in height, and U_b is the estimated bulk undercooling value at each control volume. This index has a single value for the entire domain, and is a function of time; the time at which its peak value occurs indicates the most likely time—and hence columnar front position—for CET to occur.

Two direct CET methods are described next. Hunt [60] presents a 1-dimensional analytical model that predicts columnar, equiaxed or mixed microstructure for steady-state directional solidification using the Bridgman method. An analysis is presented that uses an intuitive approach to calculate the extended volume fraction of equiaxed grains using the Avrami equation [61]. The model predicts fully equiaxed growth when,

$$G < 0.617 N_0^{\frac{1}{3}} \left\{ 1 - \frac{(\Delta T_N)^3}{(\Delta T_{tip})^3} \right\} \Delta T_{tip} \quad , \tag{2.13}$$

where G is the temperature gradient, N_0 is the total number of available heterogeneous substrate particles per unit volume, ΔT_N is the nucleation undercooling, and ΔT_{tip} is the dendrite tip undercooling of the columnar dendrites (calculated as a function of growth rate, v_{tip}). This expression is derived from an assumption based on a probabilistic analysis of columnar and equiaxed grain geometry, where 'fully equiaxed' growth corresponds to an extended volume fraction of equiaxed grains equal to 0.66, and 'fully columnar' growth corresponding to volume fraction of equiaxed grains equal to 1% of this value. The results of the analysis are presented in plots of columnar growth rate versus temperature gradient, showing the predicted equiaxed, mixed (equiaxed and columnar), and fully columnar regions for a given alloy composition, nucleation density and nucleation undercooling. Hunt concludes the analysis stating that, at low growth rates equiaxed growth depends on the efficiency of grain refiners, and that, at high temperature gradients the number of nucleation sites is more important. The above described criterion for CET has become known as *mechanical* blocking [62] and is currently the most widely used in the literature.

Alternative blocking criteria for CET have been suggested in the literature. One such alternative is proposed by Martorano et al. [63]. The authors consider the interaction between, the solutal field in the liquid surrounding the equiaxed dendrite envelope (extra dendritic liquid), and the solutal field in the liquid ahead of the growing columnar front. Using this approach, CET is assumed to occur when the *average* composition in the extra dendritic liquid rises to meet the composition of the liquid at the growing columnar dendrite tips, thus removing the solutal undercooling (i.e. the primary driving force for growth). This approach has become known as *solutal* blocking [48].

2.3 Eutectic Solidification (hypoeutectic path)

To continue the discussion it is appropriate to consider the equilibrium of phases for the alloy of interest, in other words, its *equilibrium phase diagram*. In this section, a binary eutectic alloy phase diagram is considered, as shown in Fig. 2.5. This type of alloy system is common,

examples include: lead–tin (Pb–Sn), aluminium–silicon (Al–Si), and copper–silver (Cu–Ag). Eutectic solidification involves the transformation of a liquid into two distinct phases, L→α+β, of fixed composition. Only alloys having a composition corresponding to the invariant point (position 4 in Fig. 2.5), i.e., the eutectic composition, undergo a single phase transformation so that a fully liquid material appears to spontaneously solidify at the eutectic temperature, T_{euc}. An example of one such alloy is plumbers solder (Pb–61.9wt.%Sn) [64]. Where an alloy has an original composition, C_0, less than the eutectic composition, but greater than the primary phase solubility limit (position 5 in Fig. 2.5), it is referred to as a *hypoeutectic* alloy. The solidification path of such an alloy is considered next.
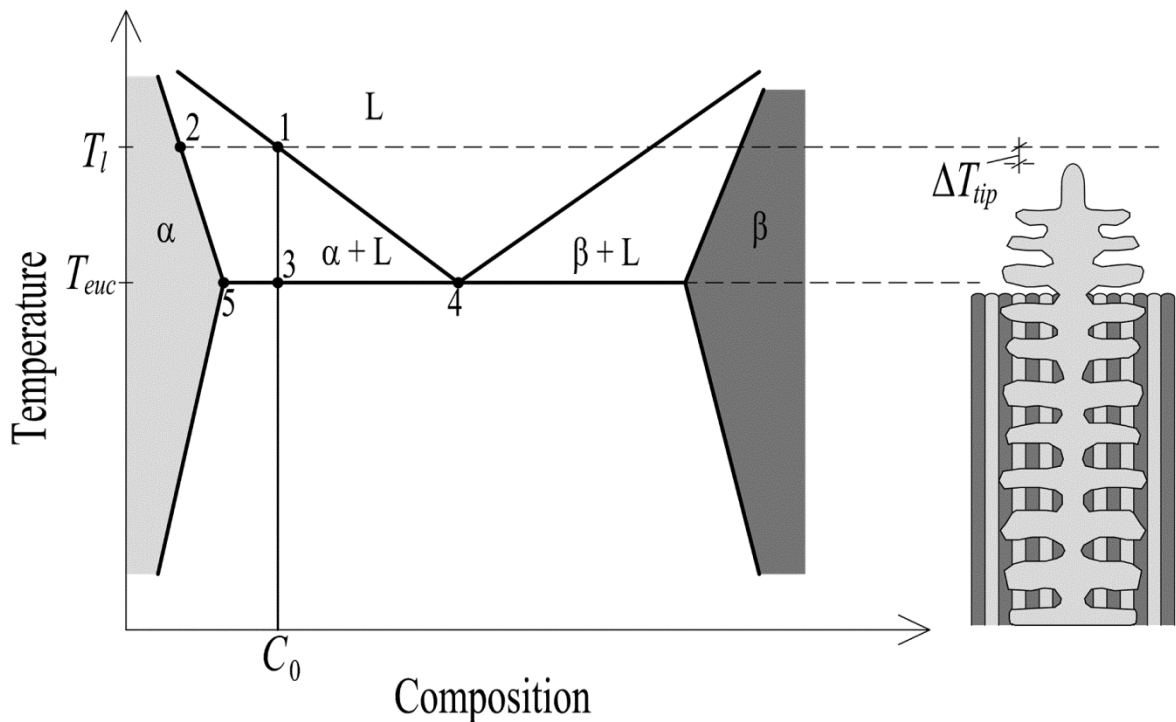
Fig. 2.5 Typical binary eutectic alloy phase diagram and hypoeutectic dendrite morphology, adapted from [4].

The material begins solidification as liquid, having a temperature higher than the alloy equilibrium liquidus temperature, T_l (position 1 in Fig. 2.5). As cooling progresses the first material to solidify is the primary α-phase, having composition given by position 2. As the temperature decreases, the composition of α-phase increases (moving along the α-solidus line), until the eutectic temperature is reached. This is the L+α period of solidification. At this point the solubility of the β-phase in α-phase is saturated (at the solubility limit, position 5) so that any remaining liquid solidifies via the eutectic transformation, L→α+β. A mutual exchange of solute between the α and β phases, via transport in the liquid, allows this to occur [4].

A typical α-phase dendrite for this alloy is shown on the right hand side of Fig. 2.5; its tip growing at a temperature below the equilibrium liquidus temperature, but above the eutectic

temperature, with undercooling, ΔT_{tip}. The eutectic material is visible (ordered structure of parallel α and β phases) following the dendrite tip at some temperature just below the eutectic temperature.

2.4 Peritectic Solidification (hypoperitectic path)

Many important materials exhibit peritectic solidification behaviour. Some examples being; the iron–carbide (Fe–C) system for steels, bronze (Cu–Sn), brass (Cu–Zn), titanium–alumindes (Ti–Al), lanthanide magnets (Nd–Fe–B), and ceramic superconductors (Y–Ba–Cu–O) [9]. Typically, peritectic materials solidify via two distinct processes; the peritectic reaction, and the peritectic transformation. Consider the equilibrium phase diagram for a typical peritectic material, of composition C_0, as shown on the left hand side of Fig. 2.6. The solidification path of this hypoperitectic material is now considered.
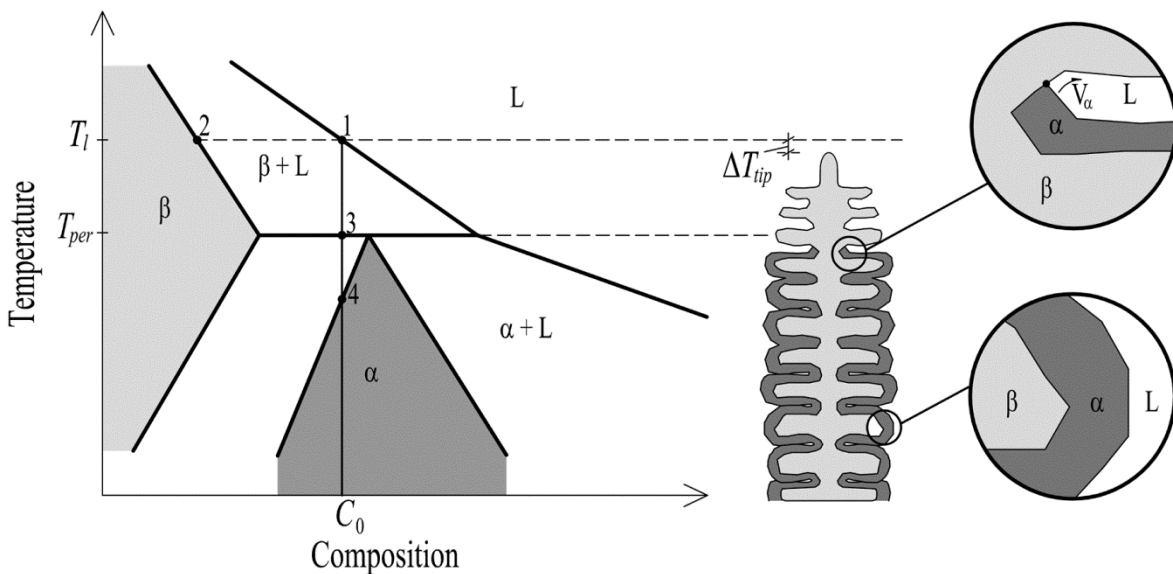
Fig. 2.6 A binary peritectic phase diagram and hypoperitectic dendrite morphology. The inserts illustrate a peritectic reaction (upper) a peritectic transformation (lower), adapted from [4].

2.4.1 The peritectic reaction

The material begins the solidification process as fully liquid at temperatures higher than the material equilibrium liquidus temperature, T_l (position 1 in Fig. 2.6). As the material is cooled below this temperature, the primary β-phase will solidify first, initially with a composition as given by position 2, and gradually increasing in composition as the temperature decreases until the equilibrium peritectic temperature, T_{per}, is reached, given by position 3. This is the L→β+L period of the solidification process [4].

As the material is cooled further, at some temperature just below T_{per}, the peritectic reaction occurs where the secondary α-phase begins to grow at the β+L interface. All three phases; α, β and Liquid, are in contact with each other during the reaction, as illustrated in Fig. 2.6 by the small black circle in the upper insert. This is the β+L→α+β period of the solidification process. The secondary α-phase grows laterally around the existing β-phase at some velocity, V_α.

2.4.2 The peritectic transformation

As further cooling occurs (moving away from position 3 to position 4) the primary β-phase continues to grow; however, the secondary α-phase (left behind by the peritectic reaction) begins to engulf the β-phase by diffusion at the α–β interface. The α-phase also continues to grow at the expense of the Liquid phase through the α–L interface. In this case, the secondary α-phase divides the Liquid and primary β-phase [65]. This process is illustrated in the lower insert of Fig. 2.6 and is known as the peritectic transformation.

It is important to note that the above example assumes that equilibrium solidification does not occur; rather, dendritic growth of the primary β-phase occurs (in a positive temperature gradient) with some level of undercooling; this is followed by non-equilibrium peritectic growth through the peritectic reaction and transformation processes. Further details regarding these processes can be found in a review by Kerr and Kurz [66].

2.4.3 Growth models of peritectic solidification

Fredriksson [67] provides a detailed account of the peritectic reaction and transformation in relation to the iron–carbide and iron–nickel systems. There are some existing growth models that can reasonably predict the kinetics of peritectic growth. However, these models seem to work well for some alloys and not for others, in other words, the models are alloy specific. For example; Bosze and Trivedi [68] outline a model where a platelike (or Widmanstätten) morphology can be used to predict the growth of peritectics. Fredriksson and Nylén [69] found that this model compares very well with experimental data for Cu–Sn alloys, but very poorly with Ag–Sn alloys.

Another study by Phelan [70] et al. employing the same growth model shows—using in-situ observations of the peritectic reaction—how Fe–C alloys grew much faster than predicted. This discrepancy is explained by the fact that stress and strain, between the primary and secondary phases, increases during solidification because of density differences between the phases. The free energy in each phase changes as a result, leading to changes in position of the solubility lines on the equilibrium phase diagram, this in turn leads to diffusionless transformation [67].

A recent study on the solidification of binary Al–Ni powders, by Tourret and Gandin [71], gives a 1-dimensional spherical growth model to predict peritectic growth (along with dendritic and eutectic). The model incorporates the growth model developed by the KGT model [30] for columnar dendritic growth.

2.5   Gamma Titanium Aluminide Alloys

At the turn of the millennium, gamma titanium aluminide (γ–TiAl, gamma TiAl) peritectic alloys had emerged as a viable structural material—particularly in aerospace and automotive applications [72]—on account of their excellent mechanical properties. While gamma TiAl alloys offer similar strength and stiffness properties to that of established structural materials, e.g., nickel

based superalloys, steel or other titanium alloys, they have a low density advantage over competitors. Dimiduk [73] outlined this using cross plots of material properties [74] for gamma TiAl to compare density normalised mechanical properties; specific strength (yield strength/density), and specific modulus (elastic modulus/density, i.e., stiffness-to-weight ratio), over a range of temperatures. For example, the specific modulus of gamma TiAl alloys can be 50-70% greater than that of nickel-based superalloys, or other titanium alloys, at elevated temperatures. Also, the specific strength versus temperature for gamma TiAl alloys, relative to other alloys, is significantly larger, as shown in Fig. 2.7.
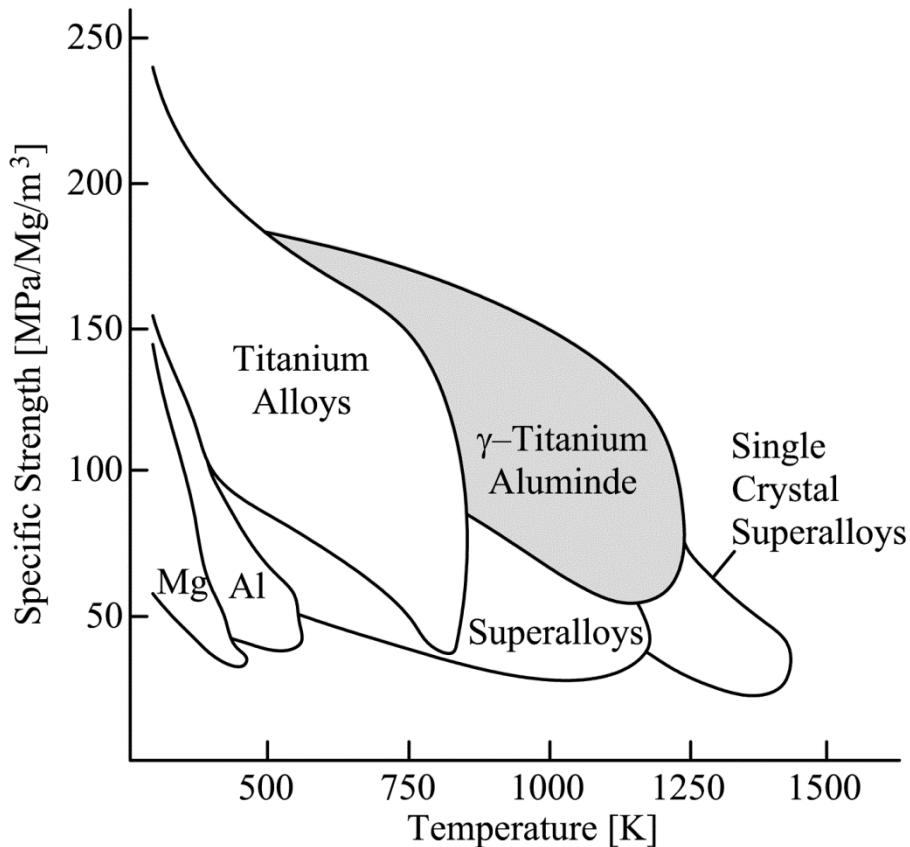
Fig. 2.7 Specific strength versus temperature for various alloys [73].

These studies [72][73] predicted that approximately 10-15 years of technology maturation would be required for successful implementation of TiAl in real applications, citing cost of production versus improvement in performance as key to its success. Casting issues surrounded the alloy given its high liquidus temperature (~1500 °C), the high reactivity of molten titanium, and other common casting problems such as shrinkage porosity, hot tearing and misrun [75]. Currently, however, a 2nd generation gamma TiAl multicomponent alloy (Ti–48Al–2Cr–2Nb, all at. %) is in service [76] as low pressure turbine (LPT) blades in the GEnx (General Electric's next generation) aero engine [77], see Fig. 2.8. This engine is currently used to power Boeing's 787 Dreamliner aircraft.
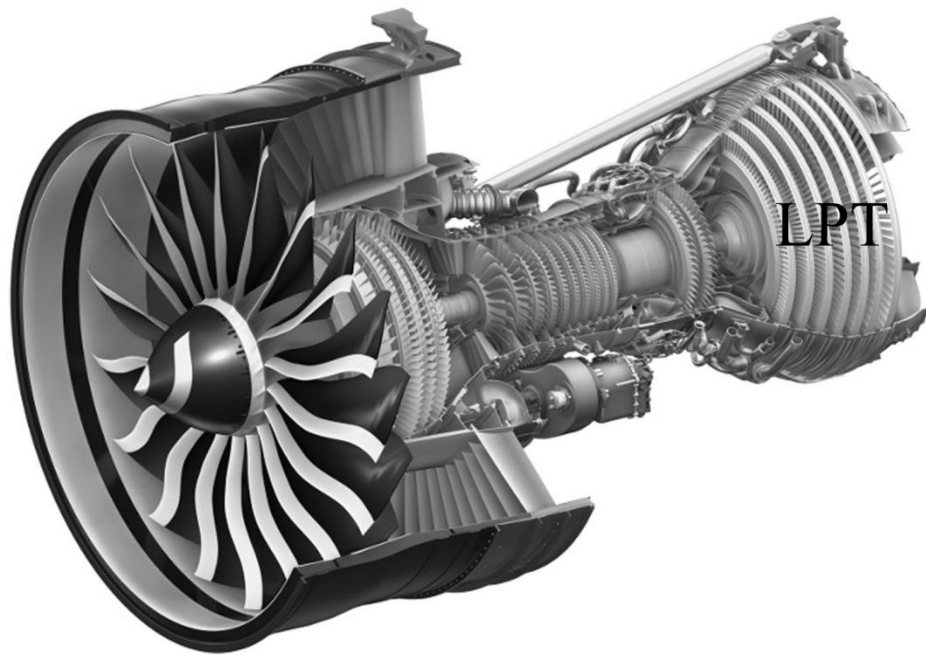
Fig. 2.8 GEnx aircraft engine [77].

While the introduction of this relatively new material into service marks an important milestone for the success of gamma TiAl alloys, rising fuel costs have led to higher engine efficiency targets and hence higher engine operating temperature requirements. So called 3rd generation gamma TiAl alloys, having a higher quantity of niobium or molybdenum, can increase the maximum application temperatures—limited by creep resistance—from 700 °C (for 2nd generation TiAl alloys) to 850 °C [78]. One such 3rd generation alloy, with chemical composition Ti–45.5Al–4.7Nb–0.2B–0.2C (all at. %), has been the focus of an experimental study [79] examining CET in directionally solidified castings.

2.5.1 The TiAl binary alloy phase diagram

Murray [80] gives a thorough assessment of the TiAl system which has been subsequently updated by Okamoto, twice [81] [82]. Schuster and Palm [83] give a critical assessment of all available phase diagrams (from the literature) for the binary TiAl system. However, a recent experimental study by Witusiewicz et al. [84] observes that none of the available data in the literature could successfully represent the current experimental data for the TiAl system. They carry out a re-evaluation of the system using the CALPHAD (CALculation of PHAse Diagrams) approach to obtain the phase diagram shown in Fig. 2.9. The region of this phase diagram of interest—as part of this thesis—is encircled in grey in the figure.

Clemens [78] notes that, for fine grained TiAl binary alloys, room temperature elongation to fracture varies directly with aluminium content, reaching a maximum at Ti–48Al (at. %). Since low temperature ductility is a limiting factor in structural applications, most engineering gamma TiAl binary alloys are restricted to the 45–48Al (at. %) range. However, early in the development of

gamma TiAl alloys, it was recognised that the use of binary TiAl alloys for structural applications would not be possible due to poor resistance to creep at high temperatures and oxidisation. To combat these issues various studies investigating the introduction of other alloying elements were initiated, two such studies are discussed in the following section.
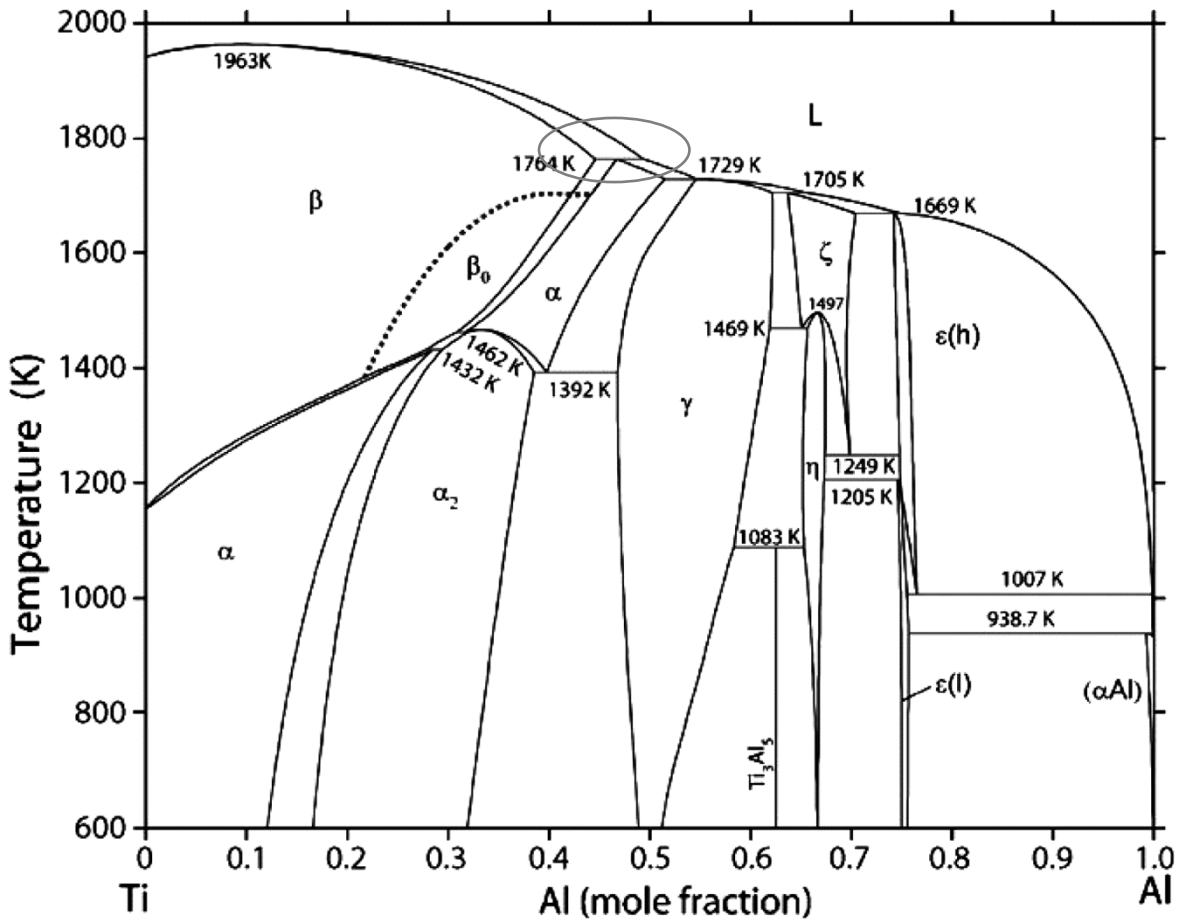
Fig. 2.9 Titanium-aluminium phase diagram [84].

2.5.2 Current studies involving multicomponent gamma TiAl alloys

A recent investigation by the European Space Agency (ESA) backed research group IMPRESS (Intermetallic Materials PRocessing in relation to Earth and Space Solidification) [85] looked in detail at the effect of casting gamma TiAl alloys in microgravity environments, as part of the MAXUS 8 sounding rocket mission [86]. Niobium—as an alloying element—was considered in this study, with and without boron grain refinement. The alloy compositions of interest to this group were the following intermetallic compounds: the ternary unrefined alloy, Ti–46Al–8Nb (all at. %); and the multicomponent refined alloy, Ti–46Al–7.5Nb–2.5B (all at. %). A CET was not achieved in any of the alloys in the microgravity experiments. This, ultimately, was due to a furnace design problem leading to unwanted radial columnar growth in the unrefined samples that consequently disallowed the possibility of CET occurring [87].

24

A similar alloy to that studied in IMPRESS—but with a lower level of boron, and low levels of carbon—is now the current focus of the ESA backed research group; GRADECET. The material of interest in this study is a gamma titanium aluminide multicomponent alloy with a nominal composition of: Ti–45.5Al–4.7Nb–0.2C–0.2B (at. %), hereafter referred to as alloy 455. (This alloy composition is also a focus of this thesis.)

GRADECET (GRAvity DEpendence of Columnar to Equiaxed Transition in Ti–Al Alloys) aims to understand the effect that gravity has on the casting process of this alloy. Experiments, using a redesigned version of the IMPRESS furnace, are planned for microgravity environments (less than 10^{-4} g) on-board the MAXUS sounding rocket, in terrestrial environments (1 g) in a standard laboratory setting, and in hypergravity environments (up to 20 g) in the large diameter centrifuge at the ESA in Noordwijk, the Netherlands. The complicating effects of gravity, e.g., thermal and solutal convection and sedimentation, are suppressed in microgravity solidification experiments. By carrying out identical experiments in terrestrial environments, it is possible to distinguish the effect of these phenomena from others—common to both environments—and therefore refine and improve theoretical models for casting [88]. Hypergravity is important when considering the centrifugal casting technique, commonly used to manufacture, for example, high performance turbine blades for aero-engines.

The main focus of GRADECET is to understand the relationship between the solidification conditions occurring (e.g., temperature gradient and growth rate), and the resulting cast microstructure. The conditions to produce a CET in the microstructure are of particular interest.

2.5.3 Effect of further alloying elements (Nb, B, C)

The addition of niobium to the binary gamma TiAl alloy is known to be beneficial in several ways. First, gamma TiAl alloys are strengthened by its addition, since the α-tranus line on the phase diagram is shifted towards the Al rich side, narrowing the α+γ field, and hence stabilising the β(Ti) phase leading to microstructural refinement [89]. The resulting dense microstructure reduces dislocation glide and so increases yield strength, via the Hall-Petch boundary strengthening mechanism. Second, it is understood that stacking fault energies are reduced by high levels of niobium in gamma TiAl alloys, so that mechanical twinning becomes the prominent deformation mode giving an improved ductility [90]. Third, niobium increases the activation energy of diffusion which has the effect of improving creep resistance at high temperatures. Finally, oxidisation resistance is significantly improved [91].

Small quantities of boron are commonly added to titanium alloys as a mechanism for grain refinement though the formation of titanium diboride (TiB_2) acting as heterogeneous nucleation sites, a phenomenon first documented by Bryant [92].

It is also possible for carbon to be added to gamma TiAl alloys, as an interstitial alloying element, to increase creep strength via precipitation hardening arising through the formation of perovskite type carbides (Ti_3AlC) [93].

2.5.4 Applications of gamma titanium alloys

Established titanium alloys have traditionally been used in applications where weight and/or space saving is important without compromising strength. For example, the landing gear beams on-board the Boeing 747 and 757 aircraft are titanium forgings [94]. The load requirements and space restriction for this application deem titanium alloys appropriate. The marine and chemical industries make use of commercially pure titanium alloys due to their unusually high corrosion resistance [64]. Peritectic gamma titanium aluminide alloys, however, are used in applications that demand a combination of several properties, e.g., low density, high strength, good ductility, good resistance to creep at high temperatures, good resistance to oxidisation, and burn resistance. There are a number of applications that demand such properties where gamma TiAl alloys have been used so far. The most current applications are now discussed.

Aerospace applications

The main application of interest has been already mentioned, i.e., low pressure turbine blades for aero engines. Some practical advantages associated with these alloys over rival materials are as follows. The weight saving in the blade itself is of the order of 50%. A knock on effect exists relating to other components in the turbine assembly, for example, the rotating disc that holds the blades in place can be made leaner, given that the centrifugal force requirements exerted by the spinning blades is lower [89]. The overall weight reduction results in a higher engine rotation speed and hence improved engine performance and efficiency. For gamma TiAl alloys, a higher stiffness to weight ratio gives a higher natural frequency of vibration when compared to traditional nickel superalloys. This results in a quieter less noisy engine [78]. General Electric have 20,000 gamma TiAl LPT blades in service on nineteen Boeing 787 and 747-8s [76]. Rolls Royce have been developing gamma TiAl alloys since 1999 [95], and have recently stated on their website that gamma TiAl alloys will be used in the LPT of their next generation Trent XWB aero engine [96].

Apart from LPT blades, other engine components have been targeted for gamma TiAl such as: stator vanes, exhaust components, combustor casings, radial diffusers, transition duct beams and turbine blade dampers. Finally, gamma TiAl was cited as a potential material to be used in the development of a future supersonic high speed civil transport aircraft [97].

Automotive applications

Internationally, the motor industry is facing increasingly stringent legislation in terms of carbon dioxide emissions and fuel consumption. As a result, engine sizes are getting smaller, engine rotational speeds are increasing, and target exhaust gas temperatures are increasing. Gamma TiAl components can help to reach these efficiency and performance targets. For example, Mitsubishi Motor Corp have used a gamma TiAl alloy in the turbocharger rotors for the Lancer Evolution cars series [98]. While not in service yet, it has been reported recently [99] that, gamma TiAl will be used in the valve train of 4-stroke internal combustion engines. Interestingly, gamma TiAl engine

valves were introduced successfully in Formula-1 racing car engine valves [100] until the FIA subsequently banned their use from 2006 onwards.

Processing Routes

Several processing technologies are capable of producing parts from TiAl alloys, among them; investment casting [101], electron beam melting or EBM [102], and forging with advanced machining [103], the latter using pre-shaped cast feedstock.

2.6 The Front Tracking Model (FTM)

The casting process has traditionally been completed using experience-based techniques developed by foundry engineers [104]. Key discoveries, like that of Chalmers and co-workers [41] [50] relating constitutional undercooling, solid–liquid interface growth rate, and temperature gradient, have provoked a steady development of mathematical models for the solidification phenomena observed by casting engineers. Knowing the position, velocity and temperature gradient of the solid–liquid interface during alloy solidification is central to understanding of the final cast grain structure. Various models capable of predicting this structure—and specifically CET—have been developed at different length scales. Wu and Ludwig [105], Martorano and Biscuola [106] and Jacot et al. [107] have developed models to predict CET at the macroscopic length scale (at the scale of the casting). Models to predict CET at the mesoscale (at the scale of the grain) have been developed using the Monte Carlo method [108] and cellular automation technique [109]. Microscale models (at the scale of dendritic features) to predict CET have been developed using the phase field method [110] and the cellular automation technique [111].

A front tracking model (FTM) refers to a numerical model that estimates and follows the growth of a solidification interface, or grain envelope, during solidification, i.e., at the macroscale or mesoscale of the casting (in the order of millimetres). FTMs have been used to track the solidification interface in simple phase change problems involving pure materials [39], and also in more complex problems involving binary alloys [112]. In this section, the key features of the front tracking model (FTM) algorithm by McFadden and Browne [113], capable of predicting CET, are outlined. This model is an extension of a previous front tracking model by Browne and Hunt [114].

2.6.1 The heat equation

The model uses an explicit finite difference control volume (CV) numerical method to solve the following heat equation over a 2-dimensional domain;

$$\rho c \frac{\partial T}{\partial t} = \frac{\partial}{\partial x}\left(k \frac{\partial T}{\partial x} \right) + \frac{\partial}{\partial y}\left(k \frac{\partial T}{\partial y} \right) + E \quad . \tag{2.14}$$

The first term on the left hand side (LHS) describes the time rate of change of thermal energy in the CV, where t is time, ρ is the material density, c is the material specific heat capacity, and T is

temperature. The first and second terms on the right hand side (RHS) give the net change in heat flux by thermal diffusion in the *x* and *y* directions, respectively, where *k* is the material thermal conductivity. The final term, *E*, is a source term used to deal with the latent heat released during solidification with units of W/m^3. The model ignores the effect of convection in the melt.

2.6.2 Nucleation

To initiate crystal growth nucleation must occur. Hence, as the melt is cooled, at some temperature the free energy of the liquid phase reduces such that it equals the free energy of the solid phase, and a transformation from liquid to solid occurs [115]. The front tracking model assumes that this transformation occurs at some fixed temperature, T_{nuc}, below the equilibrium liquidus temperature of the alloy, T_l. The difference between these temperatures is known as the nucleation undercooling, $\Delta T_{nuc} = T_l - T_{nuc}$.

This assumption is reasonable given that nucleation rate undergoes a steep increase below a certain temperature [116]. In the McFadden and Browne FTM, the values for nucleation undercooling are set independently for columnar and equiaxed crystal growth. The columnar growth nucleation undercooling is estimated using the 'cap' model of nucleation [117]. While the nucleation undercooling for equiaxed growth is determined by a relation involving the seed particle diameter, solid-liquid interfacial energy, and volumetric entropy of fusion [118]. For both types of growth, the user manually sets the seed locations (nucleation sites) on the domain grid from which columnar or equiaxed growth could initiate once the seed is activated, i.e., when some specific value for ΔT_{nuc} is reached.

2.6.3 Tracking the front

The McFadden and Browne FTM is developed for binary hypoeutectic alloys. A schematic for dendritic and eutectic growth of a hypoeutectic material in the southwest quadrant of a square mould is shown in Fig. 2.10(a). Columnar dendrites (in black) are growing from the mould wall into the liquid melt (white area), equiaxed dendrites (in grey) are forming in the melt, and eutectic solid (cross hatched) is following behind the progressing columnar dendrites.

Figure 2.10(b) depicts how the FTM treats this scenario. The columnar front is given by a line joining the large columnar dendrite tips. The area between this line and the fully solid area is called the columnar mush, made up by solid columnar dendrites and interdendritic liquid. In a similar manner, the equiaxed dendrite tips are joined to form a front. However, in this case there is one front per equiaxed dendrite, which encompasses it, giving an equiaxed envelope. Each envelope contains solid equiaxed dendrites and interdendritic liquid and each envelope represents a single grain.
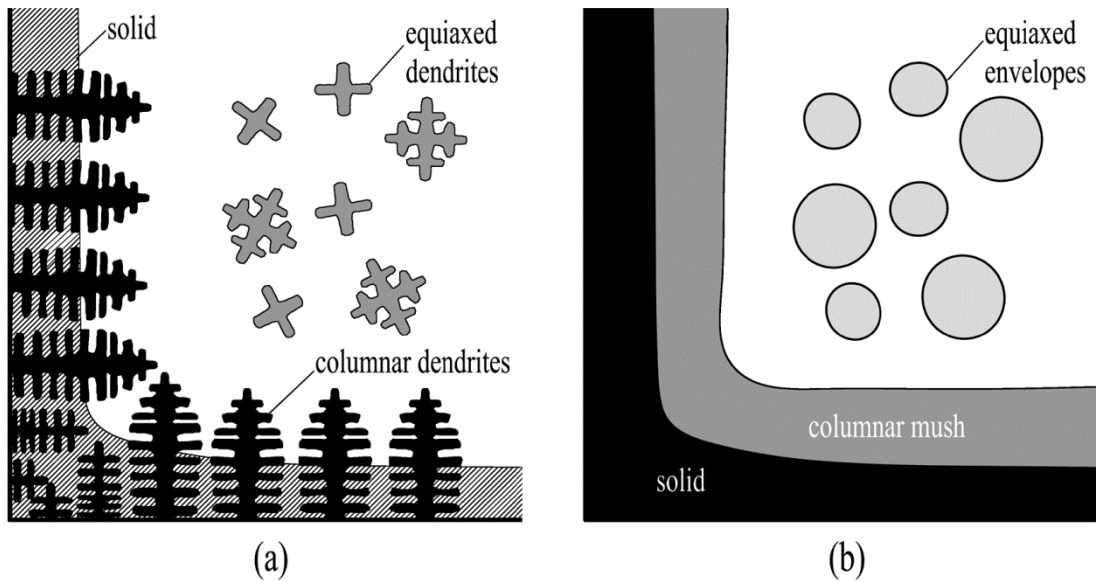
Fig. 2.10 (a) Schematic of dendritic growth. (b) Front tracking model applied to dendritic growth.

The columnar front can be made up by a number of columnar grains that have grown independently, impinged upon one another, and merged to form a new front. A more detailed illustration of typical evolution of columnar growth in the FTM is shown in Fig. 2.11 [87]. The solidification front is given by computational markers at the intersections with the square CV gridlines. Piecewise linear segments between the markers define the columnar front.
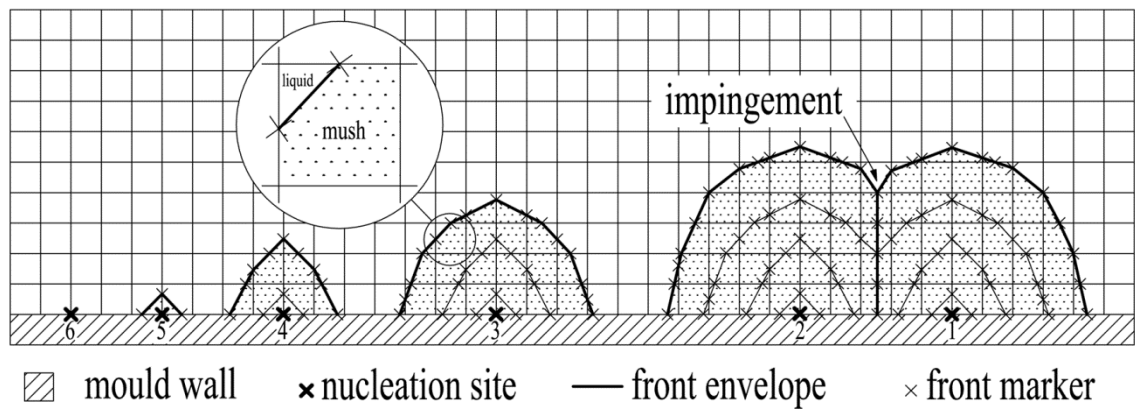
Fig. 2.11 Evolution of nucleation sites showing early columnar growth and impingement [87].

Once a nucleation site is activated it is permitted to grow as a grain. At every time step thereafter, the undercooling and hence dendrite tip velocity at every marker (making up that grain) is calculated using *dendrite kinetics*. The front marker locations are then updated to form a new front envelope and the process is repeated. The dot hatched areas in Fig. 2.11 are mushy regions and the non-hatched areas are liquid regions.

It is clear that nucleation sites 1 and 2 have nucleated at the same time, followed by sites 3, 4, and 5 at subsequent times. Site 6 has not yet nucleated. The grains formed by sites 1 and 2 have impinged. The insert shows an enlarged view of a CV containing the liquid–mush front, i.e., the columnar front. This shows how the front markers separate the liquid and mushy zones to give a

29

captured volume of mush in that CV, used to calculate the *latent heat* released as solidification progresses.

2.6.4 Dendrite kinetics

The solution of equation (2.14) gives the temperature at all CVs. The temperature at any front marker, i.e., the temperature at the modelled dendrite tip, T_{tip}, is then calculated using bilinear interpolation of the surrounding CV temperatures. This temperature is used to calculate undercooling at the marker, ΔT_{tip}, as follows:

$$\Delta T_{tip} = T_l - T_{tip} \quad , \tag{2.15}$$

where T_l is the equilibrium liquidus temperature. The undercooling at this position is then used to calculate the subsequent growth rate, v_{tip}, i.e., the magnitude of dendrite tip velocity, according to a dendrite growth law (power law) for low thermal gradients by Burden and Hunt [119], as follows:

$$v_{tip} = C \Delta T_{tip}^{b} \quad , \tag{2.16}$$

where C is the dendrite growth coefficient having units of m/s·°C^b, and b is the dimensionless undercooling exponent. The direction of growth of a front marker is given by the bisector of the angle made by the line segments that meet at the marker.

2.6.5 Latent heat

To solve equation (2.14) the value for the source term, E, must be known. This term is the rate of latent heat released during solidification per unit volume. An equation for E can be assembled by considering; latent heat released by a per unit volume (ρL_M) times the volume of material solidified per second ($\partial V_S/\partial t$), thus giving units of Watts; then dividing by the volume of one CV (V_{CV}) gives the heat rate per unit volume in one CV, having units of W/m^3. The equation is as follows:

$$E = \frac{\rho L_M}{V_{CV}} \left(\frac{\partial V_S}{\partial t} \right) \quad , \tag{2.17}$$

where L_M is the latent heat of fusion per unit mass and V_S is the volume of material solidified. The volume of material solidified is calculated using the *internal solid fraction* approach after Banaszek and Browne [120], which is illustrated in Fig. 2.12. A typical CV (with the front passing through) is shown in the figure. The captured volume of mush, d, is given by the region made up of solid columnar dendrites (dark grey) of volume, V_S, and interdendritic liquid (dot hatched), all within the CV of volume, V_{CV}. The internal fraction of solid (volumetric), g_S, is given the ratio of solid volume to captured volume within the mush region,

$$g_S = \frac{V_S}{d} \quad . \tag{2.18}$$

Rearranging for V_S and differentiating with respect to time gives: $\partial V_S/\partial t = g_S(\partial d/\partial t) + d(\partial g_S/\partial t)$. This relation allows the latent heat term to be dealt with in two parts: *viz.* $E = E_a + E_t$ where,

$$E_a = \frac{\rho L_M}{V_{CV}} g_S \left(\frac{\partial d}{\partial t} \right) \quad , \tag{2.19}$$

$$E_t = \frac{\rho L_M}{V_{CV}} d \left(\frac{\partial g_S}{\partial t} \right) \quad . \tag{2.20}$$

The term E_a accounts for latent heat released due to the <u>a</u>dvancement of the front, while E_t accounts for latent heat released due to the <u>t</u>hickening of the mush in the CV. These latent heat terms are calculated on a per CV basis.
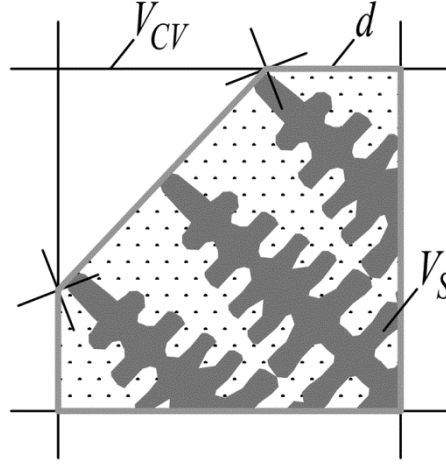
Fig. 2.12 Captured volume.

For a given alloy composition, the volumetric fraction of solid, g_S, can be expressed in another way; as a function of the local CV temperature, T. The Browne and Hunt [114] FTM uses a linear function to estimate fraction of solid such that; it equates zero at the equilibrium liquidus temperature T_l, and unity at the equilibrium solidus temperature T_s, as follows:

$$g_S = \frac{T_l - T}{T_l - T_s} \quad , \tag{2.21}$$

This approach is too simplistic. In real solidification problems a non-linear function like the one presented by Scheil [33] is more appropriate;

$$g_S = 1 - \left(\frac{T_m - T}{T_m - T_l} \right)^{\frac{1}{k_{part} - 1}} \quad , \tag{2.22}$$

where T_m is the alloy melting temperature and k_{part} is the partition coefficient for the alloy. The partition coefficient is taken from the alloy phase diagram as the ratio of composition of solid, C_S,

to composition of liquid, C_L, at any given temperature in the solidification range; T_s to T_l. It is assumed that the liquidus and solidus lines from the alloy equilibrium phase diagram are straight.

With equation (2.22) inserted in the latent heat term E_t, an iteration scheme is required to solve equation (2.14). The McFadden and Browne FTM uses a Newton–Raphson scheme to do so as follows. An error function, $y(g_S)$, is set up by subtracting g_S from the right hand side of equation (2.22) to give,

$$y(g_S) = 1 - g_S - \left(\frac{T_m - T}{T_m - T_l} \right)^{\frac{1}{k_{part}-1}} .$$
(2.23)

The local CV temperature, T, in the above equation, is estimated by the explicit numerical solution to equation (2.14) as follows:

$$T = T^m + \frac{\Delta t}{\rho c V_{CV}} \left(f_c + f_a + f_t \right) ,$$
(2.24)

where T^m is the local CV temperature from the previous time step, f_c is the net flow of heat by conduction into a CV, f_a is the latent heat released due to the advancement of the front, f_t is the latent heat released due to the thickening of mush, and Δt is the time step duration. Note that $f_a = E_a V_{CV}$ and $f_t = E_t V_{CV}$, where $V_{CV} = \Delta x \cdot \Delta y \cdot 1$, in words, Δx is the CV width, Δy is the CV height, and the CV has unity depth.

To initiate the iteration scheme, the value of g_S from the previous time step is used as the first estimate of solid fraction. The final value for g_S is determined (within a specified tolerance) by performing iterations of the following (Newton–Raphson) equation,

$$g_S^{p+1} = g_S^p - \frac{y(g_S^p)}{y'(g_S^p)} ,$$
(2.25)

where superscript p is the iteration index and $y'(g_S^p)$ is the first derivative of equation (2.23) with respect to g_S.

2.6.6 Eutectic solidification in the FTM

Where the alloy being modelled is of eutectic composition, it is assumed that eutectic solidification occurs in equilibrium. That is, a solid front follows behind the tracked front at the equilibrium eutectic temperature for the alloy, i.e., as indicated by the line labelled 'solid' in Fig. 2.10(a). The growth of eutectic solid is calculated using an enthalpy method for isothermal freezing, as given by Voller [121]. The fraction of solid at which eutectic solidification begins is as follows:

$$g_{S\,euc} = 1 - \left(\frac{T_m - T_{euc}}{T_m - T_l} \right)^{\frac{1}{k_{part}-1}} ,$$
(2.26)

where T_{euc} is the equilibrium eutectic temperature, and the total enthalpy, H, per CV is given by,

$$H = cT^m + (1 - g_S^m)L_M + \frac{\Delta t}{\rho V_{CV}} f_c \quad , \tag{2.27}$$

where T^m and g_S^m are the local CV temperature and solid fraction from the previous time step, respectively. The first two terms on the RHS of equation (2.27) represent the enthalpy in a CV at the previous time step, and the last term on the RHS is the change in enthalpy due to thermal diffusion for the current time step. The following conditions determine the local CV temperatures;

$$T = \begin{cases} \dfrac{H}{c} & \forall & H < cT_{euc} \\ T_{euc} & \forall & cT_{euc} \leq H < \left[cT_{euc} + (1 - g_{S_{euc}})L_M\right] \\ T_{Scheil} & \forall & H \geq \left[cT_{euc} + (1 - g_{S\,euc})L_M\right] \end{cases} \quad , \tag{2.28}$$

and the local CV solid fractions are given by;

$$g_S = \begin{cases} 1 & \forall & T < T_{euc} \\ 1 - \dfrac{H - cT_{euc}}{L_M} & \forall & T = T_{euc} \\ g_{S\,Scheil} & \forall & T_L > T > T_{euc} \end{cases} \quad , \tag{2.29}$$

where the subscript '*Scheil*' refers to the solution to equation (2.25).

2.6.7 Thermophysical properties

The FTM uses polynomial functions of temperature to estimate specific heat capacity c, density ρ, and thermal conductivity k, for a given alloy at any temperature T, as follows:

$$property(T) = a_3 T^3 + a_2 T^2 + a_1 T + a_0 \quad , \tag{2.30}$$

where the polynomial coefficients a_0, a_1, a_2 and a_3 are specific to the alloy being modelled, and to each individual property. When a CV contains a mixture of liquid and mush, or liquid and solid, each property is approximated, per CV, by the law of mixing, for example, the thermal conductivity of a CV, k_{CV}, is calculated as follows:

$$k_{CV} = \left[1 - \left(g_s \frac{d}{V_{CV}}\right)\right]k_L + \left[g_s \frac{d}{V_{CV}}\right]k_S \quad . \tag{2.31}$$

2.7   Front Tracking Methods with Convection

A number of authors have carried out modelling work using front tracking methods where convection in the liquid is accounted for. A short review of this work is provided next.

A study by Li et al. [39] present a detailed description of a fixed grid explicit finite difference method, with 2nd order discretisation, for tracking the position and shape of a planar

solidification interface in Cartesian and cylindrical coordinates. Li et al. extend the model [40] to account for natural convection induced in the liquid. The model is applied to a horizontal Bridgman furnace solidification scenario and compared with experimental data for pure succinonitrile [13]. Moving boundary conditions are used to simulate the movement of the sample through the furnace. Distortion of the interface shape, due to thermally induced natural convection in the liquid, is discussed. Good agreement between numerical and experimental results is found.

Banaszek and Browne [120] extend the FTM of Browne and Hunt [114] (for binary alloys) so that it accounts for natural convection induced by thermal gradients in the liquid, *viz.* ahead of the columnar front and within the mushy zone. A control volume method is applied to one quadrant of a square mould containing liquid Al–Cu with a fixed heat transfer coefficient applied at the mould walls. Conservation equations of energy, mass and momentum are solved to determine the thermal and velocity fields where Boussinesq natural convection of a Newtonian and incompressible fluid (the liquid) is assumed. Convection in the mushy zone is treated. The dendrite kinetics law by Burden and Hunt [119] is used to track the columnar front and a simple linear solid fraction to temperature relationship is assumed. While equiaxed growth is not simulated, the authors discuss the potential for equiaxed growth with and without the natural convection accounted for. The study concludes stating that natural convection tends to promote conditions for equiaxed growth in two ways: by lowering the temperature gradient at the columnar front, thereby widening the extent of undercooled liquid; and by providing nucleation sites, potentially via dendrite arm fragmentation.

Banaszek et al. [122] later validated a more advanced FTM with experimental data, for directionally solidified Al–7wt.%Si, by power down method. The model employs the same treatment of convection as in reference [120], a Scheil [33] solid fraction to temperature relationship, and KGT dendrite kinetics. They demonstrate the effect of convection (compared to conduction only) using a metric for evaluating the likelihood of equiaxed growth: *equiaxed index*, as proposed by Browne [59]. It is concluded that the equiaxed index is lowest (and therefore equiaxed growth is least likely) in the early and late stages of solidification, and, that convection increases equiaxed index and hastens its peak value when compared to the conduction only case. (Very recently, Banaszek and co-workers [123] have extended the FTM to simulate dendritic growth in a 3-dimensional domain where convection in the melt is accounted for.)

Mirihanage et al. [124] further developed the McFadden and Browne FTM to include the growth and transportation (due to natural convective effects) of equiaxed grains ahead of a growing columnar front. Simulations of square mould castings of Al–7wt.%Si over a 2-dimensional domain are presented. The mushy zones in both columnar and equiaxed regions are treated as porous media for convective flow. The study is limited to cases where the solutal diffusion length is reasonably smaller than the equiaxed grain size and where solutal convection is weak.

Ludwig and Wu [125] present a qualitative study where a front tracking method is employed to simulate the CET in steel castings (Fe–0.34wt.%C), melt convection and equiaxed grain

transport are included. Mechanical and soft blocking mechanisms for arresting columnar growth is considered, *viz.* due to the presence and sufficient number of equiaxed grains, or due to the disappearance of constitutional undercooling, respectively. The dendritic growth model of Lipton et al. [46] (known as the LGT model) is used to track the solidification front. A control volume method is used to solve conservation equations of mass, momentum, species and enthalpy in three separate phases (liquid, columnar and equiaxed) over a 2-dimensional axisymmetric domain. The main limitation of this model is that ideal solidification morphologies are assumed; cylindrical for columnar growth and spherical for equiaxed. Wu and Ludwig [105] have subsequently developed this model for 3-dimensional domains.

2.8 Conclusion to the Literature Review

It is clear that (from Chapter 1) that the Bridgman furnace solidification process has long been established, and is widely used in industry and research for the purposes of directional solidification. The main advantage of the process is that solidification conditions can be controlled in a precise manner through adjustment of temperature gradient and pulling rate. It is mainly for this reason that the Bridgman method is popular in solidification research.

The literature review (given in this chapter) describes typical solidification morphologies that occur in directional solidification of alloys. This is followed by a description of the columnar and equiaxed types of dendritic growth, and the phenomenon of columnar-to-equiaxed transition in castings. Eutectic and peritectic solidification are explained; particular focus is given to a 3rd generation gamma titanium aluminide alloys (peritectic) that have potential applications in the aerospace and automotive industries. Front tracking methods of modelling solidification are defined and an established front tracking model for alloy solidification from the literature (for eutectic solidification) is described in detail. This is followed briefly by the role of convection in the liquid as applied in front tracking models.

Following the review, it is noted that the FTM originally proposed Browne and Hunt [114], and later extended by McFadden and Browne [113], has not been adapted for traditional Bridgman furnace solidification, i.e., where the sample is pulled through the furnace. Thus far, any implementation of this model has been carried out on a fixed numerical grid, without any movement of the sample through that grid. The McFadden and Browne FTM has been applied to binary alloy solidification problems and, in most instances, to hypoeutectic solidification. Also, this model has not been applied to multicomponent alloys (or to pure materials), nor has it been applied to hypoperitectic alloy solidification with a realistic model for latent heat release.

The gamma titanium aluminium system is currently in its infancy in terms of alloy development for the aerospace and automotive industries. Whilst these alloys offer a low density advantage over their competitors, casting issues and the control of as-cast microstructure remain as barriers to their success. Accurate modelling of the solidification phenomena occurring during growth in these alloys is therefore needed.

2.9   Scope of the Current Research

The scope of the current work relates to the adaption of the front tracking model of McFadden and Browne [113] to model the process of Bridgman furnace solidification in any of its modes: steady Bridgman, transient Bridgman, steady power down, or transient power down. The model is adapted for multicomponent alloy solidification (in terms of latent heat release), specifically, for a hypoperitectic titanium aluminide alloy. The model is also adapted to simulate steady growth in a pure material for the purposes of a verification exercise. Convection in the melt during solidification is not considered in this work. However, consideration of convection would be a logical next step in the development of the model (at a later stage).

The developed model is applied in series with a discrete proportional integral derivative controller for the purposes of characterising a real Bridgman furnace (in terms of heat transfer coefficients). The model is adapted, at this stage, to simulate a hypoperitectic gamma titanium aluminide multicomponent alloy. The developed model, and characterised furnace data, is then used to simulate directional solidification experiments in the same Bridgman furnace. These experiments combine traditional Bridgman solidification in series with power down solidification; both of which involve transient heat transfer. The results from these experiments are then interpreted accordingly using the model.

Relevant discussion and conclusions are provided in each of the four chapters that follow. Further discussion and overall conclusions are then given in two separate chapters to complete the thesis.

Chapter 3

Model Development

In this chapter, a 1-dimensional front tracking model of transient Bridgman solidification of a cylindrical rod is developed and demonstrated for use with binary hypoeutectic alloys, in simple solidification scenarios, and for simple furnace geometries. Referring to Section 1.2, this chapter addresses the first objective of this thesis. Reference [126] is the main source of content for this chapter.

3.1 The Biot Number

A 1-dimensional heat flow model is considered reasonable for Bridgman solidification of metallic alloys where the rod diameter is small, since the majority of the heat flow in the rod occurs in the axial direction [127]. The Biot number, Bi, is used to help vindicate this assumption. The Biot number is defined as the ratio of thermal resistance within a material, to the thermal resistance at its surface; in this case, the thermal resistance within the material is L_{char}/k, and at its surface is, by definition, the inverse of the heat transfer coefficient ($1/h$), giving the following:

$$ Bi = \frac{hL_{char}}{k} \quad , \tag{3.1} $$

where h is the heat transfer coefficient at the surface of the rod, L_{char} is characteristic length of the rod and k is the thermal conductivity. When the Biot number is less than 0.1, the temperature at the centre of the rod is very nearly equal to the temperature at the surface of the rod for any point along its axis [128] since the rate of heat transfer within the rod is much faster than that occurring at its surface. The characteristic length of the rod is given by the rod volume divided by the effective surface area through which h acts. For a long rod (large length-to-diameter ratio) the characteristic length is equal to half the rod radius. Therefore, a low Biot number is expected for Bridgman solidification of metallic alloys (having high thermal conductivity) where the rod diameter is small.

3.2 Bridgman Furnace Front Tracking Model (BFFTM)

The objective of the model is to simulate columnar growth in Bridgman furnace solidification where the pulling rate is variable, i.e. transient solidification, and using the front tracking model (FTM) of McFadden and Browne [113]. Two key modifications are necessary to do this. Firstly, the numerical algorithm is updated to account for advection of heat through a fixed

domain as the sample moves. This means that the governing heat equation contains an extra term to deal with the translation of the sample. Secondly, the front position must be able to advance and retreat—within a fixed domain—given that the pulling rate is a function of time. These aspects and other important features of the model are expounded upon in the following sub-sections.

3.2.1 The heat equation

Considering internal heat flow in the axial direction only; the heat equation for a long cylindrical rod of uniform cross sectional area A, and perimeter p, moving at a pulling rate u along its axis, and transferring heat radially at its circumference to (or from) a surrounding heat sink (or source) with a heat transfer coefficient h, is given by,

$$\frac{\partial}{\partial t}(\rho c T) = \frac{\partial}{\partial x}\left(k \frac{\partial T}{\partial x}\right) - u\rho c \frac{\partial T}{\partial x} - \frac{hp}{A}(T - T_\infty) + E \quad , \qquad (3.2)$$

(adapted from [127] and [129]) where ρ, c and k are the density, specific heat capacity and thermal conductivity of the rod material respectively, T_∞ is the temperature of the surrounding source (or sink), and E is the latent heat generated per unit volume. The first term on the left hand side (LHS) is the time rate of change of sensible energy per unit volume. The first term on the right hand side (RHS) of this equation gives the diffusion of thermal energy by conduction in the axial direction per unit volume. The second term on the RHS is the change in thermal energy of a mass as it moves through space. (This term is not included in the McFadden and Browne FTM.) In other words, this term is the difference between the energy advected into and out of a fixed volume. The full derivation of equation (3.2) from first principles can be found in Appendix A.1.
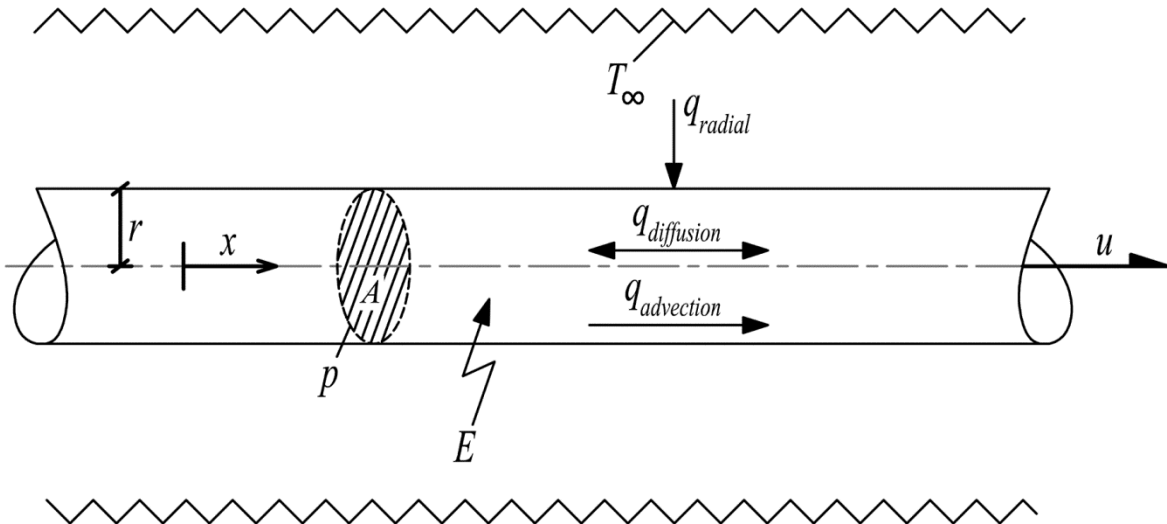
Fig. 3.1 Schematic of heat transfer occurring in a moving rod.

Figure 3.1 shows a schematic of the heat transfer scenario dealt with using equation (3.2). Note that the x-axis fixed to ground and aligned with the rod axis. The axial heat flux due to

diffusion in the rod is shown as $q_{diffusion}$ (acting in the positive and negative x-directions) and the axial heat flux due to advection is $q_{advection}$ (acting in the positive x-direction, i.e., same direction as the rod movement). A radial heat flux, q_{radial}, acts at the rod circumference at any position along its length that is surrounded by the heat source (or sink) having temperature T_∞. Finally, E in this is the latent heat released during a solidification process occurring within the rod.

In the simulations carried out in this chapter, the following Dirichlet boundary conditions are applied at the domain boundaries,

$$T(x,t) = \begin{cases} T\big|_{x=0} = T_H & \forall \quad t \\ T\big|_{x=\ell} = T_C & \forall \quad t \end{cases}, \tag{3.3}$$

In words, this means that the domain ends are maintained at a fixed temperature; T_H at the hot end and T_C at the cold end.

3.2.2 The domain

Figure 3.2 shows a 1-dimensional domain of a Bridgman furnace. The hot region is given by $0<x<x_1$, the adiabatic (or 'baffle') region by $x_1<x<x_2$ and the cold region by $x_2<x<\ell$. The hot region heater is held a temperature T_H and heat is transferred to the sample here, with heat transfer coefficient h_H. Similarly, the cold region heater is held at T_C and heat is transferred away from the sample here, with heat transfer coefficient h_C. Note that T_H or T_C replaces T_∞ in equation (3.2) depending on axial location and in the same manner h_H or h_C replaces h. In the adiabatic zone the heat transfer coefficient with the surroundings is zero.
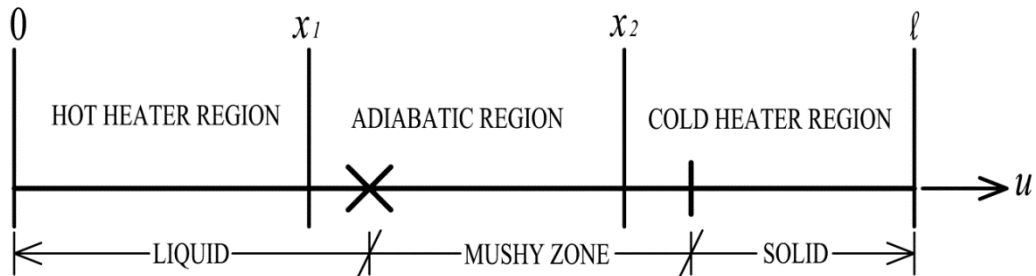
Fig. 3.2 Bridgman furnace front tracking model domain and co-ordinate system.

The domain is fixed in space, and the sample is being drawn through the fixed domain at some pulling rate u. The domain is divided into disc-shaped volumes of thickness Δx. The mush–liquid interface (the front) is shown in the domain given by a front marker (×).

This arrangement allows for the adiabatic zone to be any length (less than the domain length). Alternatively, the adiabatic zone can be eliminated, i.e., set to be an adiabatic point, by letting $x_1 = x_2$. In the numerical algorithm that follows, only the thermal history within the domain is recorded at every time step. As the sample gets passed out of the domain (beyond $x=\ell$) its temperature is no longer of concern since it is assumed that the material here is fully solid. This arrangement is suitable given that T_C is normally set below the liquidus temperature for the alloy. It

is possible that mush could exist beyond the domain extent; however, this can be dealt with by increasing the domain size or lowering T_C, accordingly.

3.2.3 The heat fluxes

Equation (3.2) can be numerically discretised using the control volume (CV) approach and written as a sum of heat flux terms where the sample is divided into disc shaped CVs, Δx metres wide, as shown in Fig. 3.3(a). The resulting explicit solution is given as follows:

$$\frac{\rho c \Delta x}{\Delta t}\left(T_i^{m+1} - T_i^m\right) = q_{i-1} + q_{i+1} + q_{adv} + \Delta x \frac{2}{r_2} q_2 + q_a + q_t \quad , \tag{3.4}$$

where the term in parentheses is the change in temperature at any CV, for example, the CV labelled 'i' in Fig. 3.3 (b), during a time Δt. See Appendix A.2 for a full derivation of equation (3.4).
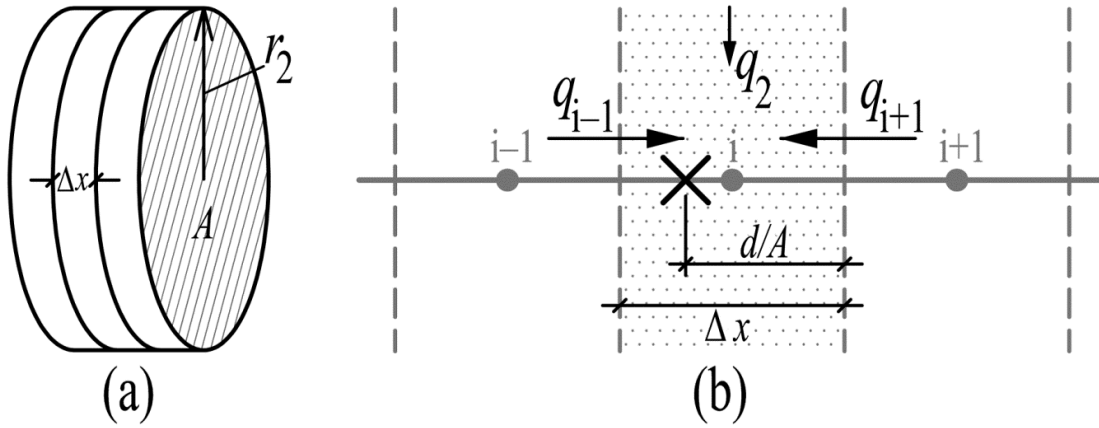
Fig. 3.3 (a) Disc shaped control volumes (b) control volume with heat flux shown.

The temperature of the CV labelled 'i' is T_i and the superscripts 'm' and '$m+1$' refer to the present and future temporal locations in the algorithm, respectively. The temperatures of the CVs on the west and east sides of the CV labelled 'i' are given by T_{i-1} and T_{i+1} respectively.

The heat fluxes due to thermal diffusion across the west and east faces of the CV in Fig. 3.3 (b) are given by q_{i-1} and q_{i+1}, respectively, and are calculated using the following finite difference equations:

$$q_{i-1} = k\left(\frac{T_{i-1}^m - T_i^m}{\Delta x}\right) \quad , \tag{3.5}$$

$$q_{i+1} = k\left(\frac{T_{i+1}^m - T_i^m}{\Delta x}\right) \quad . \tag{3.6}$$

The advection heat flux q_{adv} is the difference in thermal energy advected into and out of a CV during one time step, while the sample is moving at a pulling rate u, and is given by,

$$q_{adv} = -\frac{\rho c u}{2}\left(T_{i+1} - T_{i-1}\right) \quad . \tag{3.7}$$

The radial heat flux q_2—occurring at the circumference of the CV—is related to the heat transfer coefficient h, and the surrounding temperature of the source (or sink) T_∞ as follows:

$$q_2 = -h\left(T_i^m - T_\infty\right) \quad , \tag{3.8}$$

where the subscript '2' refers to the circumference of the disc shaped CV such that $p=2\pi r_2$ and $A=\pi(r_2)^2$ so that; $p/A=2/r_2$.

The latent heat term, E, in equation (2.17)—from the McFadden and Browne FTM, refer to Section 2.6.5—is expanded and discretised to give the latent heat flux terms; q_a and q_t. Given that the volume of solid, V_S, is equal to the captured volume of mush, d, multiplied by the volumetric fraction of solid, g_S, i.e., $V_S=g_S d$, then it follows that; $\partial V_S/\partial t=g_S(\partial d/\partial t)+d(\partial g_S/\partial t)$. Discretising the derivative terms and substituting into equation (2.17) yields: $E=(q_a+q_t)/\Delta x$, where;

$$q_a = \frac{\rho L_M}{V_{CV}} g_S^m \left(\frac{d^{m+1} - d^m}{\Delta t}\right)\Delta x \quad , \tag{3.9}$$

$$q_t = \frac{\rho L_M}{V_{CV}} d^m \left(\frac{g_S^{m+1} - g_S^m}{\Delta t}\right)\Delta x \quad . \tag{3.10}$$

The subscripts 'a' and 't' refer to the advancement of the front, and thickening of the mush behind the front, respectively. When the front marker (×) is in a CV, as shown in Fig. 3.3, the captured volume of mush in that CV is given by the volume d, and the position of the marker is given by the distance d/A, where A is the cross sectional area of the CV.

The heat flux due to the advancement of the front, q_a, can be directly calculated using simple dendrite kinetics. However, to calculate the heat flux due to thickening of the mush, q_t in equation (3.10), and when using the Scheil relation for g_S, equation (2.22), the volumetric fraction of solid at the future time step, g_S^{m+1}, is unknown, since it is a function of the *future* local CV temperature, T_i^{m+1}. Therefore, to solve for T_i^{m+1} in equation (3.4), a Newton–Raphson iteration scheme is used to estimate q_t in mushy CVs as per the method described in Section 2.6.5.

3.2.4 Movement of the front

Bidirectional requirement

The BFFTM model is designed for bidirectional movement of the front within the fixed domain, i.e., the front can move in the positive *x*-direction *and* negative *x*-direction during one time step of the numerical algorithm. Previous front tracking models [113][114] are designed to only *advance* the mush–liquid interface within the domain; there is no way (or need) in these models to decrease

41

the captured volume of mush. In Bridgman solidification, however, bidirectional movement of the front is a necessity (when using in a fixed grid) since the pulling direction is in opposition to the growth direction. This is dealt with by updating the front position due to dendritic growth (in the negative x-direction, see Fig. 3.2), and due to translational movement of the crucible through the furnace (in the positive x-direction, Fig. 3.2), separately, and in sequence, during each time step of the numerical algorithm. This means that latent heat released due to the advancement of the front is calculated based on the change in front position (and hence change in volume) due to *growth* in a moving solid, as opposed to the overall change in front position with respect to the fixed grid.

The BFFTM uses the same approach to dendrite kinetics as the front tracking model outlined in Section 2.6.4, i.e., a power law function of undercooling is used to calculate the growth rate, equation (2.16). In the BFFTM, however, the axial position of the front relative to the fixed domain, x, must account for the growth rate of the columnar tip (v_{tip}) and the pulling rate due to the movement of the sample (u), and is calculated as follows:

$$x^{m+1} = x^m + \left(u - v_{tip} \right) \Delta t \quad , \tag{3.11}$$
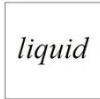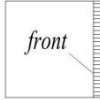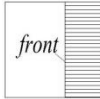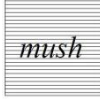
where x^m and x^{m+1} are the axial positions of the front at present and future time steps in the numerical algorithm, respectively. Note that u and v_{tip} always exist in opposing directions, and that the front will appear (from the point of view of the fixed grid) to move with the sample when $u > v_{tip}$, and vice versa when $v_{tip} > u$. The value for u can be pre-determined or set to be a function of time, for example, a ramp or step input.

Status flags

The resulting front position is recorded and used to identify a particular scenario or 'status' flag for each CV, individually. The CV status then identifies whether or not the latent heat fluxes q_a and q_t are active for that CV at that time step. Table 3.1 shows all the possible scenarios (status flags) that a CV can encounter, all of which depend on the front position. Note that the other heat fluxes, equations (3.5), (3.6), (3.7) and (3.8), do not depend on these status flags and are applied in the algorithm regardless of front position.

Figure 3.4 illustrates the typical progress of the front marker and the status flag at each CV during successive time steps. At time $= t$ the front is in CV 'i' with status (3) and is growing in the negative x-direction. In this scenario both latent heat fluxes are active since the front is advancing and the mush is thickening. As the front grows into CV 'i-1', at time $= t + \Delta t$, the status is changes to (2), since it is the first time the front has entered that CV, i.e., only advancement is occurring so only q_a is active.

Table 3.1 Control volume status flags used to activate latent heat flux.

Status flag	State	Illustration	Value of q_a and q_t
(1)	fully liquid	*liquid*	$q_a = q_t = 0$
(2)	front in the CV for the first time, partial mush	*front*	$q_a \neq 0, q_t = 0$
(3)	front in the CV, partial mush	*front*	$q_a \neq 0, q_t \neq 0$
(4)	front has passed the CV, fully mush	*mush*	$q_a = 0, q_t \neq 0$
(5)	fully solid	*solid*	$q_a = q_t = 0$
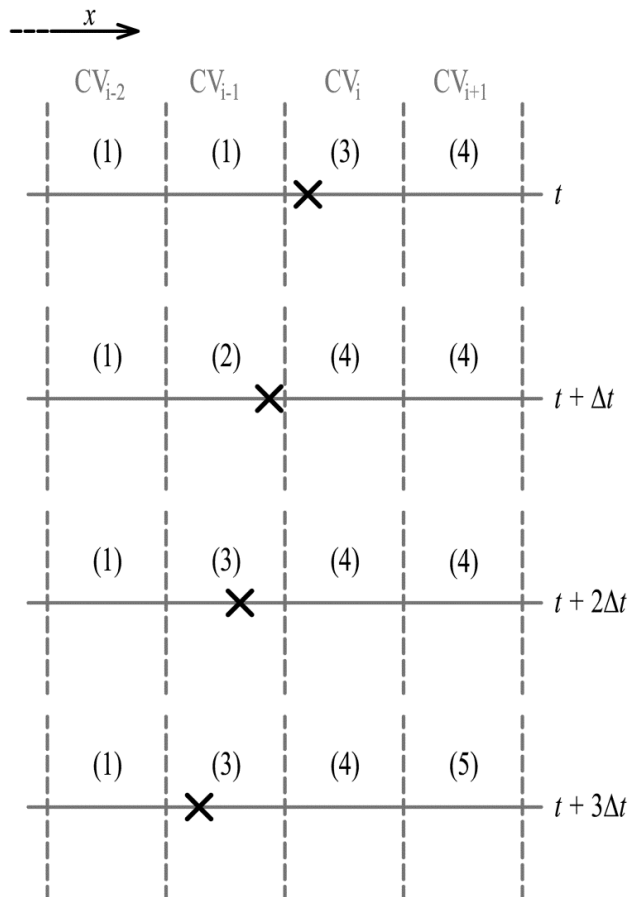
Fig. 3.4 Typical progress of the columnar front marker with status flag values shown.

At the next time step, time = $t + 2\Delta t$, this same CV changes to status (3) and so on. CVs immediately to the right of the CV containing the front will have status (4) since the CV is fully

43

mush and only thickening occurs, i.e., only q_t is active. Where the temperature of a fully mush CV drops below the equilibrium solidus temperature, T_s, the status changes to (5) as illustrated in the figure in CV 'i+1' at time $= t + 3\Delta t$.

3.2.5 Nucleation, thermophysical properties, and numerical stability

The BFFTM uses the same nucleation criterion for columnar growth as the front tracking model as outlined in Section 2.6.2. Only one seed location, however, can be specified given the 1-dimensional nature of the problem. The seed may be placed anywhere in the domain from 0 to ℓ.

The BFFTM uses the same method of calculating the thermophysical properties as the front tracking model outlined in Section 2.6.7.

The BFFTM uses an explicit numerical method. The following condition is checked to ensure numerical stability at every time step, after [130] as follows:

$$\Delta t < \frac{\rho c (\Delta x)^2}{2k} \quad .$$

(3.12)

3.2.6 Code structure

The BFFTM is written in FORTRAN 90 with double precision used for all real variables. The code is divided into five subroutines; each deals with a major task required per pass through the time loop. The code is presented in a simplified flowchart form in Fig. 3.5. The subroutines are labelled 1-5.

All variables are initiated before entering the time loop. Once the value for time is less than the end time, the algorithm continues to cycle through subroutines 1-5. The first subroutine checks for nucleation; the temperature at the seed position is checked against the nucleation undercooling value, and will nucleate if it satisfies the pre-set criterion. Once nucleated the algorithm skips this subroutine thereafter.

The second subroutine updates the front position. The dendrite tip growth rate calculation requires the undercooling at the tip. This is calculated, for any given front position, by linear interpolation of temperature between CV centres to get the tip temperature (i.e., at the front), and hence undercooling. The pulling rate is predefined. The net change in front position, $(u-v_{tip})\Delta t$, is then calculated, and added to previous front position, as per equation (3.11) in this subroutine.

In the third subroutine, the change in captured volume of mush is calculated for each CV. The fourth subroutine determines what status should be assigned to each CV, based on; front position and solid fraction, in that order. This subroutine is designed such that a CV must progress from one status to the next in the correct order, i.e., 1-2, 2-3, 3-4 and 4-5. It also allows for the reversal of the front relative to the domain, i.e., when $u > v_{tip}$, by the following permitted status

44

changes; 2-1, 3-1, 4-1, 5-1, 4-3 and 5-4. The solid status (5) is determined solely on solid fraction, i.e., a solid fraction of unity gives status (5).

```
                        ┌─────────────┐
                        │    start    │
                        └──────┬──────┘
                               ▼
                        ┌─────────────┐
                        │ initiate    │
                        │ variables   │
                        └──────┬──────┘
                               ▼
                          ◇ time < endtime ◇  ──No──►
                               │ Yes
                               ▼
                  ┌─1─────────────────────────┐
                  │   check for seed nucleation │
                  └───────────┬────────────────┘
                              ▼
                  ┌─2─────────────────────────┐
                  │ update the front marker position │
                  └───────────┬────────────────┘
                              ▼
                  ┌─3─────────────────────────┐
                  │ calculate new captured volume │
                  └───────────┬────────────────┘
                              ▼
                  ┌─4─────────────────────────┐
                  │   update the CV statuses    │
                  └───────────┬────────────────┘
                              ▼
                  ┌─5─────────────────────────┐
                  │ update the temperature distribution │
                  └───────────┬────────────────┘
                              ▼
                  ╱ output the temperature at set intervals ╱
                              ▼
                        ┌─────────────┐
                        │ update the  │
                        │    time     │
                        └─────────────┘
                    time loop
                        ┌─────────────┐
                        │     end     │
                        └─────────────┘
```
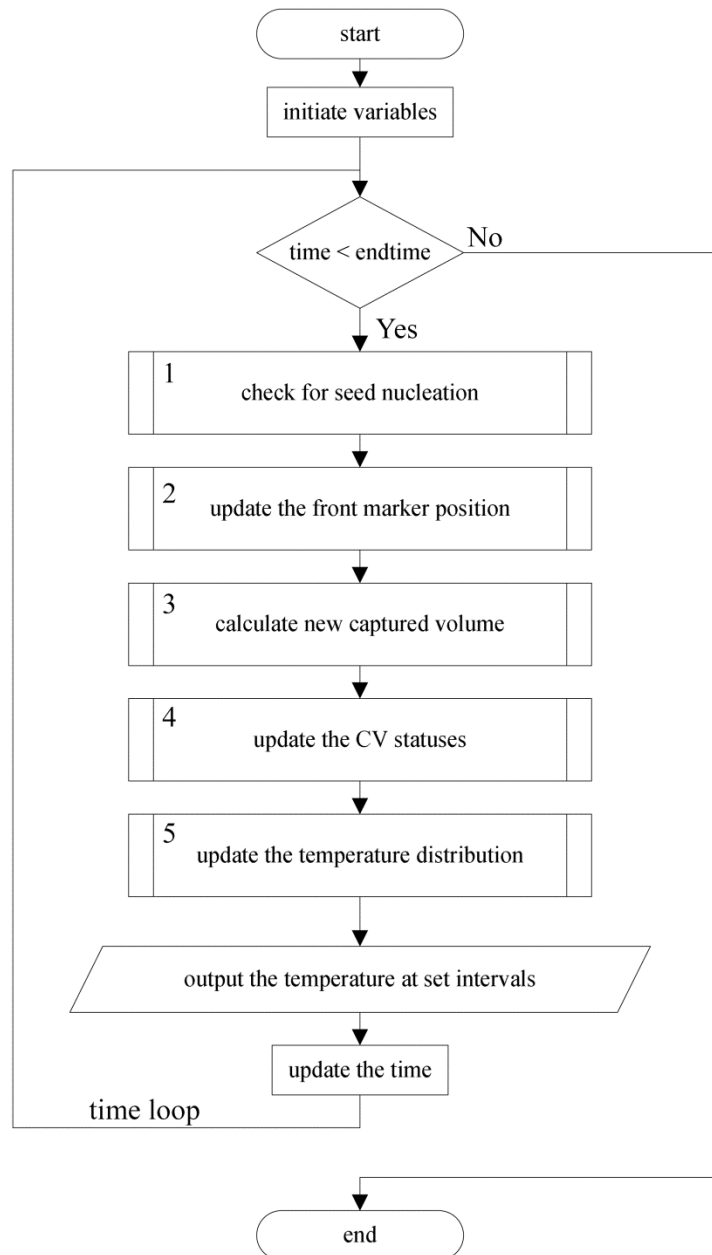
Fig. 3.5 Bridgman furnace front tracking model algorithm flowchart.

The fifth (and final) subroutine is by far the most involved. Initially it calculates the material properties at each CV using a polynomial function of temperature specific to the simulation alloy, as per Section 2.6.7. (However, the code is designed such that the user can switch between fixed and variable properties as required.) Next the conduction, advection, and radial heat fluxes are calculated in series for each CV. With regard to the fraction of solid calculation, the model allows the user switch between a linear function of temperature, as in equation (2.22), a Scheil type function, as in equation (2.21), or a user-defined lookup table. Finally, the algorithm calculates each CV temperature for the following time step by the solution to equation (3.4).

The code repeats subroutines 1-5 until the time exceeds the end time for the simulation. The code is written such that the user specifies how many output data files are required. The temperature at each CV is recorded at suitable equal intervals to achieve the desired number of output files and the sequential time step number for each file is stored as part of the '.txt' file name. The maximum number of time steps that can be requested is 100 billion. Other output data is also recorded at these time intervals as follows: front position, dendrite tip growth rate, dendrite tip temperature, temperature gradient at the tip, mush width, Biot number at each CV, and all of the heat fluxes values at each CV. In addition, the user may specify one particular CV of interest to get the following data from that CV at each of the data output intervals; solid fraction, temperature, total enthalpy, flag status, and cooling rate.

Finally, the code uses an error reporting system that stops the program with an error message, while preserving the run data. Typical traceable errors include; 'numerical scheme instability', 'Biot number too high', 'non-convergent iteration scheme', 'user input error', and 'too many output files requested'.

3.3 Modelling Bridgman Solidification of Al−7wt.%Si

Al−7wt.%Si was chosen as a suitable hypoeutectic binary alloy, for the purposes of simulation modelling, since it is well documented in the literature, for example by Gandin [47][57], and also because it has been modelled previously using the McFadden and Browne FTM, in references [113] and [56].

3.3.1 A transient solidification problem

A notional problem is designed for the purpose of demonstrating the transient solidification facility of the BFFTM. Two scenarios are simulated. In the first simulation ('Simulation 1') the initial temperature distribution is linear in the adiabatic zone and held constant in the hot and cold regions. The sample pulling rate is set to zero. Given this initial condition, the temperature profile in the sample is then permitted to find a steady-state. In the second simulation ('Simulation 2') the initial temperature profile is given by the final (steady-state) temperature profile from Simulation 1. The pulling rate then undergoes two separate step changes. The subsequent change in front position and temperature profile is observed.

3.3.2 Properties of Al−7wt.%Si

The material selected for modelling was Al−7wt.%Si. Material properties for this binary hypoeutectic alloy are taken from the study by McFadden et al. [56] where polynomial functions of temperature are used to estimate the materials' density ρ, volumetric heat capacity ρc, and thermal conductivity k, using equation (2.30). The polynomial coefficients for this alloy, as well as other important thermodynamic and dendritic growth data, used in the simulations, are given in Table 3.2.

Table 3.2 Material properties for Al–7wt.% Si [56].

Property	Units	Coef.	Liquid	Solid
Volumetric heat capacity, ρc	[J/m^3]	a_0	3.06×10^6	2.349×10^6
		a_1	-324.7	972
		a_2	0	0
Thermal conductivity, k	[W/m·°C]	a_0	44	1.3581
		a_1	0.022747	0.2284
		a_2	0	-3.840×10^{-5}
Density, ρ	[kg/m^3]	a_0	2370	2535
		a_1	0	0
		a_2	0	0
Equilibrium liquidus temperature, T_l	[°C]		618	
Equilibrium eutectic temperature, T_{euc}	[°C]		577	
Melting temperature of pure Al, T_m	[°C]		660.2	
Partition coefficient, k_{part}	[–]		0.13	
Volumetric latent heat of fusion, L_V	[J/m^3]		1064×10^6	
Dendrite growth constant, C	[m/°C^b]		2.9×10^{-6}	
Undercooling exponent, b	[–]		2.7	

3.3.3 Simulation details

The hot heater temperature T_H, and cold heater temperature T_C, are set at 50 °C above the alloy equilibrium liquidus temperature T_l, and 50 °C below the alloy equilibrium eutectic temperature T_{euc}, respectively. The heat transfer coefficient in the hot and cold zones is set to a high value, $h_H=h_C=1500$ W/m^2·°C, which is in keeping with the Biot number requirement for the model, i.e., $Bi < 0.1$. Referring to Fig. 3.2 and Fig. 3.3, the domain length is set at 100 mm, sample radius is set to 8 mm, and the adiabatic zone length is fixed at 20 mm (such that $x_1 = 40$ mm and $x_2 = 60$ mm).

Two simulations are carried out. In Simulation 1, the initial temperature profile is set (arbitrarily) to equal to the hot and cold heater temperatures, in the hot and cold regions, respectively; and vary linearly between these temperatures in the adiabatic region. The pulling rate in Simulation 1 is fixed to zero. The simulation time is set to 300 s. The model finds a steady-state temperature profile in this time.

In Simulation 2, the steady-state temperature profile from Simulation 1 is used as the initial temperature profile. In Simulation 2, the pulling rate undergoes a step change at a time $t =100$ s of $u = 0 \rightarrow 0.5$ mm/s, followed by another step change in pulling rate at a time $t = 500$ s of $u = 0.5 \rightarrow 1$ mm/s. The simulation time is set to 1000 s in this case. The model finds a steady-state temperature profile in this time.

In both simulations the numerical time step is set at $\Delta t = 0.75 \times 10^{-3}$ s which satisfies the stability criterion given by equation (3.12). The columnar nucleation undercooling is set to 1 °C

which is in keeping with the work of McFadden et al. [56] in simulations using the same alloy composition. In both simulations, the seed is located at the centre of the CV having an initial temperature just below the temperature at which nucleation would occur (i.e., in this case, just below 617 °C). This was done so that the model nucleated the seed at time $t = 0$ s, and so that the CV flag status array—referred to in Section 3.2.4—was populated appropriately for the given scenario.

3.4 Modelling Results

3.4.1 Grid convergence study

A grid convergence study was carried out according to the method outlined by De Vahl Davis [131]. In this method, simulations are performed at three different grid sizes—i.e., using three different CV widths—and the difference between the results is used to find the order of error, n, for the numerical procedure (without a requirement for an exact solution) as follows:

$$n = \ln\left(\frac{T_{sim_{\Delta x_1}} - T_{sim_{\Delta x_2}}}{T_{sim_{\Delta x_2}} - T_{sim_{\Delta x_3}}}\right) \bigg/ \ln(\lambda) \quad , \tag{3.13}$$

where T_{sim} is the numerical solution given by equation (3.4), Δx_1 is the finest grid resolution, and λ is the refinement ratio, such that, $\lambda = \Delta x_1/\Delta x_2 = \Delta x_2/\Delta x_3$. Table 3.3 summarises the results obtained.

Table 3.3 Grid convergence study results.

CV Width [mm]			Truncation error order
Δx_1	Δx_2	Δx_3	n
5	10	20	0.5707
2.5	5	10	0.6559
1	2	4	0.9998

The above results demonstrate grid independence for CV widths of 2 mm or less. In other words, the order of error in the numerical procedure has converged to ≈ 1. (See Chapter 4 for further analysis of error in the BFFTM.) A factor of safety of four was applied in simulations that follow; Δx was conservatively set to 0.5 mm.

3.4.2 Simulation 1: Results

The evolution of the temperature profile in the sample, for Simulation 1, is shown in Fig. 3.6. The initial temperature profile for the simulation is labelled as $T_{initial}$ and the final steady-state temperature profile is shown as T_{steady}. The adiabatic zone start and finish positions, x_1 and x_2, are shown in the figure.
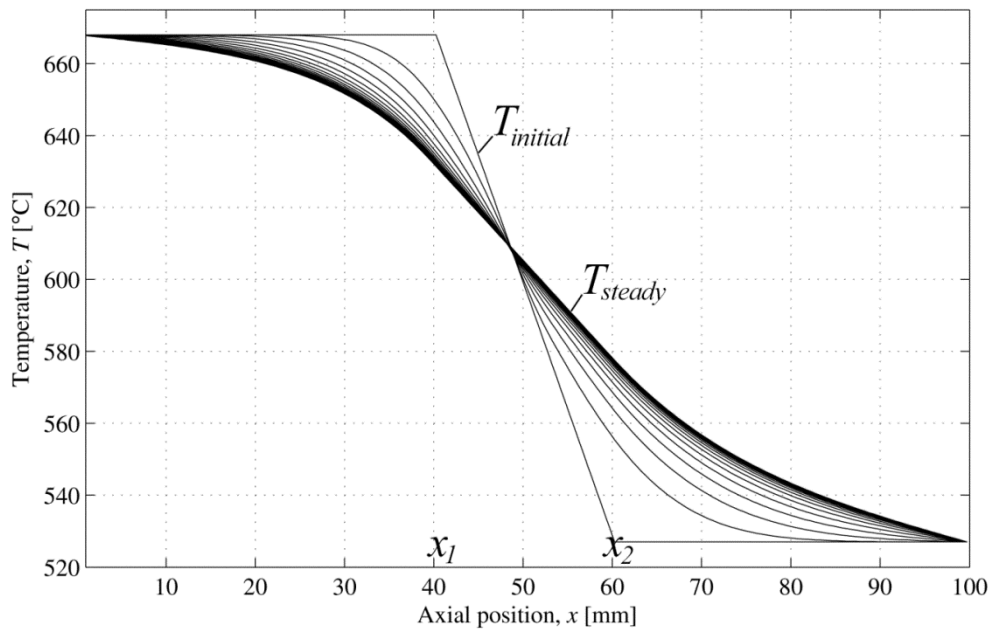
Fig. 3.6 Simulation 1: Evolution of a steady-state temperature profile.

Figure 3.7 shows the corresponding thermal history (solid lines) for this simulation at positions in the adiabatic region of the domain, x = 44 mm, 46 mm, 48 mm, 50 mm, 52 mm, 54 mm and 56 mm. The dashed line shows the progression of the front marker in terms of axial position, x, plotted as a function of time with the axial position on the right hand side y-axis of the figure.
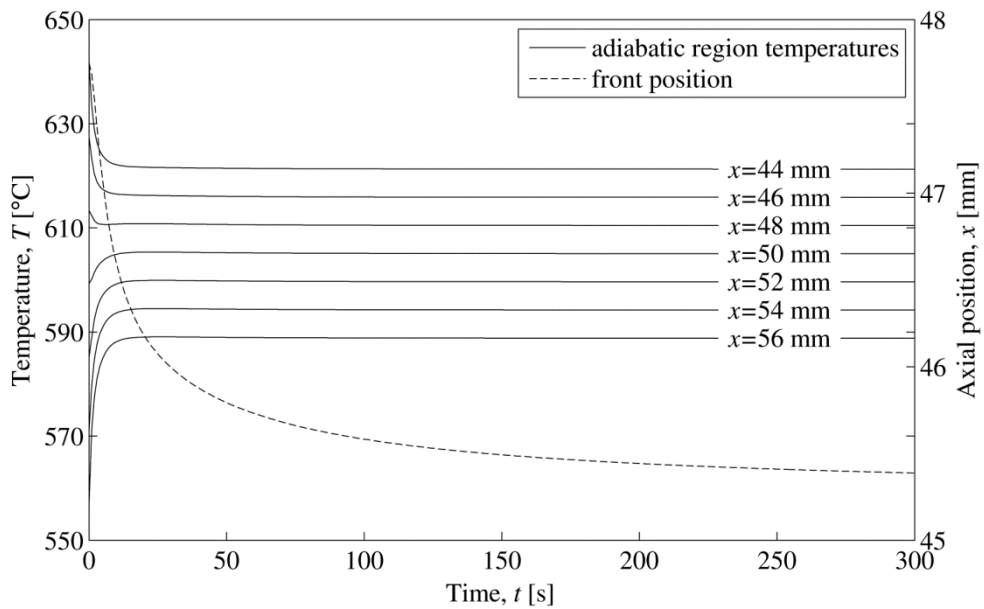
Fig. 3.7 Simulation 1: Thermal history in the adiabatic zone and change in front position.

3.4.3 Simulation 2: Results

The evolution of the temperature profile in the sample, for Simulation 2, is shown in Fig. 3.8. The initial temperature profile for the simulation is labelled as $T_{initial}$. (Note that this is equal to

49

T_{steady} from Simulation 1.) The final steady-state temperature profile is for this simulation is shown as T_{final} in the figure.
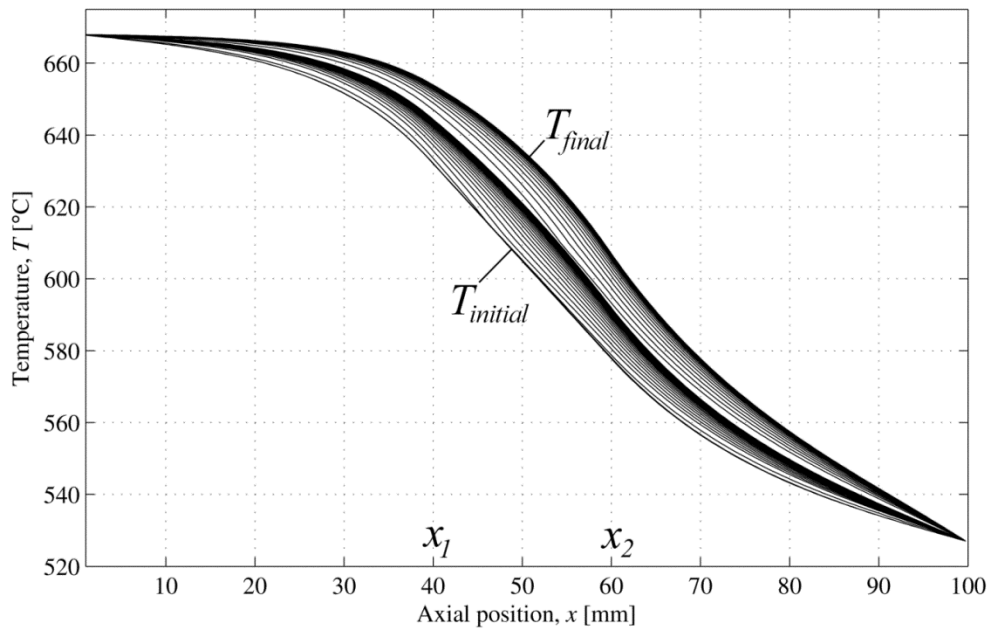
Fig. 3.8 Simulation 2: Evolution of temperature profile with two step changes in pulling rate.
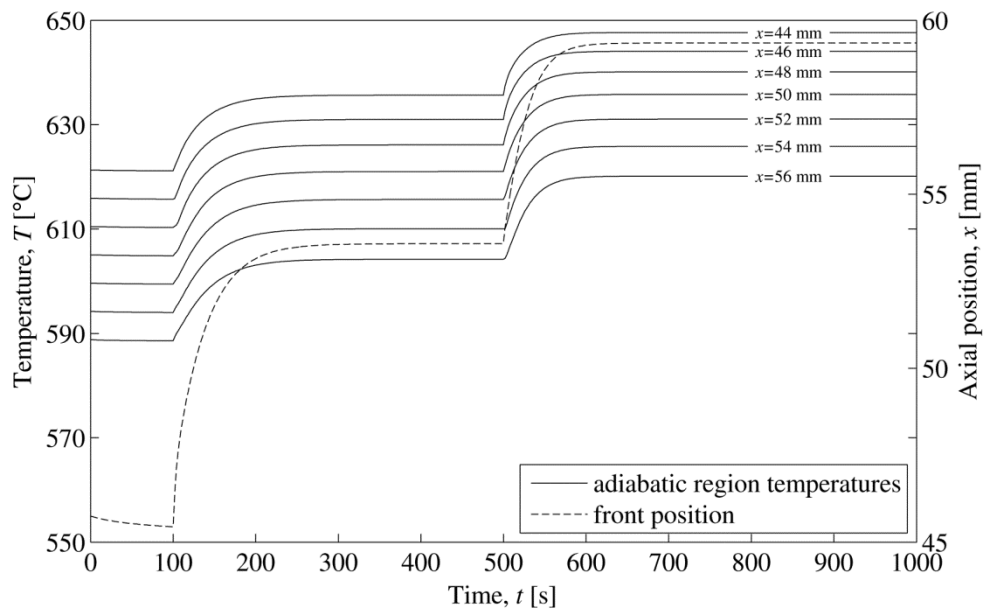
Fig. 3.9 Simulation 2: Thermal history in the adiabatic zone and change in front position.

Figure 3.8 shows the corresponding thermal history (solid lines) for this simulation at positions in the adiabatic region of the domain, x = 44 mm, 46 mm, 48 mm, 50 mm, 52 mm, 54 mm and 56 mm. The dashed line shows the progression of the front marker in terms of axial position, x, plotted as a function of time with the axial position on the right hand side y-axis of the figure.

3.5 Discussion

In the results for Simulation 1, i.e., Fig. 3.6 and Fig. 3.7, where the pulling rate is set to zero, it is shown how the sample temperature profile and front position settle—from an arbitrary initial state—to a steady-state. This simulation result is of practical importance as it calculates the an estimate for the initial condition of a real Bridgman furnace experiment before pulling of the sample begins. The final temperature profile for Simulation 1 is the starting temperature profile for Simulation 2.

In the results for Simulation 2, the effect of suddenly changing the pulling rate is observed. The temperature profile undergoes a net increase in temperature due to new advection heat flux from the hot heater zone as a result of the change in pulling rate. The reaction of the front position is typical of a first-order type response to a step input. The front reaches a steady-state, i.e., when the front growth rate and pulling rate eventually match, and the temperature profile does not change with respect to time within approximately 100 s after each step change. The net effect of increasing the pulling rate was to increase the dendrite tip undercooling and the volume of undercooled liquid ahead of the front. This scenario is useful in that these conditions could produce a columnar to equiaxed transition (CET) in a Bridgman furnace experiment.

3.6 Conclusion

The method used to adapt the FTM of McFadden and Browne [113] to model columnar growth in the Bridgman method is fully described. The resulting model is appropriate for processes with a low Biot number. Issues relevant for front tracking, as applied to Bridgman solidification and not dealt with before in the McFadden and Browne FTM, are explained in terms of their solution and implementation. For example, the method to correctly calculate latent heat release where bi-directional movement of the columnar front occurs during one numerical time step is provided.

Bridgman furnace solidification of the binary hypoeutectic alloy; Al–7wt.%Si, was simulated. This was chosen for simulation modelling since the McFadden and Browne FTM has been implemented previously for hypoeutectic compositions and this particular alloy has been modelled significantly in the literature. A double jump in pulling rate is simulated and conditions to promote a CET are apparent. The simulations demonstrate the transient capability of the model.

The simulation approach is useful in that the initial condition, i.e., the temperature profile in the sample, is not assumed *a priori*; rather it is calculated based on furnace conditions (heat transfer coefficient) that can be measured separately.

This chapter satisfies Objective 1 of this thesis, as given in Section 1.2. Now that the BFFTM algorithm has been developed and demonstrated, it is appropriate to look at a method of verification for the model.

Chapter 4

Order Verification

In this chapter, an order verification procedure is applied to the BFFTM in a simple solidification scenario: steady solidification (i.e., at a fixed pulling rate, u) of pure titanium. Verification exercises require analytical solutions from the literature—for comparison purposes—which is what restricts this particular exercise to a *steady* process involving a *pure* material. Further verification modelling, e.g., *transient* solidification of an *alloy*, would require appropriate analytical solutions from the literature (presently not available). However, this chapter details the first step in the broad task that is verification for the BFFTM. Referring to Section 1.2, this chapter addresses the second objective of this thesis. Reference [132] is the main source of the content for this chapter.

4.1   Definition of 'Verification'

The word verification (from Latin, *verus*, meaning true) is defined as the act of demonstrating truth or correctness by comparison to fact, theory, or statement [133]. In numerical modelling, *verification* refers to the process by which one demonstrates that a partial differential equation (PDE) code correctly solves its governing equations [134]. This process involves comparison of numerically simulated results with a known analytical (exact) solution to the PDE. The numerical model is verified if this comparison is adequately close. In other words, the numerical model accurately solves the equations that constitute the mathematical model. Model verification is not to be confused with model *validation*. Boehm [135] and Blottner [136] define verification as "solving the equations right", and validation as "solving the right equations". Model validation should be carried out after successful model verification, and usually involves comparison of numerically simulated data with experimental data, in order to confirm that the PDE being solved is representative of the real system being modelled. Note that there are differences in opinion regarding these definitions in the literature and, for the purposes of this thesis, the methodology of Roache [137] is adopted.

4.2   Order Verification Method

The formal order verification procedure used in this chapter was first implemented by Steinberg and Roache [138]. A summary of the procedure is given by Knupp and Salari [134]. The method focuses on order of accuracy. Under this method, a numerical model is verified when; the

observed order of accuracy from simulated results matches the theoretical order of accuracy of the governing partial differential equation, upon which it is based; given that the model is *consistent* and *convergent*.

4.2.1 Theoretical order of accuracy

The discretisation of the governing PDE gives the theoretical order of accuracy of the model. The PDE is broken down into estimations of each partial derivative using a truncated Taylor series expansion for each derivative term, yielding simple finite difference equations. The truncation error is the difference between the actual value for the derivative term and the estimated value using the difference equations, and can readily be written in terms of the grid resolution. One can then state the theoretical order of accuracy of the discretisation method by looking at the power to which the grid resolution is held in the leading term of the truncation error. For example, considering a one-dimensional domain with grid resolution Δx, the Taylor series expansion for a second order partial derivative of the dependant variable T, in respect of the spatial variable x, is given by;

$$\left.\frac{\partial^2 T}{\partial x^2}\right|_i = \underbrace{\frac{T_{i-1} - 2T_i + T_{i+1}}{(\Delta x)^2}}_{approximation} + \underbrace{O(\Delta x)^2}_{truncation} \quad , \tag{4.1}$$

where subscript 'i' refers to a central node or control volume location in the domain. The first term on the right hand side (RHS) of equation (4.1) is the finite difference approximation of the second order partial derivative, while the second term on the RHS is the truncation error. The truncation error is the sum of the terms excluded from the Taylor expansion for the second order partial derivative, i.e., $O(\Delta x)^2 = ((\Delta x)^2/4!)d^4 T/dx^4 + higher\ order\ terms$, as shown by Özışık [139]. In this case, the lowest power of Δx in the leading term of the truncation is two; therefore the theoretical order of accuracy for this discretisation method is second order. Where a PDE contains multiple derivative terms, the lowest power of Δx in the leading term of the truncation—across all partial derivative terms in the PDE—gives the overall theoretical order of accuracy for the model. Boundary conditions also effect the model order of accuracy.

4.2.2 Observed order of accuracy

The observed order of accuracy of the model is determined by comparing the simulated results for an arbitrary test problem at two grid resolutions with a known analytical solution. The difference between the simulated results and the analytical solution is known as the *numerical* error, made up primarily by the truncation error (sometimes called discretisation error), plus the round off error associated with the algorithm software, plus any iterative convergence error. Round off errors are usually negligible relative to the truncation error and iterative convergence error occurs only with implicit finite difference solvers that require a statement of solution tolerance [140].

The numerical solution gives a value for the dependant variable T_i^{num} at distinct locations in the modelled domain. The analytical solution—which is continuous—is evaluated at the same locations to give T_i^{exact}. The local numerical error NE_i^{local} can be calculated by their difference, at each discrete position as follows:

$$NE_i^{local} = T_i^{exact} - T_i^{num} \quad .$$

(4.2)

Where the numerical scheme uses a fixed grid resolution, it is useful to calculate the global numerical error NE^{global} as follows:

$$NE^{global} = \sqrt{\frac{1}{N_{CVs}} \sum_i^{N_{CVs}} \left(T_i^{exact} - T_i^{num} \right)^2} \quad ,$$

(4.3)

where N_{CVs} is the total number of control volumes or mesh nodes. (This is also known as the l_∞ norm of the numerical error.) The observed order of accuracy for the numerical scheme, p_o, is calculated using the global numerical error at two grid resolutions, Δx_1 and Δx_2, as follows [134]:

$$p_o = \frac{\ln\left(\dfrac{NE_{\Delta x_1}^{global}}{NE_{\Delta x_2}^{global}} \right)}{\ln\left(\dfrac{\Delta x_1}{\Delta x_2} \right)} \quad .$$

(4.4)

4.2.3 Order verification procedure

The verification procedure is illustrated by the flowchart in Fig 4.1. Firstly, the theoretical order of accuracy of the model is determined via its governing equations and the finite difference scheme used in the model. Secondly, a test problem is designed. This is where the model is constrained to solve the modelling scenario of interest by setting the boundary conditions; Dirichlet, Neumann or Robin, and other factors required to define the problem. While the physical properties of the material are required in this step—in order to run the numerical model later—they are arbitrary in terms of the success of the order verification procedure itself. Thirdly, an exact solution to the PDE of interest must be found. Following this, the code is run at two different grid resolutions. The results from these simulations are used in the next step to calculate the observed order of accuracy, i.e., via equations (4.3) and (4.4). If the observed order of accuracy does not match the theoretical order of accuracy, one must go back through the code to look for coding errors before re-running the code at two grid resolutions, and so on until the code is verified.

As mentioned at the beginning of Section 4.2, for this verification procedure to be successful, it is taken that the numerical model being treated is *consistent* and *convergent*. The Lax–Rychtmyer [141] theorem, summarised as follows:

$$\text{consistency} + \text{stability} \Leftrightarrow \text{convergence} \quad ,$$

54

helps to explain how consistency and convergence are related in finite difference methods. A finite difference scheme is convergent if and only if the numerical scheme is stable and consistent; the converse also being true, a convergent scheme must be stable and consistent. Ultimately, for a scheme to be *stable* the numerical error for that scheme must not amplify without bounds [139]. This is normally dealt with by using a suitably small spatial grid and time step combination to satisfy a defined mathematical stability criterion. Consistency means that, as the as the spatial or temporal step size approaches zero, the finite difference approximations for the derivative terms in the governing equation should become arbitrarily close to the real derivative values. One may surmise that any finite difference scheme, applied using Taylor series' approximations for the partial derivative terms, is consistent; however, this is not always the case. An interesting example being the Du Fort–Frankel scheme [142] which is inconsistent even though it is unconditionally stable.
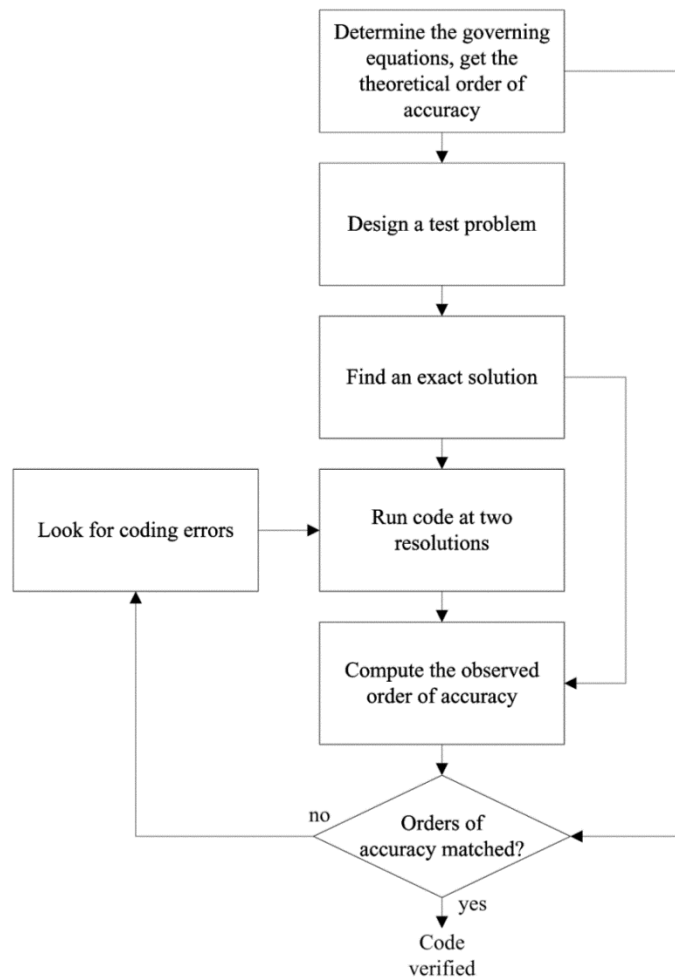
Fig. 4.1 Code verification procedure, adapted from Knupp and Salari [134].

With reference to the verification procedure outlined here, the numerical model is consistent when the value calculated for p_o is greater than zero. This means that the continuum PDE equation is recovered as $\Delta x \rightarrow 0$. In all simulations that follow, the spatial and temporal step sizes used obey the numerical scheme stability criterion, i.e., equation (3.12).

4.3 Bridgman Solidification

In this section a Bridgman furnace arrangement is described. This is followed by details of a particular problem to be solved as part of the order verification procedure, i.e., a test problem is defined in terms of boundary conditions, thermophysical properties, and other input data required for modelling.

4.3.1 The Bridgman procedure

A schematic of a Bridgman furnace is shown in Fig. 4.2. The furnace is tubular and made up of three zones: a hot zone with heater held at a temperature, T_H, having a heat transfer coefficient with the sample, h_H; an insulated adiabatic zone (shown hatched) of length, L_A; and a cold zone with heater held at a temperature, T_C, having a heat transfer coefficient with the sample, h_C. Normally, the hot and cold zones have differing heat transfer coefficients (depending on the apparatus), and the hot zone is held at a temperature above the liquidus or melting temperature of the sample material, while the cold zone is held at a temperature below the material solidus or melting temperature. A cylindrical sample with radius, r, is contained in a hollow thin walled crucible. Both are translated at a fixed pulling rate, u, through the furnace. The heaters impose a fixed temperature gradient in the sample (long curved line) as it is passed through the furnace.
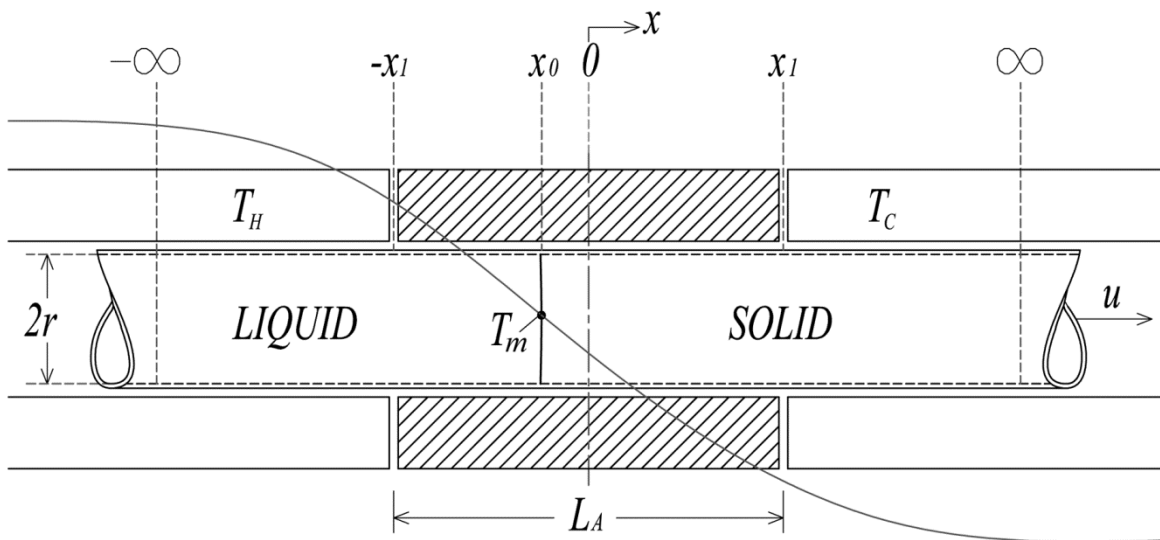
Fig. 4.2 Schematic of a Bridgman furnace.

A solidification interface is formed at some position in the adiabatic zone where the temperature is equal to the material melting temperature, T_m. In steady solidification, the position of the interface and the temperature profile is stationary relative to the furnace, which is fixed to ground.

Note that the sample and crucible are shown to be infinitely long in the figure. In reality a sample and crucible would have a fixed length, however—for the purposes of developing an analytical model—the rod is treated as infinite.

4.3.2 The test problem

The modelling scenario is that of steady solidification of a pure material at a constant pulling rate. The material used for modelling purposes was arbitrarily chosen as high purity titanium. Table 4.1 shows the thermophysical properties for this material and other input data necessary for modelling.

Table 4.1 Thermophysical properties for high purity titanium and other modelling input data.

Input	Units	Liquid	Solid
Thermal conductivity, k	[W/m·°C]	17	17
Density, ρ	[kg/m^3]	4110	4350
Specific heat capacity, c	[J/kg·°C]	925	925
Heat of fusion per unit mass, L_M	[J/kg]	2.95×10^5	
Speed of sound, v_{sound}	[m/s]	5090	
Melting temperature, T_m	[°C]	1670	
Hot heater temperature, T_H	[°C]	1700	
Cold heater temperature, T_C	[°C]	1300	
Hot zone heat transfer coefficient, h_H	[W/m^2·°C]	100	
Cold zone heat transfer coefficient, h_C	[W/m^2·°C]	600	
Sample radius, r	[mm]	5	
Adiabatic length, L_A	[mm]	40	
Pulling rate, u	[mm/s]	0.4	
Numerical time step, Δt	[s]	0.75×10^{-3}	
CV thickness (grid resolution), Δx	[mm]	0.8, 0.4, 0.2, 0.1	
Modelled domain length, ℓ	[mm]	200	

4.4 Modelling

In this section a mathematical model of the Bridgman furnace is set out. This is followed by details of an exact analytical solution for that model in the context of the test problem from Section 4.3.2. Finally, details of the BFFTM to be verified are given, and the theoretical order of accuracy of the model is calculated.

4.4.1 Mathematical model

Considering heat flow in the axial direction only, and referring to Fig. 4.2, the heat equation for a long cylindrical rod of uniform cross sectional area A, and perimeter p, moving at a pulling rate u along its axis, and transferring heat laterally to the surroundings with a heat transfer coefficient h, is given by equation (3.2). Noting that; $T_\infty = T_H$ and $h = h_H$ for $x > x_1$, and $T_\infty = T_C$

and $h = h_C$ for $x < -x_1$. This 1-dimensional model, with an additional term for peripheral heat loss, is deemed appropriate scenarios where the Biot number is less than 0.1.

4.4.2 Analytical solution

Naumann [27] demonstrates a 1-dimensional analytical model and solution for Bridgman furnace solidification. With reference to Fig. 4.2, Naumann's analytical solution is adapted here for the test problem given in Section 4.3.2. Assuming steady heat transfer (partial derivative terms with respect to time are set to zero), and using the transformation for dimensionless position, $X=x/r$, where r is the rod radius and x is the real axial position, the dimensionless steady-state form of equation (3.2) for equilibrium solidification can be written as;

$$\frac{\partial^2 T}{\partial X^2} - Pe\frac{\partial T}{\partial X} - 2Bi(T - T_{H,C}) = 0 \quad, \tag{4.5}$$

where $T_{H,C}$ refers to the temperature of the hot or cold heater regions (depending on axial position) and Pe is the thermal Péclet number, Bi is the Biot number—as given in equations (4.6) and (4.7), respectively—and assuming a characteristic length for the rod equal to its radius [128].

$$Pe = \frac{\rho c r u}{k} \tag{4.6}$$

$$Bi = \frac{h_{H,C}r}{k} \tag{4.7}$$

Note that; $h_{H,C}$ refers to the heat transfer coefficient in the hot or cold region of the furnace (depending on axial position). Assuming a pulling rate $u > 0$ the solution to (4.5) is given by equations (4.8), (4.9), (4.10) and (4.11), where $T_L(X)$ and $T_S(X)$ refer to temperature as a function of dimensionless position in the liquid and solid parts of the rod, respectively.

$$T_L(X) = T_H - D\exp[\beta*(X + X_1)] \qquad \forall \qquad -\infty < X \le X_1 \tag{4.8}$$

$$T_L(X) = A + B\exp(Pe_L X) \qquad \forall \qquad -X_1 \le X \le -X_0 \tag{4.9}$$

$$T_S(X) = A* + B*\exp(Pe_S X) \qquad \forall \qquad X_0 \le X \le X_1 \tag{4.10}$$

$$T_S(X) = T_C + C\exp[-\alpha*(X - X_1)] \qquad \forall \qquad X_1 \le X < \infty \tag{4.11}$$

The constants: α, $\alpha*$, β and $\beta*$ are calculated as follows:

$$\alpha* = \left(\sqrt{4\alpha^2 + Pe_S^2} - Pe_S\right)/2 \quad, \qquad \alpha = \sqrt{2Bi_C} \quad, \tag{4.12}$$

$$\beta* = \left(\sqrt{4\beta^2 + Pe_L^2} + Pe_L\right)/2 \quad, \qquad \beta = \sqrt{2Bi_H} \quad. \tag{4.13}$$

This solution is valid for a planar solid liquid interface located at a dimensionless position X_0 within the limits of the adiabatic zone $\pm X_1$ only. The thermal resistance of the crucible wall is

assumed to be negligible. Seven unknowns exist; A, A^*, B, B^*, C, D, and X_0. To solve for these unknowns, the following conditions are applied; T_L and dT_L/dX are continuous at $-X_1$, and similarly T_S and dT_S/dX are continuous at X_1. It is assumed that the temperature in the liquid is equal to the temperature of the solid at the solid liquid interface, and that solidification occurs in equilibrium at the melting temperature for the material, T_m. It is assumed that the latent heat generated at the liquid–solid interface is equal to the net conduction away from the interface in the solid and liquid phases, in other words, the Stefan condition is applied at the interface. Noting that the temperature gradient in the liquid and in the solid, at the interface, are both negative with respect to the coordinate system in Fig. 4.2, the following equation is applied:

$$q_{latent} = k_L \left.\frac{\partial T_L}{\partial X}\right|_{X_0} - k_S \left.\frac{\partial T_S}{\partial X}\right|_{X_0} \quad , \tag{4.14}$$

where q_{latent} is the rate of latent heat liberated at the interface per unit area;

$$q_{latent} = \rho_L u L_M \quad , \tag{4.15}$$

and L_M is the latent heat of fusion of the material per unit mass. Finally, the position of the interface, X_0, is found through an iterative procedure to solve the following transcendental equation;

$$\frac{k_L Pe_L (T_H - T_m) \exp(Pe_L X_0)}{\exp(-Pe_L X_1)\left(\dfrac{Pe_L}{\beta^*} - 1\right) + \exp(Pe_L X_0)} + q_{latent} = \frac{k_S Pe_S (T_m - T_C) \exp(Pe_S X_0)}{\exp(Pe_S X_1)\left(\dfrac{Pe_S}{\alpha^*} + 1\right) - \exp(Pe_S X_0)} \tag{4.16}$$

The remaining terms are calculated as follows:

$$A = T_H + B \exp(-Pe_L X_1)\left(\frac{Pe_L}{\beta^*} - 1\right) \tag{4.17}$$

$$A^* = T_C - B^* \exp(Pe_S X_1)\left(\frac{Pe_S}{\alpha^*} + 1\right) \tag{4.18}$$

$$B = -\frac{T_H - T_m}{\exp(-Pe_L X_1)\left(\dfrac{Pe_L}{\beta^*} - 1\right) + \exp(Pe_L X_0)} \tag{4.19}$$

$$B^* = -\frac{T_m - T_C}{\exp(Pe_S X_1)\left(\dfrac{Pe_S}{\alpha^*} + 1\right) - \exp(Pe_S X_0)} \tag{4.20}$$

$$C = -Pe_S B * \frac{\exp(Pe_S X_1)}{\alpha *} \tag{4.21}$$

$$D = -Pe_L B * \frac{\exp(-Pe_L X_1)}{\beta *} \tag{4.22}$$

The problem data in Table 4.1 is applied to this set of equations. A solution for the front position is computed using the `fzero` [143] command in Matlab® for solving nonlinear functions. The temperature profile in each section of the furnace is then determined.

4.4.3 Numerical solution

In this section, an outline is given of how the Bridgman furnace front tracking model (BFFTM) of Mooney et al. [126] is implemented to solve the test problem set out in Section 4.3.2. The theoretical order of accuracy of the model is determined. This is followed by details of the growth law used and the treatment of solid fraction in the solution.

Implementation of the BFFTM

The BFFTM has been demonstrated in a transient solidification problem involving a binary alloy where step changes in the pulling rate are applied [126]. It is shown how the model can be used to determine a steady-state temperature profile, given a fixed pulling rate, and assuming some arbitrary initial temperature profile in the sample. The model is applied in the same way to determine a steady-state solution to the test problem set out in Section 4.3.2. Firstly, the steady-state temperature profile for the test problem is found where the sample is stationary. A step change in pulling rate is then introduced and the evolution of the temperature profile is observed until a steady-state is reached. The final temperature profile is then used to compare with the results from the analytical model.

Note that, in the numerical solution, thermal resistance at the crucible wall is assumed negligible (as in the analytical solution). Also, Dirichlet boundary conditions are applied to the domain boundaries such that; $T=T_H$ at $x = -\ell/2$, and $T=T_C$ at $x = +\ell/2$. The value for ℓ was chosen suitably long enough so that the temperature profile approached T_H at the west domain boundary and T_C at the east domain boundary (as predicted by the analytical model).

Theoretical order of accuracy of the BFFTM

The control volume (CV) approach is used in the BFFTM. The sample is divided into disc-shaped CVs, Δx metres wide. The governing heat equation (3.2) is integrated over one CV to give the following [139];

$$\rho c \frac{\partial T}{\partial t} V_{CV} = \left\{ \left[k \frac{\partial T}{\partial x} \right]_e - \left[k \frac{\partial T}{\partial x} \right]_w \right\} A - \rho c u [T_e - T_w] A ...$$

$$... - \frac{h_{H,C} p}{A} (T - T_{H,C}) V_{CV} + \rho L_M \frac{\partial V_S}{\partial t} \tag{4.23}$$

where V_{CV} is the volume of the CV, the subscripts 'e' and 'w' refer to the east and west flat faces of the CV respectively, L_M is the latent heat generated per unit mass, V_S is the volume of solid material in a CV, and $\rho L_M \partial V_S / \partial t = E V_{CV}$. Dividing across by, $V_{CV} = A\Delta x$, and introducing Taylor series' expansions for the partial derivative terms (except for $\partial V_S / \partial t$), gives;

$$\rho c \left[\frac{\left(T_i^{m+1} - T_i^m \right)}{\Delta t} + O(\Delta t) \right] = k \left[\frac{T_{i-1} + 2T_i - T_{i+1}}{(\Delta x)^2} + O(\Delta x)^2 \right] - \rho c u \frac{(T_e - T_w)}{\Delta x} \dots$$
$$\dots - \frac{h_{H,C} \, p}{A} \left(T_i - T_{H,C} \right) + \frac{\rho L_M}{V_{CV}} \frac{\partial V_S}{\partial t} \qquad (4.24)$$

where the superscript 'm' is the temporal label, and the subscript 'i' is the spatial label for CVs lined up in the x-direction. Looking at the final term in this equation—that deals with the latent heat released during solidification—note that $V_S = g_S d$, where g_S is the fraction of solid within a CV and d is the captured volume in a CV, so then $\partial V_S / \partial t = g_S (\partial d / \partial t) + d (\partial g_S / \partial t)$ giving the following equation when Taylor series' replace the partial derivative terms:

$$\frac{\partial V_S}{\partial t} = g_S \left[\frac{\left(d_i^{m+1} - d_i^m \right)}{\Delta t} + O(\Delta t) \right] + d \left[\frac{\left(g_{Si}^{m+1} - g_{Si}^m \right)}{\Delta t} + O(\Delta t) \right] \quad . \qquad (4.25)$$

For more detailed accounts of the latent heat release mechanism used in the BFFTM see references [113] and [114]. {Refer to Appendix A.2 for detailed derivations of equations (4.23) and (4.24).}

Looking at the truncation terms—given by the "order of" notation, "O"—in equation (4.24), the lowest power of Δx is two, and in equation (4.25) the lowest power of Δt is one. This gives the theoretical order of accuracy for the discretised heat equation (used in the in the BFFTM) as first order in time and second order in space. However, it can be shown that the spatial accuracy of the BFFTM is in fact first order. This is due to the Neumann boundary condition imposed at the circumference of the sample used to estimate radial heat flow via the heat transfer coefficient, $h_{H,C}$. Removal of the truncation terms from (4.24) leaves the explicit finite difference scheme used in the BFFTM. Refer to [126] and [144] for a further description of the BFFTM algorithm.

Growth law for high purity titanium

The BFFTM, and its predecessors [113] and [114], are used to simulate dendritic columnar growth of alloys. However, the BFFTM can be adapted for growth of pure materials—where a planar non-dendritic interface occurs—by suitable adjustment of the growth law kinetics. The growth rate of the solid liquid interface, during the solidification of a pure material, is directly proportional to the level of kinetic undercooling at the interface [4] as follows:

$$v = \mu_K \Delta T_K \quad , \qquad (4.26)$$

where v is the interface growth rate, μ_K is the attachment kinetics coefficient, and ΔT_K is the kinetic undercooling at the interface which is equal to the difference between the material melting temperature and the temperature at the interface. Typically, for pure materials, the level of

undercooling is very small (less than 3 °C) unless solidification occurs at a very high speeds (100 m/s to 1000 m/s) [4]. The attachment kinetics coefficient is estimated using the collision limited growth model of Turnbull and Bagley [145];

$$\mu_K = \frac{v_{sound}L_{mol}}{\Re T_m^2} \quad , \tag{4.27}$$

where v_{sound} is the speed of sound, L_{mol} is the molar latent heat of fusion for the material, $\Re$ is the molar gas constant, and T_m is the material melting temperature (in units of Kelvin). The modelling data in Table 4.1 is used to calculate μ_K to have a value of 2.294 m/s·°C.

Fraction of solid

The volumetric fraction of solid, g_S, as a function of temperature for pure titanium, is estimated by an approximation to a step change of 0→1 near the melting temperature as follows:

$$g_S = \begin{cases} 0 & \forall & T \geq T_m \\ \dfrac{T_m - T}{\in} & \forall & T_m - \in < T < T_m \\ 1 & \forall & T \leq T_m - \in \end{cases} \quad , \tag{4.28}$$

where $\in$ is the thermal range over which phase change occurs, set to a very low value (0.01 °C in this case). This arrangement is equivalent to having a linear solid fraction to temperature relationship for an alloy with a solidification interval of 0.01 °C. This approach gives a result similar to the enthalpy linearisation method [121] where enthalpy is varied over a very small temperature range about the melting temperature.

4.5   Results

As per the description in Section 4.4.3 '*Implementation of the BFFTM*' above, the steady-state temperature profile for a fixed pulling rate was determined dynamically using the BFFTM. Firstly, the temperature profile for a stationary sample was estimated using the BFFTM, shown as $T_{initial}$ in Fig. 4.3. Then a step change in pulling rate was introduced and the evolution of the temperature profile was observed until a steady-state was reached, shown as T_{steady} in in Fig. 4.3.

This figure shows the temperature profile evolution over a 500 s period with the step change in pulling rate ($u=0\rightarrow0.4$ mm/s) introduced at $t > 0$. The time between subsequent temperature profiles shown in the figure is 10 s. The front marker for each curve is shown as an asterisk.

Simulations were carried out at four different grid resolutions, as per Table 4.1, starting at $\Delta x = 0.8$ mm and increasing the resolution by a factor of two until $\Delta x = 0.1$ mm. In each case the resulting steady-state temperature profile from the numerical model was compared to the analytical solution and the global numerical error was calculated. The observed order of accuracy was then calculated by comparing results over two consecutive grid refinements. Table 4.2 shows a summary of the results obtained.
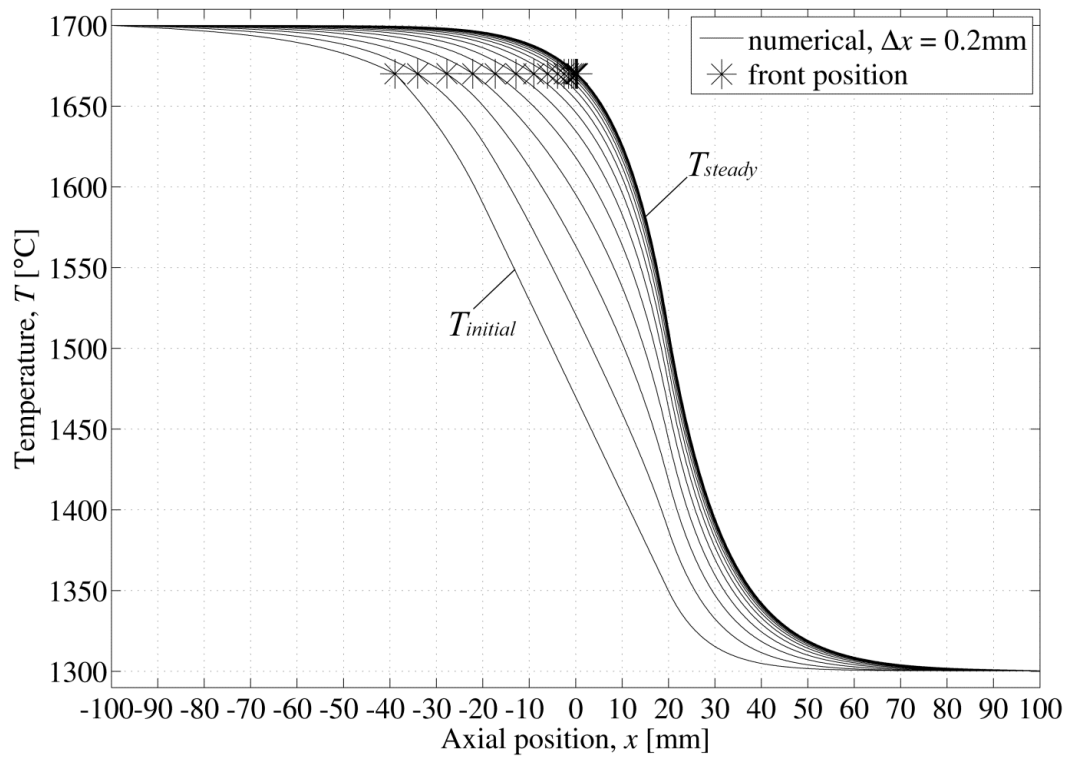
Fig. 4.3 Evolution of temperature profile resulting from step change in pulling rate.
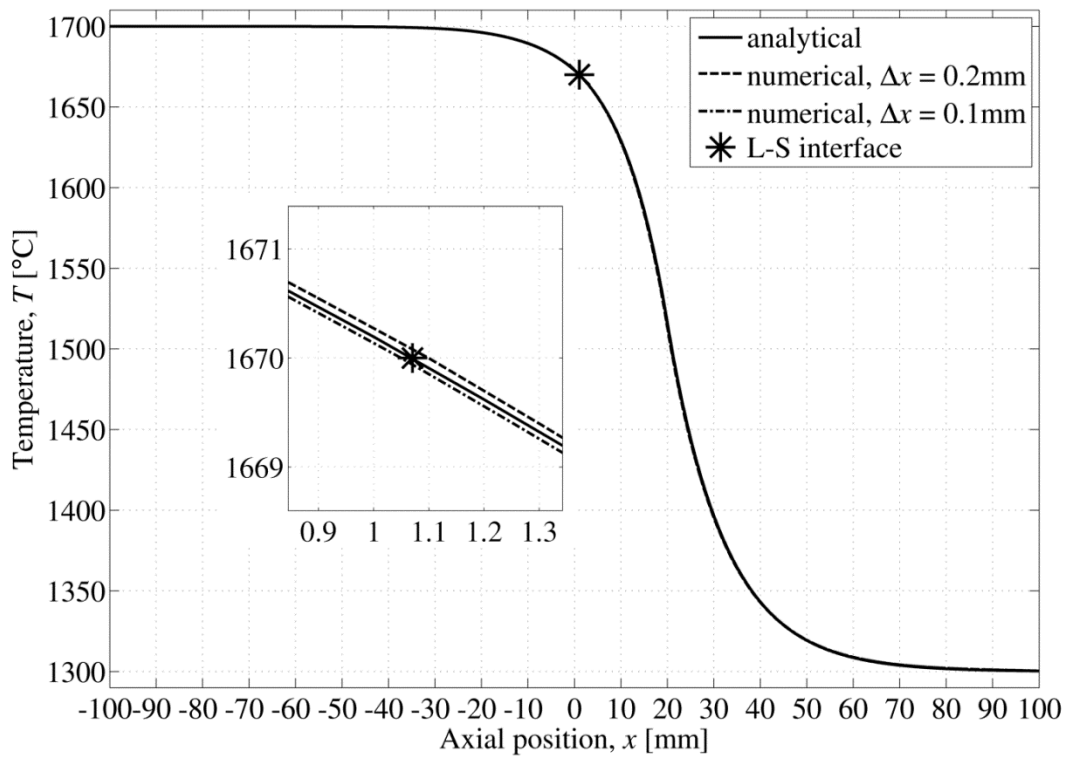
Fig. 4.4 Temperature profile for comparison of analytical and numerical solutions.

Table 4.2 Order verification simulation results

Simulation	Grid resolution, Δx [mm]	Global numerical error, NE^{global} [°C]	Observed order of accuracy, p_o
#1	0.8	2.11	
			0.61
#2	0.4	1.38	
			1.07
#3	0.2	0.66	
			0.98
#4	0.1	0.33	

Figure 4.4 shows the temperature profiles obtained from simulation #3 ($\Delta x = 0.2$ mm) and simulation #4 ($\Delta x = 0.1$ mm) along with the analytical solution. The liquid–solid interface location, as predicted this time by the analytical model, is shown by an asterisk.

4.6   Discussion

The discussion is limited to spatial order of accuracy verification since there is no transient analytical solution available to verify the temporal order of accuracy of the model.

Table 4.2 shows that the observed order of accuracy—obtained by comparing simulations at successively refined grid resolutions—converged to within two significant digits of the spatial order of accuracy for the BFFTM, i.e., it converged to one (first order). The model uses a numerically consistent finite difference scheme, since $p_o > 0$. Also, since the model is numerically stable, the scheme must be numerically convergent according to the Lax–Richtmyer theorem. The results reflect this inference since the numerical solution displayed asymptotic convergence with each grid refinement, i.e. the global numerical error was tending to zero as Δx was decreased. Also, the first term in the truncation error dominates the higher order terms, given that the value for p_o was shown to be converging [134]. The global numerical error converges by a factor of approximately two during successive grid refinements. This is to be expected given that the refinement ratio is 2 and that p_o was approximately equal to 1. If, for example, p_o was approximately equal to 2, i.e., second order accuracy, one would have expected the numerical error to decrease by approximately a factor of 4 since, $NE \propto (\Delta x)^{p_o}$.

The source of the error is most certainly due to the truncation of the derivative estimates in the discretisation scheme only. Round-off error is negligible, given that the code is implemented in double precision, thereby assigning 16 significant digits for storage of all numerically processed variables. Also the numerical scheme requires no iterative procedure so there is no potential for iterative convergence error in the numerical scheme. The analytical model is solved, however, using an iterative procedure—specifically equation (4.16) in Matlab®—but the error tolerance using this software is negligible at 2.22×10^{-16}.

The truncation error could be decreased by adding more terms to the Taylor series approximations of the partial derivative terms in the discretisation scheme. Alternatively, the existing Taylor series approximations could be improved using numerical techniques such as Heun's method or the midpoint method [140].

Figure 4.4 shows the analytical temperature profile compared with the numerically estimated temperature profiles for simulation #3 ($\Delta x = 0.2$ mm) and simulation #4 ($\Delta x = 0.1$ mm). It is clear that the numerical solution is tending towards the analytical solution as the grid resolution is refined. The maximum local error observed in simulation #3 was approximately 0.2% of the temperature range, and 0.1 % of the temperature range in simulation #4. This gives an accuracy of 0.8 °C at a grid resolution of 0.2 mm, and 0.4 °C at a grid resolution of 0.1 mm, over a 400 °C temperature range. The simulated front position is within 0.04 mm of the analytical prediction for simulation #3, i.e., 0.02% of the domain size, and 0.02 mm for simulation #4, i.e., 0.01% of the domain size.

It is noted that the analytical model assumes that equilibrium solidification occurs. In other words, the liquid–solid interface temperature is fixed at the equilibrium melting temperature during solidification. While, on the other hand, the BFFTM assumes that non-equilibrium solidification occurs. In the latter case, the front is at some temperature below the equilibrium melting temperature during solidification, i.e., it is assumed to be undercooled. Since the material solidifying is pure, this is a *kinetic* undercooling which is normally very small at low solidification velocities. For example in the test problem outlined, $u = 0.4$ mm/s giving an undercooling approximately equal to 2×10^{-4} °C. This accounts for minor differences between the predicted front location in the analytical and numerical model results. For example, given the temperature gradient at the solidification front (from the steady-state temperature profile) of 2739 °C/m, this equates to a difference of 7.3×10^{-4} mm between numerical and analytical front positions.

Finally, in the BFFTM model, it is necessary to model the phase change over a small but finite temperature range. This feature of the model is a numerical artefact whose effect on the results should be minimal. An exercise was carried out to investigate what effect increasing the range of temperature over which phase change occurs, $\in$, had on order accuracy.

Table 4.3 Effect of increasing the thermal range for phase change.

Thermal range, $\in$ [°C]	Observed order of accuracy, p_o
0.01	0.98
0.1	1.02
0.25	1.13
0.5	Non-convergent (negative p_o)

The observed order of accuracy, p_o, was calculated by comparing numerical results at a grid resolution of 0.2 mm and 0.1 mm and by increasing the thermal range, $\in$, from 0.01 °C to 0.5 °C.

Table 4.3 gives the results from this exercise where it can be seen that first order accuracy was lost above a thermal range of 0.1 °C. The order verification procedure is non-convergent when the thermal range is set to 0.5 °C. This exercise outlines the sensitivity of the method used to calculate p_o and also shows that a very small thermal range, i.e., less than 0.1 °C, is appropriate for the chosen test problem.

4.7   Conclusion

The BFFTM code of Mooney et al. [126] is verified for a simple steady scenario using the order verification method given by Knupp and Salari [134] by way of demonstrative example, specifically, steady solidification of high purity titanium. The verification method applied requires knowledge of a closed-form analytical solution (for comparison purposes with numerical results) to the governing partial differential equation of the process. This limited the choice of potential test problems to steady solidification of pure materials, since an analytical solution for transient solidification of an alloy system is not currently available in the literature.

The model is first order accurate in space. The source of numerical error is primarily truncation error. The order of accuracy of the model could be increased by using a higher order interpolation in the discretisation scheme of the model.

For the test problem investigated, asymptotic convergence of the global numerical error is observed for grid resolutions of 0.8 mm or less, and the grid resolution necessary for a maximum local numerical error of < 1 °C is 0.2 mm. A value of 0.01 °C is deemed appropriate for the thermal range over which phase change occurs in the numerical model.

This chapter satisfies Objective 2 of this thesis, as given in Section 1.2. An order verification exercise has been carried out for steady solidification of a pure material. Now that the numerical model has been developed and verified (albeit for a limited case), it is appropriate to apply the model to a real Bridgman furnace.

Chapter 5

Characterisation of a Bridgman Furnace

This chapter details how the BFFTM is applied in series with a numerically implemented proportional integral derivative (PID) controller for the purposes of determining the heat transfer coefficients of a real Bridgman furnace apparatus. A combined experimental-numerical approach is adopted. Experimental data, *viz.* thermocouple measurements at various axial positions in the sample and for different furnace temperatures from static Bridgman experiments using a hypoperitectic multicomponent alloy (alloy 455, see Section 2.5.2), is fed into the model and controller. An inverse heat transfer problem is solved that consequently characterises the furnace. This characterisation exercise was performed so that the resulting heat transfer coefficients could be used (as input data) in other key experiments using the same furnace. The model solves for the heat flux at the circumference of the sample as a function of axial position. This allows for the heat transfer coefficient at the circumference of the crucible to be estimated. The method outlined is useful as it may be applied to other Bridgman furnaces.

Referring to Section 1.2, this chapter addresses the third objective of this thesis. Reference [144] is the main source of content for this chapter. It is noted that the experiments detailed in this chapter were carried out by others, i.e., co-authors Lapin and Gabalcová of reference [144]. The following objectives were identified as part of this chapter:

(a) To estimate the heat flux at the ends of the cylindrical sample;
(b) To estimate the heat transfer coefficient at the ends of the cylindrical sample;
(c) To estimate the heat flux at the circumference of the sample as a function of axial position;
(d) To estimate the heat transfer coefficient at the circumference of the crucible as a function of axial position.

5.1 Bridgman Furnace Heat Transfer Coefficients

Determining the heat transfer coefficients in a Bridgman furnace using traditional techniques can be time consuming and difficult to do accurately. The calculation depends on furnace and sample geometry, the sample properties, the crucible properties, and the atmospheric conditions

inside the furnace. It is necessary for experimentalists to know the heat transfer coefficient of their furnace so that they can accurately estimate the true temperature gradient and temperature profile in a test sample.

An experimental procedure is outlined by Banan et al. [146] where an average heat transfer coefficient between a sample and the surrounding furnace is estimated using a lumped capacity cooling model. An isothermal sample is suddenly moved to a hotter part of the furnace and the thermal history recorded.

An experimental study by Rosch et al. [147] combines radiation and convection heat fluxes to estimate an overall heat transfer coefficient in a Bridgman furnace. The radiation heat flux is linearised with respect to temperature difference through the following relation:

$$T_{furnace}^4 - T_{muffle}^4 \approx 4T_{av}^3\left(T_{furnace} - T_{muffle}\right) \quad , \tag{5.1}$$

where $T_{furnace}$ is the furnace temperature, T_{muffle} is the surface temperature of the muffle tube containing the ampoule, and T_{av} is their average. This approximation produces an error of less than 2 percent provided that $T_{furnace}/T_{muffle}$ and $T_{muffle}/T_{furnace}$ is less than 4/3. Ultimately, Rosch et al. merge the $4(T_{av})^3$ into the overall combined heat transfer coefficient. Rosch et al. subject the sample to additional heating—within the operating furnace—using an electrical heating coil wrapped around the crucible (i.e., the muffle); thus, creating a known temperature difference between the sample and furnace heater. The work has been extended [148] to estimate convection coefficients in different gas environments, and emissivities for different coil sleeve materials. Neither of these studies treat the heat transfer coefficient as a function of axial position, that is, fixed values are used for the heat transfer coefficient in the hot and cold zones. However, both studies conclude that the overall heat transfer coefficient is non-linear (i.e., a function of temperature cubed) at higher temperatures due to dominant radiation heat transfer.

A numerical study by Bartholomew and Hellawell [149] looks at changes in growth rate and temperature gradient where the radiation heat transfer incorporates a view factor to account for a typical furnace geometry. Separate values for liquid and solid thermal conductivity are used.

Several analytical studies [26][150][151], concerned with interface shape and interface velocity during growth of crystalline materials, use a fixed value for heat transfer coefficient to specify their boundary conditions. However, it is noted that the heat transfer coefficient should increase at high temperatures due to increased radiative effects.

5.2 Methodology

5.2.1 Experimental method

The experiment apparatus

The experiments were carried out using a vertical Bridgman furnace, as shown schematically in Fig. 5.1. The furnace, fully described elsewhere [152], consisted of a cold formed smooth molybdenum resistance heating element in the hot zone. The cylindrical heating element had a

length of 300 mm and inside diameter of 33 mm. The space between the hot and cold zones was 7 mm, made up by a 5-mm thick annular aluminium oxide baffle and a 2 mm gap on the hot side. The cold zone heat sink consisted of a cylindrical water-cooled 'crystalliser' with inside diameter of 16 mm.
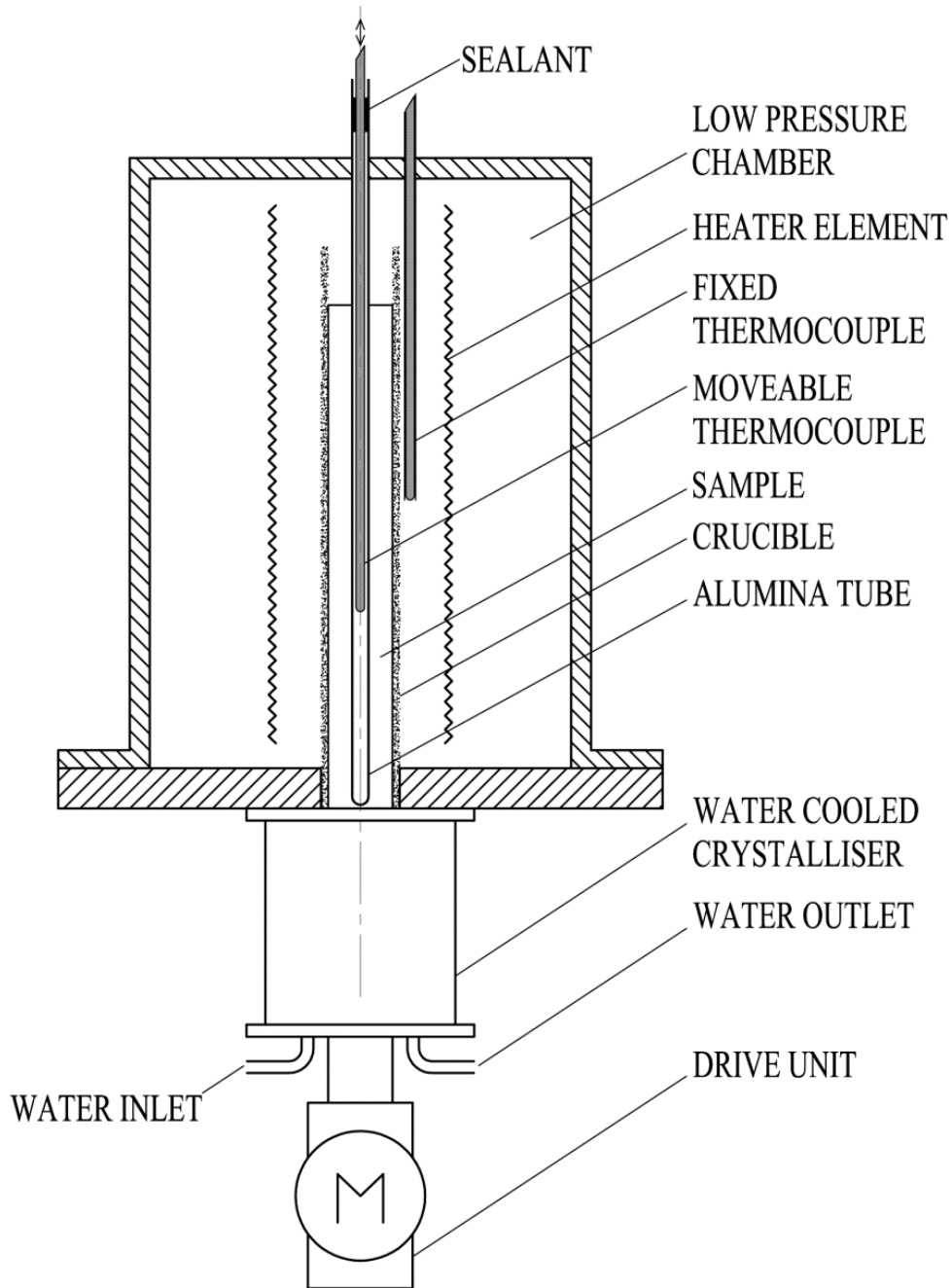
Fig. 5.1 Schematic of the Bridgman furnace apparatus.

The sample was a 170-mm long rod of titanium aluminide, with a diameter of 10 mm. The sample was contained in a high purity yttrium oxide (Y_2O_3), crucible with outside diameter of 15 mm, and a wall thickness of 2.5 mm. A moveable thermocouple was located in the longitudinal axis of the sample, contained in a protective closed-end alumina tube, with inside and outside diameters of 3 mm and 5 mm, respectively. The tube was plasma sprayed with a layer of yttrium oxide to minimise reaction between the tube and the melt. The thermocouple was free to traverse in

the axial direction of the crucible. The alumina tube was fixed and contained air at standard atmospheric pressure. The open end of the tube was closed with a sealant.

A fixed thermocouple was contained in a protective ceramic tube and positioned at a fixed distance from the crucible wall. The reading from this thermocouple was used to control the heater temperature by comparing directly with the heater temperature set-point. The furnace was enclosed in a low pressure chamber so that solidification could occur in a contaminant free and rarefied atmosphere.

The experimental procedure

The furnace chamber was evacuated to an absolute pressure of 3 Pa and flushed with Argon (99.9995% purity) six times, before being backfilled with argon to an absolute pressure of 10 kPa. The hot region heater was set so that the fixed thermocouple read 1680 °C, to partially melt the sample, for a period of 1200 s. The crucible and sample were drawn 20 mm into the cold region of the furnace where they were allowed to achieve a steady-state temperature profile for a period of 300 s. The moveable thermocouple was located at an initial axial position of 2 mm from the zero datum position at the bottom of the sample (in the cold zone). The thermocouple was moved upwards along the sample axis, at 0.25 mm increments, stopping to measure the axial temperature. The final temperature measurement was taken at an axial position of 160 mm from the zero datum position.

This procedure was repeated for three other heater settings corresponding to a fixed thermocouple reading of 1650 °C, 1630 °C and 1600 °C. The water-cooled crystalliser had a constant output water temperature of 17 °C during all experiments.

5.2.2 Mathematical model and the numerical implementation

The BFFTM model—as described in Section 3.2—is applied to the experimental data. Some modifications are required to deal with the more complicated multi-component titanium aluminide alloy, specifically with respect to the calculation of volumetric solid fraction, g_S. This is dealt with later, in detail, in Section 5.3.4. In addition, the calculation of the radial heat flux q_2 requires attention to account for the physical aspects of the experimental apparatus. It is noted that in the experimental procedure the sample is stationary, i.e., $u = 0$, so the advection term in equation (3.2) is zero. The following describes in detail how the BFFTM is applied to the experimental apparatus in order to characterise it.

Application of the mathematical model to the experiment apparatus

Figure 5.2 shows a schematic section of the experimental Bridgman furnace apparatus in Fig. 5.1. The schematic shows the cold (a) and hot (b) regions of the furnace separately. The alumina tube assembly that contains the moveable thermocouple is not considered in this analysis. It is assumed that the effect of the presence of the alumina tube assembly is negligible at very high temperatures,

70

so that the temperature at the centre of the sample is equal to the temperature measured by the movable thermocouple.
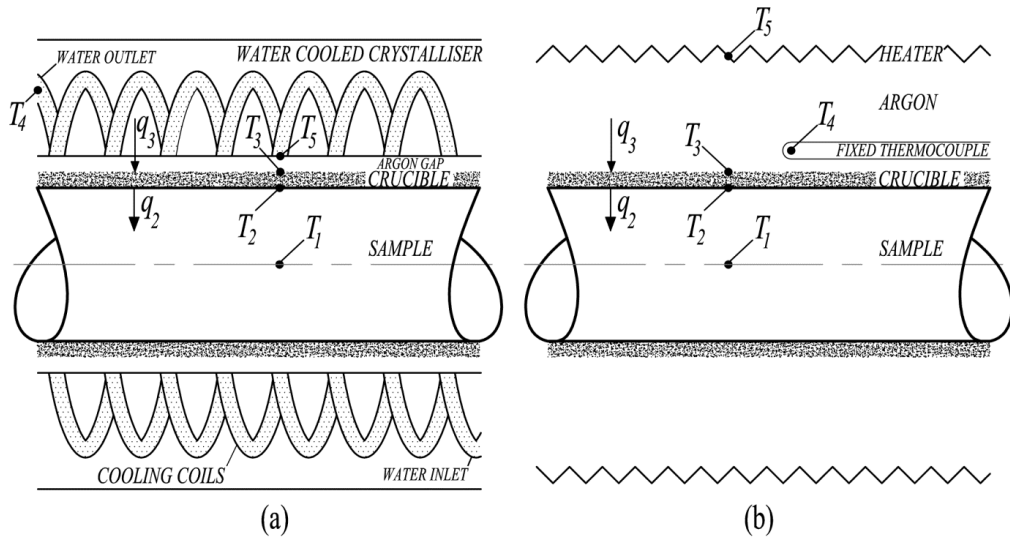
Fig. 5.2 Schematic of the cold (a) and hot (b) regions of the Bridgman furnace apparatus.

The temperature throughout the sample is assumed to vary in the axial direction only; that is, the temperature at the centre of the sample T_1 is assumed to be equal to the temperature of the sample at the sample–crucible boundary, T_2. This is a reasonable assumption for processes with a Biot number less than 0.1.

The sample experiences a heat flux q_2 at the sample–crucible boundary (i.e., at the sample circumference) in the hot and cold regions of the furnace. The crucible wall is treated as a thermal resistance between the sample surface and the outside surface of the crucible such that $T_2 \neq T_3$. In the hot region of the furnace T_3 is greater than T_2, and vice-versa in the cold region. It is assumed that heat transfer in the crucible occurs by conduction in the radial direction only, and that the contact resistance between the sample and the crucible inner wall is negligible. Then, by conservation of radial heat flow and assuming no axial heat flow in the crucible, the radial heat flux at the outside of the crucible q_3, is related to the radial heat flux at the sample–crucible boundary, q_2, such that,

$$q_3 r_3 = q_2 r_2 \quad , \tag{5.2}$$

where r_2 is the radius of the sample and r_3 is the outside radius of the crucible.

The temperature at the crucible wall, T_3, is a function of the ratio of the outer to inner radii of the crucible (r_3/r_2), the thermal conductivity of the crucible material (k_{cru}) and the radial heat flux (q_2) [153], and is given by;

$$T_3 = T_2 + q_2 r_2 \frac{1}{k_{cru}} \ln\left(\frac{r_3}{r_2}\right) \quad . \tag{5.3}$$

Note that, equations (5.2) and (5.3) are used together to replace equation (3.8) in the BFFTM numerical scheme, when characterising the furnace, to account for the crucible which was previously ignored. See Appendix A.4 for the derivation of equations (5.2) and (5.3).

71

The heat transfer coefficients

Figure 5.2(a) shows the cold region of the furnace—the crystalliser component—where the water temperature at the outlet of the crystalliser is T_4. The heat transfer coefficient at the circumference of the crucible, as a function of axial position in the crystalliser, is then given by;

$$h_3 = q_3 \frac{1}{T_4 - T_3} = q_2 \left(\frac{r_2}{r_3} \right) \frac{1}{T_4 - T_3} \quad . \tag{5.4}$$

Since the furnace is rarefied to approximately one-tenth of atmospheric pressure during experiments, it is assumed that only radiative heat transfer occurs in the hot region of the furnace between the crucible and the heater surface. Referring to Fig. 5.2(b), the radiation heat transfer coefficient at the crucible circumference is given by the net radial heat flux q_3, divided by the temperature difference between the surfaces exchanging thermal radiation, T_5-T_3 [154]. However, the heater temperature T_5 is unknown in this case. Instead, the known temperature T_4 (as measured by the fixed thermocouple) is used to define a heat transfer coefficient at the crucible wall h_3 for the hot zone, according to equation (5.4).

Similarly, the heat transfer coefficient for heat transferred through the end faces of the sample, h_x, is given by;

$$h_x = q_x \frac{1}{T_4 - T_x} \quad , \tag{5.5}$$

where q_x and T_x are the net axial heat flux and the temperature, respectively, at the sample ends, i.e., at $x=0$ and $x=\ell$ (see Fig. 5.3 below).

Model domain

A simple 1-dimensional numerical domain is applied to the *sample only*, within the experimental setup, as illustrated in Fig. 5.3. Note the orientation change in this figure when referring back to Fig. 5.1, the x-direction relates to the vertical axis of the sample in the furnace. The numerical domain is in the range $0<x<\ell$. The cold region is given by $0<x<x_1$, the baffle region is given by $x_1<x<x_2$ and the hot region given by $x_2<x<\ell$. The domain is divided into disc-shaped volumes of thickness Δx. The mush–liquid interface (front) is shown in the domain given by a front marker (×).
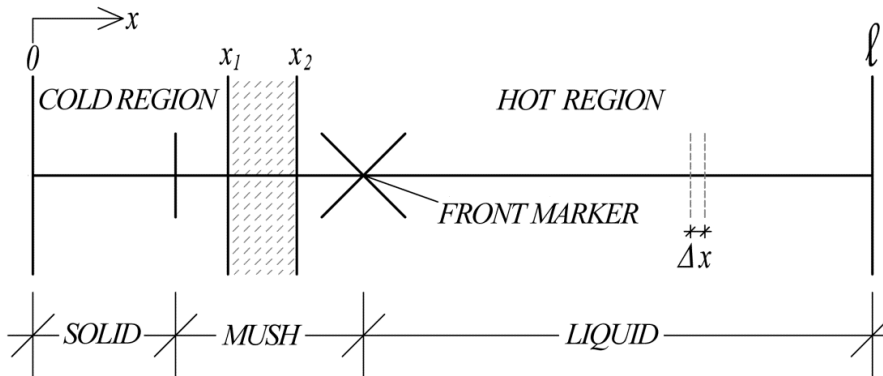
Fig. 5.3 A 1-dimensional numerical domain applied to the sample in the experimental set up.

Boundary conditions

A Neumann boundary condition is applied at both ends of the numerical domain. The temperature profile from each experiment is extrapolated using the shape preserving `pchip` (Piecewise Cubic Hermite Interpolating Polynomial) command in Matlab® [155] to estimate the temperature gradient at $x=0$ and at $x=\ell$. This permits a simple calculation for the diffusion heat flux (in the axial direction only) by application of Fourier's law at both ends of the domain, such that;

$$
flux = \begin{cases} q_{i-1} & = -k\dfrac{dT}{dx}\bigg|_{x=0} & \forall & x=0 \\[2ex] q_{i+1} & = -k\dfrac{dT}{dx}\bigg|_{x=\ell} & \forall & x=\ell \end{cases} .
\tag{5.6}
$$

PID method for solving the inverse heat transfer problem

An inverse heat transfer problem is one where a thermal *effect* is known and the *cause* is discovered [156]. In this case, the temperature at the centre of the sample (the effect) is known and the heat flux at the surface of the sample (the cause) is unknown. Various procedures involving iterative matrix calculations exist [157][158] to solve the inverse heat transfer problem for relatively simple heat equations. However, computational effort is substantially increased for non-linear problems [159] like the one presented here.

An alternative, non-traditional method for solving the inverse heat transfer problem is to manipulate the heat flux q_2 in a controlled manner, based on the error between the experimentally measured temperature and the same temperature as simulated by a numerical procedure. This method is implemented in a similar manner by McFadden et al. [56] to estimate heat flux at a heat sink during a directional solidification experiment using a proportional integral derivative (PID) control algorithm.

Figure 5.4 shows a control system block diagram with negative feedback, applied on a per CV basis, where 'PID' refers to a discrete PID controller process and 'BFFTM' is the process that solves equation (3.4) for T_i^{m+1}. Given some starting value for the heat flux at the surface of the sample q_2, the BFFTM can simulate the corresponding CV temperature $T_{1(sim)}$.
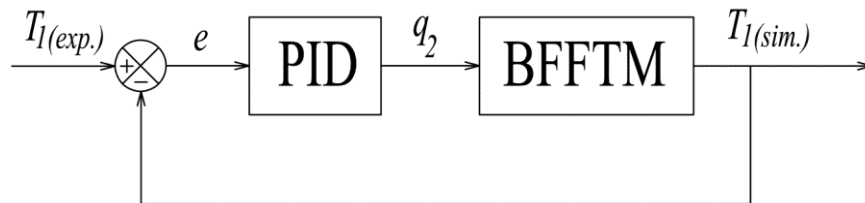
Fig. 5.4 Control system block diagram with negative feedback loop to control CV temperature.

This temperature is fed back and compared with the experimental temperature measurement $T_{I(exp)}$ and an error signal is generated. The PID controller uses the error signal to continuously and dynamically manipulate the value of q_2 so that the error value is minimised and a steady-state temperature output is reached. At this point the simulated temperature is equal to the experimental sample temperature. This process is carried out at each CV independently.

An ideal PID controller with filtered derivative is used to implement the discrete PID controller process. The control equation—written in the Laplace domain—is given by [160],

$$q_2(s) = e(s)K_c \left(1 + \frac{1}{\tau_I s} + \frac{\tau_D s}{\frac{\tau_D}{N} s + 1} \right) \quad , \tag{5.7}$$

and is illustrated in Fig. 5.5, where K_c is the controller gain, τ_I is the integral time constant, τ_D is the derivative time constant. The controller includes an adjustment variable N for the break frequency of the low pass filter in the derivative term.
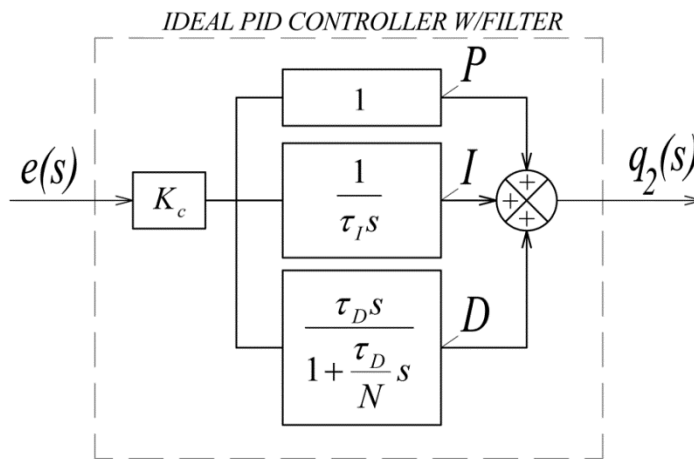
Fig. 5.5 Ideal PID controller with derivative filter.

Taking the proportional (*P*), integral (*I*) and filtered derivative (*D*) signals individually, each signal can be rewritten in the continuous time domain as follows:

$$P = K_c e(t) \quad , \tag{5.8}$$

$$I = \frac{K_c}{\tau_I} \int e(t)dt \quad , \tag{5.9}$$

$$D = K_c \tau_D \left(\frac{de}{dt} \right) - \frac{\tau_D}{N} \left(\frac{dD}{dt} \right) \quad . \tag{5.10}$$

These equations are discretised—for implementation in series with the BFFTM algorithm—using a forward difference approximation in the derivative signal and the trapezoidal rule in the integral signal, yielding,

74

$$P^{m+1} = K_c e^{m+1} \quad , \tag{5.11}$$

$$I^{m+1} = I^m + \frac{K_c}{\tau_I} \Delta t \left(\frac{e^{m+1} + e^m}{2} \right) \quad , \tag{5.12}$$

$$D^{m+1} = \left(1 - \frac{N}{\tau_D} \Delta t \right) D^m + K_c N \left(e^{m+1} - e^m \right) \quad . \tag{5.13}$$

Determining the heat transfer coefficient at the crucible circumference

The temperature output from the BFFTM, $T_{1(sim)}$, and the steady-state value of the controller manipulated variable q_2, is used to calculate the temperature at the exposed side of the crucible T_3 using equation (5.3), given that $T_2 \approx T_1$. This allows for the heat transfer coefficient h_3 to be calculated via equation (5.4), as illustrated in the block diagram in Fig. 5.6.
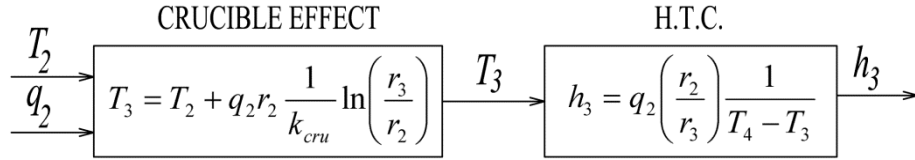
Fig. 5.6 Block diagram for the calculation of the heat transfer coefficient, h_3.

5.3   Simulation Input Parameters

5.3.1 Geometrical properties

The geometrical properties used in the numerical procedure are given in Table 5.1.

Table 5.1 Geometrical properties used in all simulations.

Property	Value
Sample length, ℓ [mm]	170
Baffle zone start, x_1 [mm]	20
Baffle zone end, x_2 [mm]	27
Sample radius, r_2 [mm]	5
Crucible outer radius, r_3 [mm]	7.5

The geometric location of the baffle zone is trivial in the simulations that follow where the PID controller is active. This is because the PID controller determines the sign of the radial heat flux at the sample circumference (q_2), i.e., negative for heat flowing away from the sample and positive for heat flowing into the sample along its entire length (even in the baffle region). The model is implemented so that only an adiabatic point exists (in effect, $x_1=x_2$) at the position of zero heat flux, as predicted by the PID controller.

5.3.2 Numerical parameters

The numerical parameters used in all simulations are given in Table 5.2. The numerical time step Δt, and control volume thickness Δx, are selected so that the explicit finite difference scheme is stable. Convergence of the model was tested by carrying out trial simulations with the inverse heat transfer controller switched off. The trials demonstrated a suitably convergent result using these numerical parameters.

Table 5.2 Numerical parameters used in all simulations.

Property	Value
Control volume thickness, Δx [mm]	0.2
Time step, Δt [s]	7.5×10^{-4}
Number of control volumes	850

5.3.3 Controller parameters

The discrete PID controller is tuned using the Ziegler Nichols ultimate cycle method [161]. Table 5.3 shows the resulting values for controller gain K_c, integral time τ_I, and derivative time τ_D used in all simulations.

Table 5.3 Ideal PID controller settings for all simulations.

Controller setting	Value
Controller gain, K_c	2
Integral time, τ_I [s]	8
Derivative time, τ_D [s]	0.12
Filter variable , N	10

5.3.4 Material properties

Thermophysical properties

The density, specific heat capacity and thermal conductivity of the alloy are estimated by first, second and third order polynomial functions of temperature using equation (2.30), where the polynomial coefficients are taken from a study by Egry et al. [162] for the ternary titanium aluminide alloy, Ti–45.5Al–8Nb (all at.%). This alloy is constitutionally very similar to alloy 455 used in the experiments described here.

Table 5.4 shows the polynomial coefficients used to calculate these properties, where α is the thermal diffusivity ($k/\rho c$) and the latent heat of fusion per unit mass is, $L_M = 3.4 \times 10^5$ J/kg. The

thermal conductivity of the yttrium oxide crucible is estimated by a second order polynomial function of temperature fitted to data from Touloukian [163], the coefficients of which are shown in the final column of Table 5.4.

For a given CV, the algorithm calculates the variable property value based on the temperature of that CV at the previous time step. According to Özışık [139] this method of lagging properties by one time step is appropriate for non-linear problems.

Table 5.4 Polynomial coefficients used to estimate thermophysical properties of the sample alloy and crucible, adapted from Egry [162] and Touloukian [163].

	Sample Alloy				Crucible
	Specific heat capacity, c [J/kg·°C]		Density, ρ [kg/m^3]		Thermal diffusivity, α [m^2/s]	Thermal conductivity, k_{cru} [W/m·°C]
	(liquid)	(solid)	(liquid)	(solid)	(liquid or solid)	(solid)
a_0	1040	632.4	4215	3133	5.36×10^{-6}	21.31
a_1	0	7.4×10^{-2}	−0.295	−0.457	5.18×10^{-9}	−0.020855
a_2	0	-2.1×10^{-4}	0	0	4.3×10^{-13}	5.83×10^{-6}
a_3	0	2.9×10^{-7}	0	0	-3.01×10^{-15}	0

Dendrite kinetics

The growth rate, v_{tip}, of the front marker ($\times$) during solidification, is calculated in the BFFTM using a suitable dendritic growth law taken from a study by Rebow et al. [164] as;

$$v_{tip} = 2.63 \times 10^{-6} \Delta T_{tip}^{2.79} \quad , \tag{5.14}$$

where ΔT_{tip} is the undercooling at the front, i.e., the difference between the temperature at the front marker and the equilibrium liquidus temperature for the alloy. The alloy, upon which this growth law is based, is constitutionally similar (Ti–46at.%Al) to alloy 455.

Solid fraction estimation

In the BFFTM model, the volumetric fraction of solid g_S must be known as a function of temperature. Solid regions have a solid fraction of unity; liquid regions have a solid fraction of zero; while mushy regions have some value in between unity and zero, depending on the temperature and the composition. The Scheil relation, equation (2.22), is suitable for binary alloys. Another approach is required in order to be able to calculate equations (3.9) and (3.10) when modelling a multicomponent titanium aluminide alloy. The CALPHAD (CALculation of PHAse Diagrams) method uses validated thermodynamic databases for each of the alloy elements to estimate the Gibbs free energy, and hence the phase diagram for that alloy [4]. Thermocalc® [165] used the CALPHAD method to determine a function for solid fraction in terms of temperature for

the multicomponent alloy. Figure 5.7 shows the resulting solid fraction to temperature relationship for alloy 455. The equilibrium solidus temperature $T_s = 1434$ °C and the equilibrium liquidus temperature $T_l = 1550$ °C are taken from this data set as the temperatures corresponding to a solid fraction of unity and zero respectively. The data is generated using the 'Modified Scheil Module' based on the approach of Chen and Sundman [166]. The model assumes Scheil type solidification [33], that is, no diffusion in the solid; however, equilibrium back diffusion of the interstitial alloy elements (boron and carbon) is permitted.
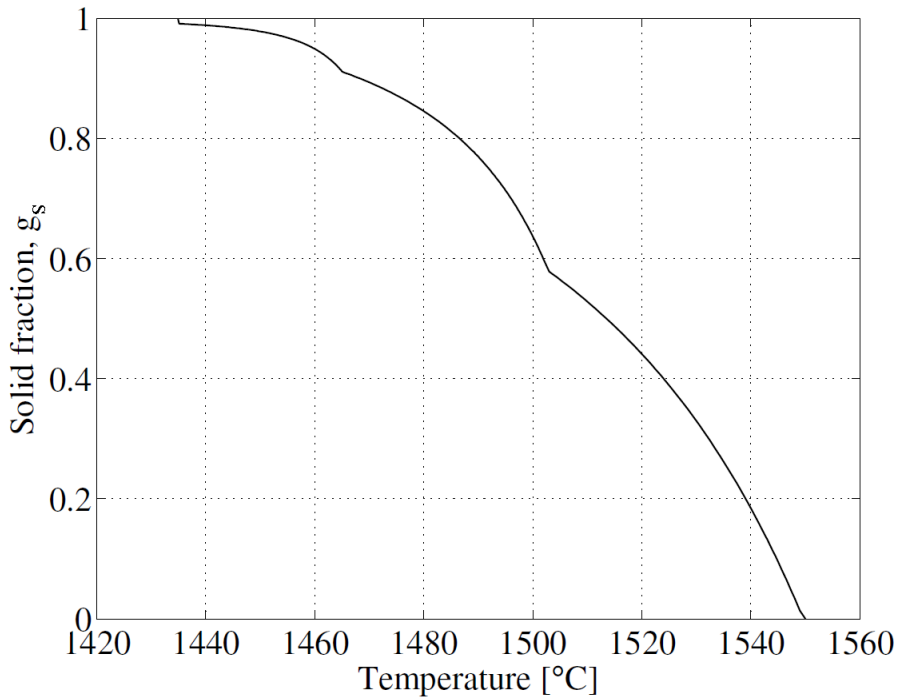
Fig. 5.7 Solid fraction to temperature relationship for alloy 455 as estimated using Thermocalc® [165] via the 'Modified Scheil Module'.

5.4   Results

In this section the results are categorised into experimental and numerical results. Reference numbers for each of the experiments, E.1–E.4, and their respective hot and cold region temperatures, are given in Table 5.5. Note that in the cold region of the furnace, T_4 refers to the steady-state water outlet temperature at the crystalliser, while in the hot region of the furnace, T_4 refers to the steady-state temperature measurement at the heater's thermocouple.

Table 5.5 Experiment reference numbers with hot and cold region reference temperatures.

	Experiment Number			
	E.1	E.2	E.3	E.4
COLD REGION, T_4 [°C]	17	17	17	17
HOT REGION, T_4 [°C]	1680	1650	1630	1600

5.4.1 Experimental results

Figure 5.8 shows the axial temperature profiles that were measured for each of the experiments referenced in Table 5.5.
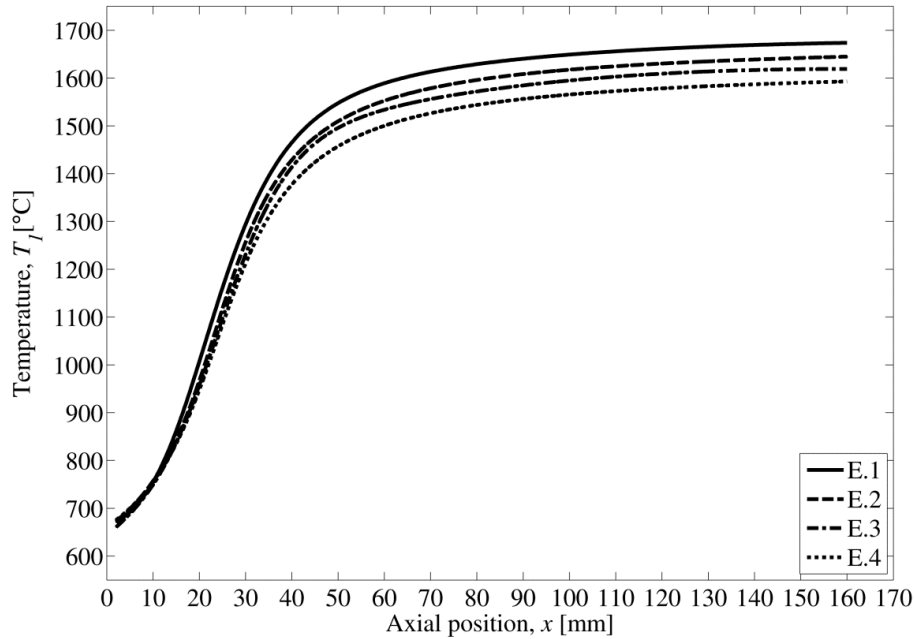
Fig. 5.8 Experiment temperature profiles at various heater settings.

5.4.2 Numerically processed results

Heat flux and heat transfer coefficients at the domain boundaries

Table 5.6 shows the estimated values for the heat flux q_x, from equation (5.6), and heat transfer coefficient h_x, from equation (5.5), at the domain boundaries. The temperature at the boundaries, T_x, is also shown (as extrapolated from the experimental data).

Table 5.6 Heat flux, heat transfer coefficients, and extrapolated temperature at the domain boundaries.

Experiment No.	$x=0$ (COLD END)			$x=\ell$ (HOT END)		
	q_x [kW/m^2]	h_x [W/m^2·°C]	T_x [°C]	q_x [kW/m^2]	h_x [W/m^2·°C]	T_x [°C]
E.1	−96	146	670.51	0.34	68	1675.00
E.2	−104	161	661.92	0.87	292	1647.03
E.3	−120	188	653.86	0.21	20	1619.09
E.4	−101	154	671.44	2.18	471	1595.37

Heat flux at the circumference of the sample

Figure 5.9 shows the heat flux at the circumference of the sample q_2—as simulated by the PID controller for each experiment—plotted as a function of axial position (grey plots). The average heat flux for all the experiments is also shown (black plot).
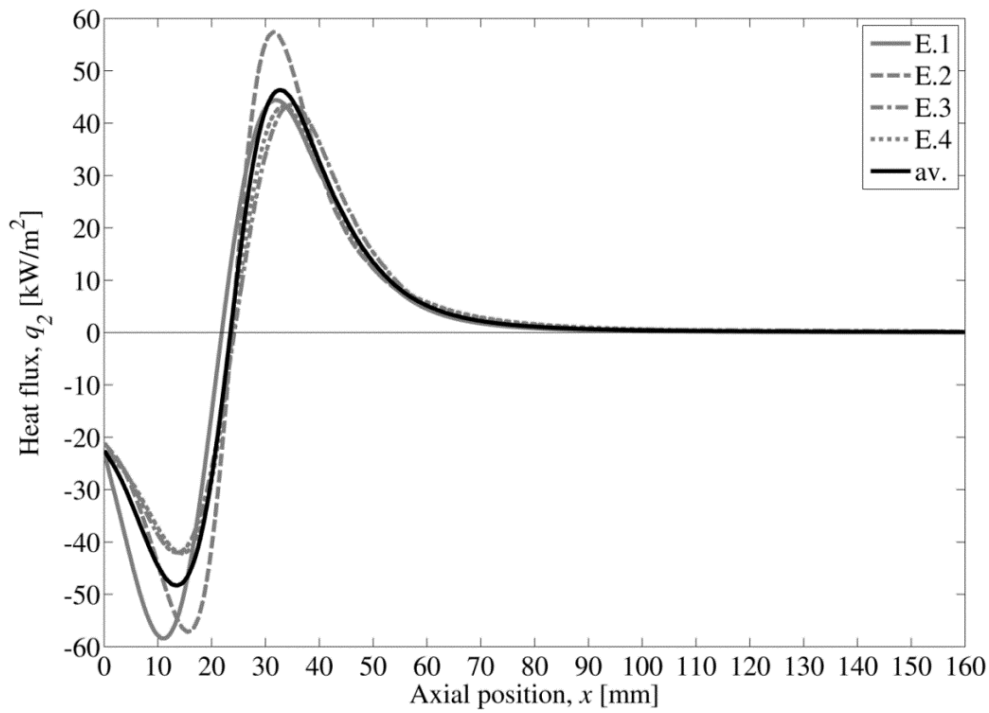
Fig. 5.9 Heat flux at the sample circumference versus axial position.

Heat transfer coefficient at the circumference of the crucible

Figure 5.10 shows the resulting heat transfer coefficient h_3 as a function of axial position for each experiment (grey plots). The average heat transfer coefficient as a function of axial position is also shown (black plot).
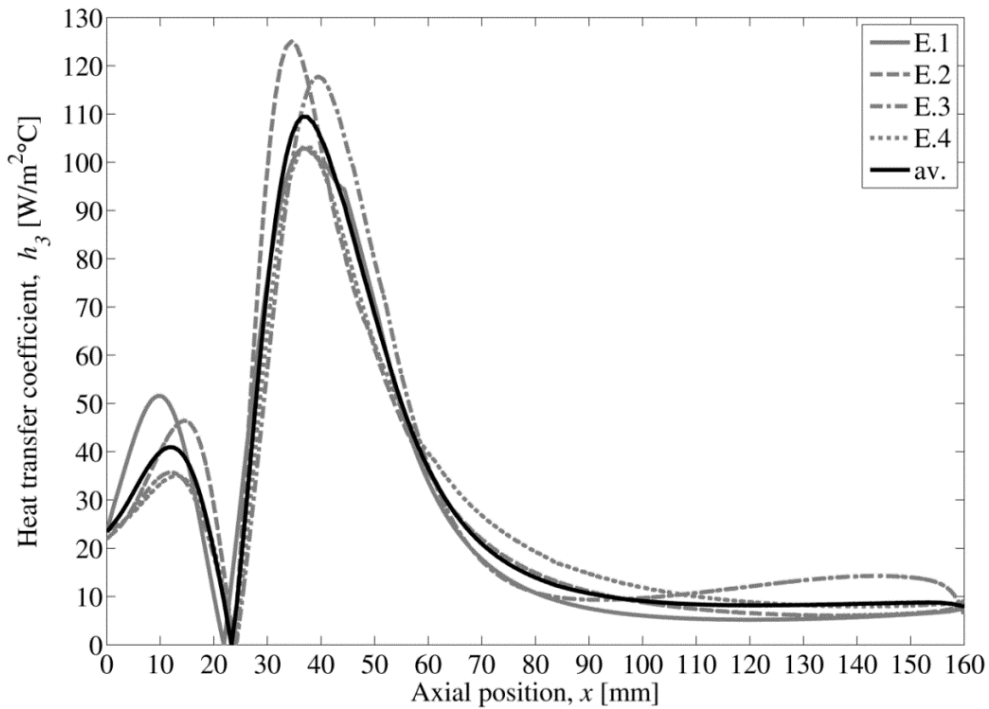
Fig. 5.10 Heat transfer coefficient at the crucible circumference versus axial position.

5.5 Discussion

5.5.1 Discussion of results

Experimental results

Figure 5.8 shows the measured temperature profile for each experiment, where the only difference between the experimental trials is that the furnace set point temperature was changed in accordance with Table 5.5. Experimental trial E.1 had the highest heater setting (1680 °C) and E.4 had the lowest heater setting (1600 °C). As the heater setting was decreased the temperature profile in the hot region decreased proportionally. However, in the cold region the temperature profiles were convergent to each other. This was to be expected given that the outflow temperature from the water-cooled crystalliser was held constant during experiments.

Heat flux and heat transfer coefficients at the domain boundaries

Table 5.6 shows that the heat flux at the cold end of the domain ($x = 0$) was much larger than that observed at the hot end ($x = \ell$). This was to be expected as the temperature gradient was much higher at the cold end of the sample than at the hot end. The estimated heat transfer coefficients at the cold end of the sample were of similar magnitude in each experiment simulation, i.e., in the range 146 W/m^2·°C to 188 W/m^2·°C.

Heat flux in the axial direction at the hot end of the sample range from 0.21 kW/m^2 to 2.18 kW/m^2. These heat fluxes are very small compared to the axial heat fluxes at the cold end, ranging from −96 kW/m^2 to −120 kW/m^2. The extrapolation exercise at the hot end of the sample was more sensitive than at the cold end. This was because the slope of the extrapolated temperature profile (i.e., at $x = 170$ mm) for each data set was very close to zero but, in some instances, an order of magnitude apart. Consequently, the hot end axial temperature gradient estimation shows greater variance than that of the cold end. This result is, therefore, reflected in the variation of the estimated heat fluxes and heat transfer coefficients for the hot end.

Additionally, in relation to the hot end, it should be noted that the temperature at $x = \ell$ (from the extrapolated curve) is not equal to the heater reference temperature in each case, i.e., the profile does not reach the heater temperature. If the temperature profile did reach the heater temperature one might expect a very large h_x at $x = \ell$. Note, for example, in E.1 how T_x at $x = \ell$ is 5 °C below the heater reference temperature ($T_4 = 1680$ °C). This explains the magnitude and difference in values of the heat transfer coefficient at the hot end, since $h_x = q_x/(T_4 - T_x)$.

It should be noted that other authors neglect the heat flux at the hot end of the sample where the sample is relatively 'long and thin', for example, in reference [149] where the length-to-diameter ratio is 12.5 (17 in the case presented here). Alternatively, in other studies [56][57], and in a similar manner to the approach used here, a small nominal value for the heat flux at the hot end q_x is set at a fixed value during simulations.

Finally, note that from the model results the heat flux at the hot end of the sample has a minimal effect on the radial heat flux predictions in Fig. 5.9. At the cold end, however, the situation is different; the relatively large axial heat flux condition has a greater influence on the radial heat flux at $x = 0$.

Heat flux at the circumference of the sample

In Fig. 5.9 it is shown that the heat flux at the sample circumference in the cold zone is negative. This means that the controller extracts heat from the CVs in this region. Similarly, the heat flux at the sample circumference in the hot region is always positive, that is, the controller adds heat to CVs here. The transition from negative to positive heat flux occurs in the baffle region of the furnace. The transition from cold to hot zone (where the heat flux is zero) is therefore an adiabatic location. This result is cognisant with a simpler mathematical analysis. Rewriting equation (3.2) as a steady-state equation (removing the transient terms) giving,

$$\frac{\partial}{\partial x}\left(k\frac{\partial T}{\partial x}\right) = -\frac{2}{r_2}q_2 \quad . \tag{5.15}$$

If the radial heat flux q_2 is zero for an adiabatic condition, then the RHS of this equation is also zero. Hence, mathematically, any adiabatic location should correspond with a point of inflection in the temperature profile, i.e., the second derivative of temperature with respect to axial position. It can be shown that all of the temperature profiles in Fig. 5.8 share points of inflection in the vicinity of the baffle zone in the experimental apparatus. In Bridgman furnace terminology the baffle zone is sometimes called the adiabatic zone. The approach used here has independently confirmed the existence of the adiabatic condition within the baffle region.

It should be noted that a direct solution for equation (3.2) is difficult to obtain because of the non-linear nature of the problem and the inherent numerical difficulties with differentiating noisy experimental data. The problem is non-linear because thermal conductivity is a function of temperature and solid fraction. The approach adopted here—which is based on an integrative control volume algorithm—is a practical method for achieving the aims and objectives outlined at the beginning of this chapter.

The heat flux at the circumference of the crucible (q_3) is assumed to be due to *radiative* heat transfer only, as the experiments were carried out under vacuum. Since the heat flux at the circumference of the sample (q_2) is directly related to q_3 by equation (5.2), it is interesting to examine the result obtained in Fig. 5.9 with respect to the equation for radiative heat flux in concentric cylinders [128],

$$q_3 = F_{3 \to 5}\frac{\sigma A_3(T_3^4 - T_5^4)}{\dfrac{1}{\varepsilon_3} + \dfrac{1-\varepsilon_5}{\varepsilon_5}\left(\dfrac{r_3}{r_5}\right)} \quad , \tag{5.16}$$

where F is the radiation view factor (equal to 1 for concentric cylinders), σ is the Stefan–Boltzmann constant, A is the area through which the radiative heat flux acts, T is the surface

temperature in units of Kelvin, ε is the spectral emissivity, r is the radius of each cylinder, and subscripts '3' and '5' refer to the surfaces exchanging heat by radiation. In this case, '3' is the outer surface of the crucible and '5' is heater surface in the hot region of the furnace, or the inner surface of the crystalliser in the cold region. Assuming constant emissivities, equation (5.16) is a function of the term in brackets in the numerator, i.e., the difference between the temperatures of each surface to the power of 4. Using this equation, one would expect for q_3 to increase as this difference increases. Figure 5.11 shows how this occurs for the majority of the sample length.
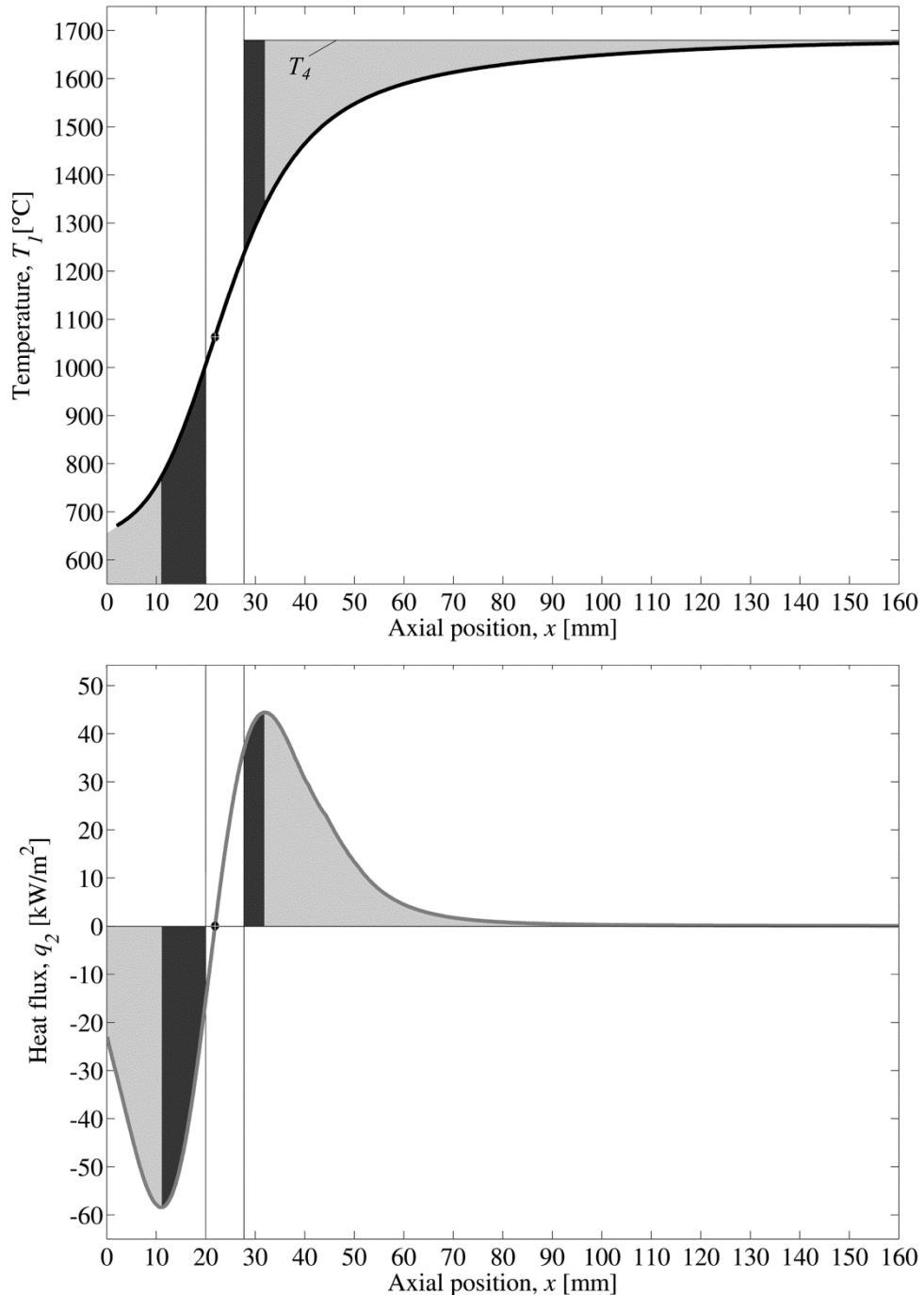

Fig. 5.11 Measured temperature profile for experiment E.1 (top) and heat flux at the sample circumference calculated via the PID controller (bottom) to give the same simulated temperature profile.

In this figure, the measured temperature profile plot for experiment E.1 is aligned above the corresponding plot for radial heat flux as calculated by the PID controller. The baffle zone ($x = 20$ to $x = 27$ mm) is the region between the two vertical lines through each plot. Assuming that, $T_4 \approx T_5$ and $T_1 \approx T_3$, it is clear that (looking at the light grey areas in both plots within this figure) the magnitude of the predicted heat flux is increasing as the difference between the temperatures of the surfaces exchanging heat is increasing. Therefore, the values predicted by the PID controller for q_2 in these regions qualitatively agree with equation (5.16).

Recall, from Section 5.3.1, that the PID controller does not distinguish between the hot and cold regions; rather it independently estimates where heat should be added or extracted at every position along the sample to make the simulated and experimental temperature profiles match. This method of implementation was a requirement; other simulations, where the PID controller was applied in the hot and cold regions only, and q_2 was set to zero in the baffle region, gave unrealistic results where a 'spike' in heat flux occurred very near to the junctions with the baffle zone. The approach used here ensures a continuous plot of heat flux as a function of x across the whole sample. This explains why the heat flux in the hot zone must decrease from its maximum value (at $x = 31$ mm), to zero within the baffle zone (at $x = 23$ mm). Similarly, in the cold region, the maximum absolute value of heat flux (at $x = 12$ mm) must decrease to zero in the baffle region (at $x = 23$ mm).

The dark grey areas in both plots do not follow the physical explanation that relates radiative heat flux to temperature difference applicable in the light grey areas. However, it is noted that the baffle region is not physically adiabatic; it is made up by a 5-mm thick annular aluminium oxide baffle ring and 2-mm gap (on the hot side). This means that from $x = 25$ mm to $x = 27$ mm the crucible surface is in view of the heater surface, albeit with a reduced view factor, i.e., less than 1. This provides a physical explanation for the mostly positive heat flux prediction in the baffle region produced by the PID controller.

Heat transfer coefficient at the circumference of the crucible

The method presented here estimates heat transfer coefficients using known reference temperatures in the heater and the crystalliser. For the heater system, the thermocouple for controlling the hot zone temperature is used to provide the reference temperature. Ideally, the surface temperature of the heater would have been used as the reference temperature; however, it is typical in high-temperature furnace designs to control the heater with a thermocouple in the vicinity of the heater which is not on the surface itself. This practical solution was deemed necessary and sufficient for future use. For the crystalliser, the reference temperature is simply the temperature of the water at the outlet of the crystalliser. This temperature was regulated throughout the experiments.

As discussed earlier, with reference to equation (5.1) and the study by Rosch et al. [147], the magnitude of the furnace heat transfer coefficient (at the crucible circumference) should increase in

proportion to a function of temperature cubed. However, this behaviour is not clearly apparent in the results presented here. Additional experiments over a wider range of temperatures would be required to confirm any dependence on the heater's temperature setting.

The heat transfer coefficient values (Fig. 5.10) are calculated directly from the results for the heat flux at the sample circumference (Fig. 5.9) by equation (5.4). It is proposed that the resulting heat transfer coefficient values obtained are, effectively, a bespoke 'signature' of the furnace design when modelled using the BFFTM.

Following on from the findings, it was possible to take the data from the results and develop an average value for the heat flux at the sample circumference and the heat transfer coefficient at the crucible circumference at each axial location. The averaged results are provided in Fig. 5.9 and Fig. 5.10. The averaged values could be applied to other scenarios providing that they are within a similar range of the operating parameters. This application is demonstrated next.

Average heat transfer coefficient at the circumference of the crucible

For demonstration purposes, the average heat transfer coefficient curve given in Fig. 5.10 is applied to independent simulation runs for each of the experimental trials. The PID controller is removed from the model; hence the simulations are direct calculations with no error correction. The adiabatic point that divides the hot and cold zones is given by the position of zero radial heat flux according to the averaged results, i.e., where the averaged heat transfer coefficient in Fig. 5.10 is zero ($x = 23.3$ mm). Figure 5.12 shows the resulting steady-state temperature profiles. It is clear that there is close agreement between experimental and simulated data. The level of agreement is better in the hot zone of the furnace than in the cold zone.
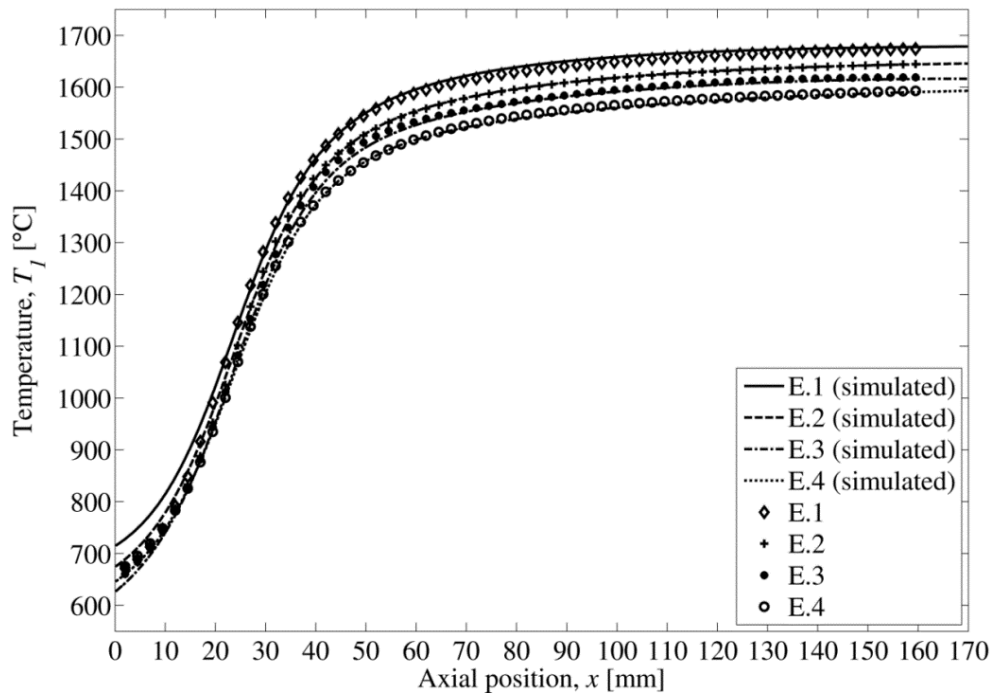

Fig. 5.12 Experimental and simulated temperature profiles using the average heat transfer coefficient.

5.5.2 Discussion of the 1-dimensional heat flow assumption

It is assumed that a 1-dimensional model for heat flow in the sample is reasonable for this problem given that a low Biot number exists at the surface of the sample, as discussed in Section 3.1. For the problem being addressed in this chapter, the heat transfer coefficient used to calculate the Biot number is referenced to the sample radius at r_2. This heat transfer coefficient, h_2, can be calculated by combining the thermal resistance of the crucible and the thermal resistance at the exposed side of the crucible wall, as per the method used by Fu et al. [167], as follows:

$$\frac{1}{h_2 r_2} = \frac{\ln(r_3 / r_2)}{k_{cru}} + \frac{1}{h_3 r_3} \quad . \tag{5.17}$$

From the results in Fig. 5.10, the maximum value observed for h_3—across all simulations—was $h_3 = 125$ W/m$^2 \cdot$°C, occurring in experiment E.2 at $x = 34.5$ mm. The resulting maximum heat transfer coefficient at the surface of the sample is then $h_2 = 170$ W/m$^2 \cdot$°C. Using h_2 to calculate the corresponding maximum Biot number yields, $Bi = 0.03$. This being the worst case scenario, the one dimensional heat flow assumption is justified.

5.5.3 Discussion on convection in the liquid

Using the BFFTM, thermo–solutal convection in the molten alloy and in mush regions is neglected for the following reasons. Firstly, in the experiment the sample is stationary, i.e., $u=0$, and the sample is allowed to settle for 300 s before measurements are taken. This is important in respect of solutal convection. For alloy 455, when $u > 0$, the primary component rejected at the interface during solidification is aluminium (45.5 at.%) having a partition coefficient of approximately $k_{part} = 0.9$. Since aluminium has a lower density than titanium, the aluminium rich liquid at the interface can become hydrostatically unstable during growth, leading to convection in the melt [168]. The secondary alloy component to consider is niobium (4.7 at.%) having a partition coefficient of approximately $k_{part} = 1.1$. This may also cause a destabilising effect on the melt. The partitioning of aluminium and niobium at the interface is a dynamic effect only present when $u > 0$. In any case, it should be noted that, since $k_{part} \approx 1$ for both aluminium and niobium in titanium, the partitioning is weak. It is assumed that any solutal convection—induced during the growth part of the experiment—has dissipated during the settling period of 300 s before the experimental measurements begin.

Secondly, in a vertical Bridgman furnace scenario the thermal gradient is parallel with the gravity vector. Given that the alloy used has a lower density at higher temperatures, the axial temperature gradient has a stabilising effect on convection in the melt. In addition, it is assumed that the sample is isothermal in the radial direction.

Where it is required to model the solidification of a multicomponent alloy, and the destabilising effects of convection in the liquid are to be accounted for, a suitable model should be considered such as the one demonstrated by Anderson et al. [169].

5.5.4 Discussion on heat flow in the crucible

It is assumed that heat flow in the crucible occurs in steady-state and in the radial direction only. However, it is probable that some axial heat flow occurs in the crucible. This assumption may introduce some error into the calculation of the heat transfer coefficient at the circumference of the crucible. A thought experiment, where the crucible is divided into annular volumes of thickness Δx, internal radius r_2 and external radius r_3, allows one to perform a qualitative heat balance exercise, as follows.

The value for q_2 is fixed by the PID controller so that the experimental and simulated temperatures match. From the point of view of the annular crucible volume, q_2 is negative as it is heat leaving the annular volume for the sample, and q_3 is positive as it is heat entering the annular volume. If some net axial heat flow were to occur in the crucible, the value for q_3 would have to change accordingly, so that q_2 is maintained.

While the approach used for predicting the heat transfer coefficient across the crucible does have potential for error—in respect of axial heat flow—it is noted that the method is consistent with other authors [167] using similar crucible geometries.

5.6   Conclusion

Firstly, the objectives of this chapter have been met, as follows:

(a)   The heat flux at both ends of the sample was estimated;
(b)   The heat transfer coefficient at both ends of the sample was estimated;
(c)   The heat flux at the circumference of the sample was estimated as a function of axial position using a combined experimental-numerical approach;
(d)   The heat transfer coefficient at the circumference of the crucible was estimated as a function of axial position.

The BFFTM is applied in this chapter—for the first time—to a gamma TiAl multicomponent hypoperitectic alloy (alloy 455, as referred to in Section 2.5.2). One main point of difference for modelling this alloy, as opposed to a hypoeutectic alloy or pure material, is in the estimation of solid fraction in the mushy zone. The solid fraction to temperature relationship, which affects the latent heat calculation within the BFFTM algorithm, is dealt with by the introduction of a pre-defined curve determined using a Scheil based CALPHAD method.

The method presented here estimates heat transfer coefficients using known reference temperatures in the heater and the crystalliser regions of the furnace. The resulting heat transfer coefficients can be used as benchmark input data for simulating other experiments performed using the same furnace, with similar operating conditions, and using the same alloy. (This is the subject of the following chapter.)

From a wider perspective, the approach used is useful to experimentalists and modellers, where the temperature of the furnace heater surface (or heat sink surface) T_5 is known *a priori*. In this case, the radiation heat transfer coefficients in the hot region of the furnace could be estimated,

a task that is normally quite difficult, due to uncertainty in values for the spectral emissivity of the surfaces exchanging heat. The method of using a PID controller for this purpose has not been previously reported in a Bridgman furnace analysis.

The usefulness of the method is demonstrated by re-running each simulation with the PID controller removed from the model. The average heat transfer coefficient curve is used to calculate the heat flux at the circumference of the sample. The resulting simulated temperature profiles closely matched the experimental data. The main assumptions of the method are discussed, namely; 1-dimensional heat flow in the sample, negligible convection effects in the liquid parts of the sample, and no axial heat flow in the crucible.

This chapter satisfies Objective 3 of this thesis, as given in Section 1.2. Now that the model has been developed, verified, and used to characterise an experimental Bridgman apparatus, the next step is to apply the model to Bridgman furnace experiments where traditional Bridgman solidification is combined in series with the power down method.

Chapter 6

Power Down Experiment Modelling

In this chapter, the BFFTM is applied to directional solidification experiments, as described by Lapin et al. [79], in the same Bridgman furnace apparatus as that used in the previous chapter. In these experiments, the traditional Bridgman solidification process is uniquely combined in series with the power down technique (over a range of cooling rates) and using alloy 455. The characterisation work from the previous chapter is used here to model these experiments accordingly. Referring to Section 1.2, this chapter addresses the fourth and fifth objectives of this thesis. Reference [170] is the main source of the content for this chapter. It is noted that the experiments and sample analysis detailed in this chapter were carried out by others, i.e., co-authors Lapin, Gabalcová and Hecht of reference [170].

In consideration of the experimental results, this chapter refers to the solidification morphology of hypoperitectic β-phase dendrites, observed in post-mortem analysis of samples. The BFFTM is used to interpret these results and to examine the critical growth conditions for CET that may occur during *transient* solidification.

While the CET phenomenon and various equiaxed nucleation models have been discussed in literature [48][49], only a few investigations focus on gamma TiAl alloys [87][152]. This is due to the experimental difficulties presented by handling the highly reactive melt and also because solidification patterns are easily lost, for example, being overrun by solid state transformations. One experimental difficulty can arise where unwanted radial temperature gradients lead to radial columnar growth instead of equiaxed growth at the expected location of CET. The BFFTM is used next to provide insight into this occurrence.

6.1   Methodology

In this section, a summary is given of the experimental apparatus, the experiment procedure and subsequent sample analysis, as carried out by Lapin et al. [79]. This is followed by details of the numerical model as applied to these experiments.

6.1.1 Experiment apparatus

Figure 6.1 shows a schematic of the Bridgman furnace apparatus and arrangement used in the experiments. The furnace is fully described elsewhere [152]. The hot zone of the furnace

comprised of a cylindrical molybdenum resistance heating element (300 mm in length and 33 mm in inside diameter) contained in a sealed low-pressure chamber. The hot and cold zones of the furnace were separated by a 5-mm thick annular baffle and a 2-mm gap (on the hot side). The cold zone consisted of a water-cooled 'crystalliser' having an inside diameter of 16 mm. Samples, 150 mm in length, were contained in a 2.5-mm thick yttrium oxide crucible. A fixed thermocouple, present near the outside wall of the crucible, was used to measure and control the furnace temperature.
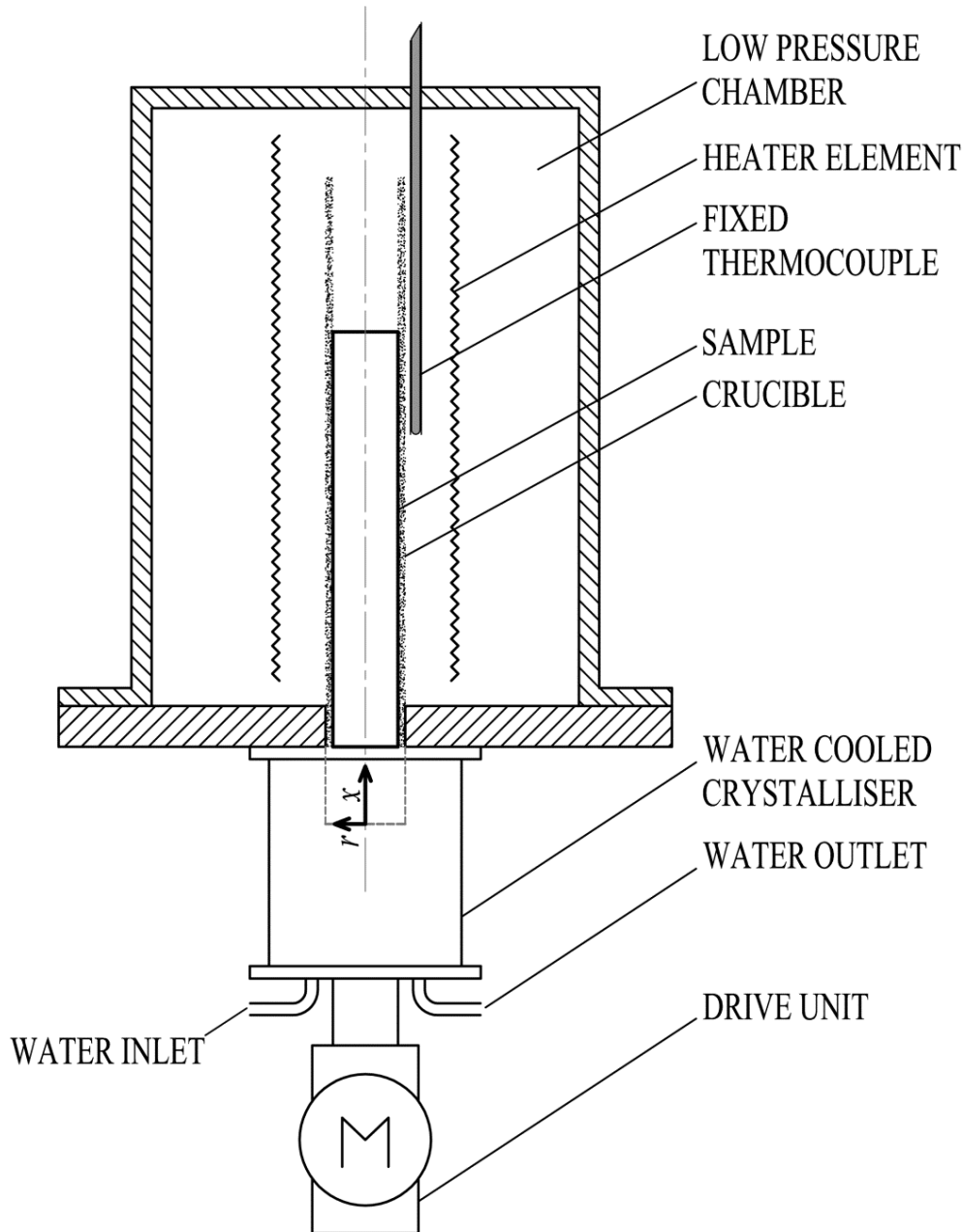
Fig. 6.1 Schematic of the Bridgman furnace apparatus.

6.1.2 Experimental procedure

The experiments were carried out under an argon atmosphere at constant absolute pressure of 10 kPa. The following five steps describe the procedure used.

- Step 1 (heating): the sample was heated until the fixed thermocouple read 1720 °C.

- Step 2 (stabilisation): the sample was allowed to stabilise at this temperature for 300 seconds.

- Step 3 (pulling): the sample—initially located as shown in Fig. 6.1, i.e., the cold end of the sample in line with the top of the water-cooled crystalliser—was pulled a distance of 20 mm into the crystalliser at a constant pulling rate of 2.78×10^{-4} m/s.

- Step 4 (controlled cooling): the furnace temperature was decreased in a controlled manner at a fixed cooling rate from 1720 °C to 1420 °C.

- Step 5 (uncontrolled cooling): the furnace was allowed to cool to room temperature without controlling the cooling rate.

This procedure was performed at four controlled cooling rates (step 4): 15 °C/min, 20 °C/min, 30 °C/min, and 50 °C/min, as such, the controlled cooling rate was the defining process parameter that distinguishes each experimental run. Figure 6.2 illustrates the experimental procedure steps by showing typical process signals for pulling rate, controlled cooling rate and thermocouple temperature, all versus time during each step of the procedure.
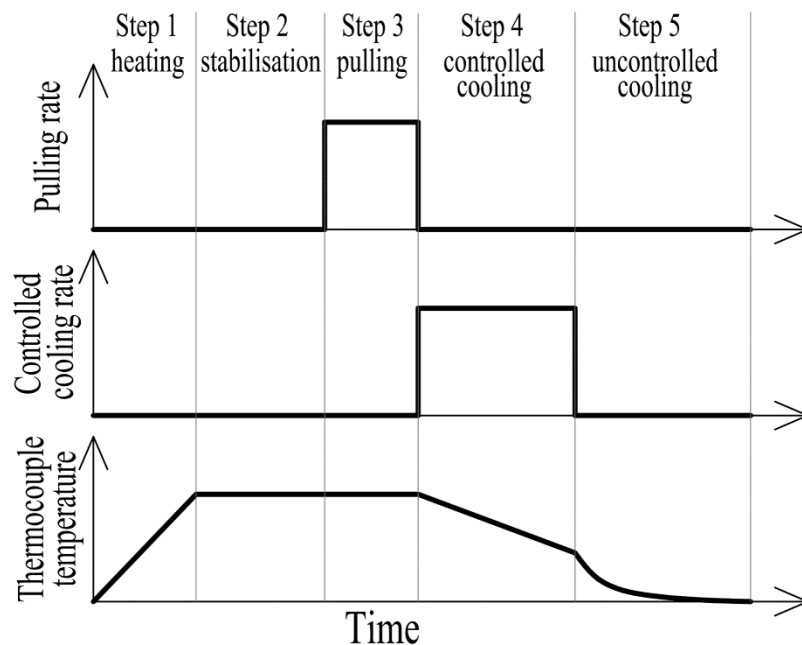
Fig. 6.2 Schematic plot of the process signals: pulling rate, controlled cooling rate, and thermocouple temperature, all versus time for the experimental procedure.

Note that Step 3 is the typical Bridgman mode of solidification, used here to induce initial columnar grain growth, while Step 4 is the typical power down mode. The pulling rate is the speed

at which the crucible is moved through the furnace. Incidentally, due to the transient nature of the experiment, the growth rate of columnar grains never equated to the pulling rate of the sample in the simulations that follow.

6.1.3 Sample analysis

The sample post-mortem analysis was carried out by optical microscopy. Chemically-etched samples were polished and examined under the stereo-microscope using; firstly, a grazing light at an approximate angle of 45° rotated into various positions to reveal each individual grain, and secondly, under flat light at 0° with the light beam parallel to the flat surface thereby revealing the primary dendrite structure (original β-phase) within each grain. The β-phase dendrite structure was used to distinguish columnar growth in the axial direction, columnar growth in the radial direction and equiaxed growth (if any) in each sample. The alloy composition was determined by chemical analysis using inductively coupled plasma (ICP) mass spectrometry and hot extraction.

6.1.4 Numerical model

The Bridgman Furnace Front Tracking Model (BFFTM)—described by Mooney et al. [126]—is a hybrid 1-dimensional transient model for axial heat flow in a cylindrical sample, solidified using the Bridgman method, where heat can be gained or lost radially at the circumference of the sample. The model uses an explicit finite difference control volume (CV) method to solve the following heat equation for temperature in a cylindrical rod of cross sectional area A, and perimeter p, moving at a pulling rate u,

$$\frac{\partial}{\partial t}\left(\rho c T\right) = \frac{\partial}{\partial x}\left(k\,\frac{\partial T}{\partial x}\right) - u\rho c\,\frac{\partial T}{\partial x} - \frac{hp}{A}\left(T - T_\infty\right) + E \quad, \tag{6.1}$$

where ρ, c and k are the density, specific heat capacity and thermal conductivity of the rod material, respectively; T_∞ is the temperature of the surrounding source (or sink), and E is the latent heat generated per unit volume. A heat transfer coefficient, h, applies to the radial heat flow at the circumference of the sample.

Figure 6.3 illustrates how the model is applied to the experimental apparatus. Figure 6.3(a) shows a schematic drawing of the physical aspects and geometry of the furnace: the cold zone (crystalliser), the baffle and air gap region (shown hatched), the hot zone (heater), and the cylindrical sample moving at some pulling rate, u, as a function of time.

Figure 6.3(b) shows the numerical features of the BFFTM as applied to this physical scenario. A fixed grid of disc-shaped control volumes (CVs), each of width Δx, make up the numerical domain that encompass the length of the sample. The front marker (×) position denotes the estimated location of the columnar dendrite tips, which have a growth rate, v_{tip}. This growth rate is calculated as a function of columnar dendrite tip undercooling, ΔT_{tip}, which is given by the difference between the equilibrium liquidus temperature for the alloy, T_l, and the dendrite tip

temperature, T_{tip}. The new front marker position, x^{m+1}, is updated over the numerical time step, Δt, by integrating the growth vector. The growth vector is the sum of the pulling rate and columnar growth rate (which act in opposing directions); hence,

$$x^{m+1} = x^m + \left(v_{tip} - u\right)\Delta t \quad , \tag{6.2}$$

where x^m is the previous marker position. (Note that this is equivalent to equation (3.11), however, the sample is being pulled, in this case, in the negative x-direction.)
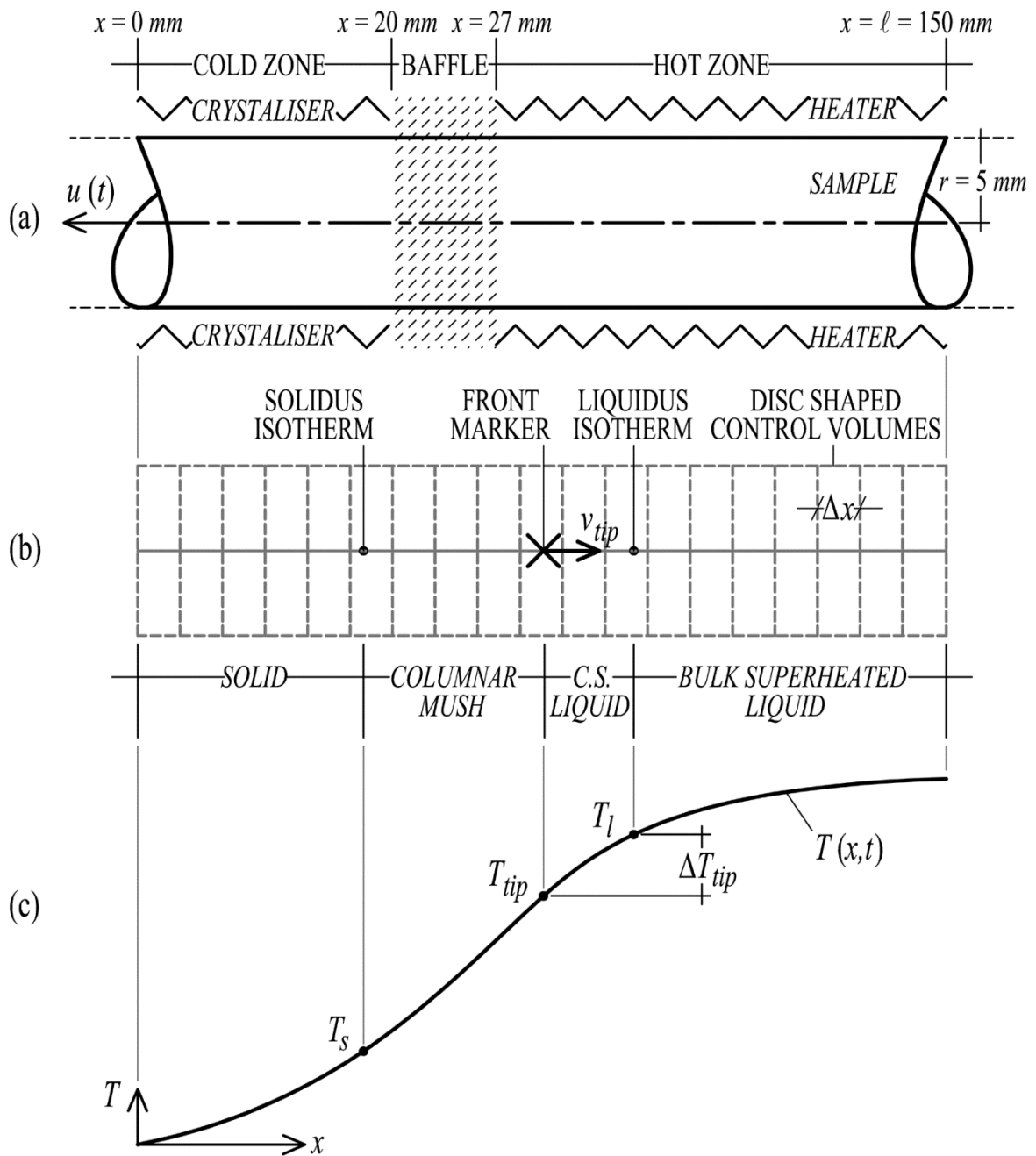
Fig. 6.3 (a) The physical model and (b) the numerical model of the Bridgman furnace apparatus aligned with (c) a typical sample temperature profile result.

Figure 6.3(c) shows a typical result for the temperature profile in a sample as produced by the model at some instance in time. The dendrite tip undercooling is due, primarily, to constitutional effects in the liquid. This is the constitutional undercooling, after Tiller et al. [41]. The extent of constitutionally undercooled liquid in the figure is shown as *C.U. LIQUID* and is given by the distance between the front marker and the equilibrium liquidus temperature isotherm. Liquid ahead of this isotherm is known as *BULK SUPERHEATED LIQUID*. The extent of the dendritic *COLUMNAR MUSH* is given by the distance from the front marker back to the position of the solidus marker, and material at a temperature below this isotherm is fully *SOLID*. The model predicts the thermal history in the sample, $T(x,t)$, and the columnar growth conditions: tip temperature, tip undercooling, temperature gradient at the tip and growth rate.

The material properties, numerical parameters, solid fraction to temperature relationship, and geometrical properties for the numerical simulations presented in this chapter were set as per Chapter 5, with the exception of sample length which was 20 mm shorter at 150 mm for the experiments described here. The simulation boundary conditions were also taken from Chapter 5, as the averaged result for heat transfer coefficient (as a function of axial position), and averaged result for heat flux at both ends of the sample.

6.2   Results

6.2.1 Experimental results

Following the sample microstructure analysis by stereoscope microscope, it was possible to identify distinct growth patterns of the primary β-phase. Figure 6.4 shows section images of the etched and polished samples, where image I is for the sample cooled at 15 °C/min, image II is for the 20 °C/min sample, image III is for the 30 °C/min sample, and image IV is for the 50 °C/min sample. In each sample the predominant growth pattern(s) of the primary β-phase was identified and the transition between each region is given by a solid white line in the figure.
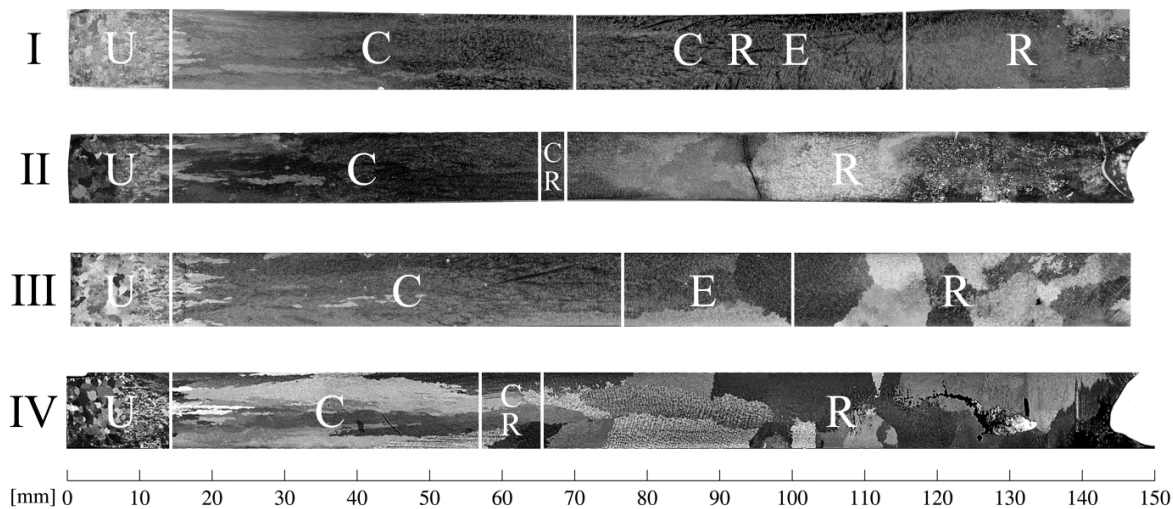
Fig. 6.4 Images of etched and polished samples with primary β-phase microstructure regions identified as follows: U–unmelted, C–axial columnar, R–radial columnar, and E–equiaxed.

Regions marked 'U' were unmelted during the procedure, regions marked 'C' had axial columnar growth, regions marked 'R' had radial columnar growth, and regions marked 'E' had equiaxed growth. In three of the samples—images I, II and IV—more than one of each growth structure type coexisted along the length of the sample. For example, in image I, the sample exhibited a region (from 70 mm to 115 mm, marked 'C R E') where axial columnar, radial columnar, and equiaxed grains coexisted. In images II and IV, axial columnar growth existed alongside radial columnar growth, which eventually choked the axial growth. These regions are marked 'C R'. The positions of each microstructural transition shown in Fig. 6.4 are listed in Table 6.1, with the exception of the 'U' to 'C' transition which was approximately the same for each sample at 14 mm. Figure 6.5 shows detailed images of: the 'C R E' region from image I; the 'C' to 'E' transition from image III; and the 'C', 'C R', and 'R' regions in image IV.
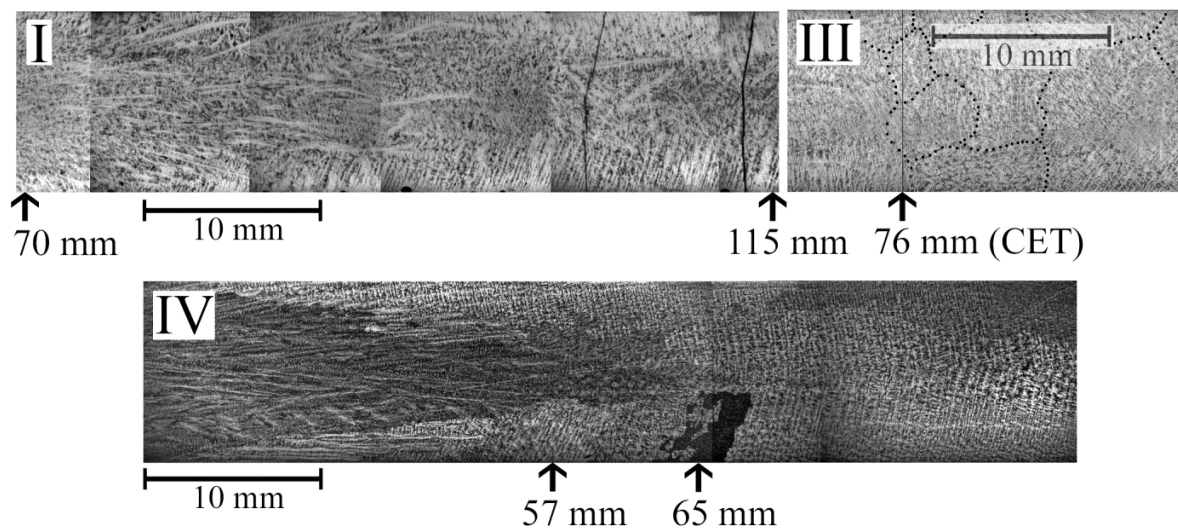
Fig. 6.5 Detailed images of samples I, III, and IV showing the typical microstructural regions observed.

Finally, The chemical analysis of the alloy samples by ICP and hot extraction returned the following alloy composition: Ti–45.5Al–4.7Nb–0.2C–0.2B (all at.%).

Table 6.1 Experimental results.

	Experiment No.							
	I		II		III		IV	
Controlled cooling rate [°C/min]	15		20		30		50	
Transition position [mm]	70	115	65	68	76	100	57	65
Transition type (marker)	C to C R E (↑)	C R E to R (♦)	C to C R (↑)	C R to R (♦)	C to E (CET)	E to R	C to C R (↑)	C R to R (♦)

95

6.2.2 Numerical results

The BFFTM simulated the conditions at the dendrite tip, namely, undercooling (ΔT_{tip}), growth rate (v_{tip}), and temperature gradient (G_{tip}), throughout the solidification process. Table 6.2 gives the simulated values for these variables at the *axial columnar* microstructural transitions. Since the model only simulates axial columnar growth, the model may only be used to interpret solidification conditions occurring during axial columnar growth and at the subsequent transition from the axial columnar structure (given by the top row of data in Table 6.2). This approach of modelling and analysing axial columnar growth in the absence of equiaxed solidification is known as the *indirect* approach and was successfully applied to CET analysis by McFadden et al. [56]. Discussion on the direct and indirect approaches to solidification analysis are available in McFadden et al. [55]. The simulated undercooled width for each axial columnar transition is also given in Table 6.2, i.e., the width of constitutionally undercooled liquid ahead of the columnar front at the moment the transition occurred.

Table 6.2 Measured axial columnar transition positions and corresponding numerical results.

	Simulation No.			
	I	II	III	IV
Axial columnar transition position [mm]	70	65	76	57
ΔT_{tip} [°C]	3.3	3.3	4.0	3.8
v_{tip} [mm/s]	0.0730	0.0739	0.128	0.1171
G_{tip} [°C/mm]	2.073	2.957	1.089	3.876
Undercooled width [mm]	1.6	1.1	3.7	1.0

The evolution of dendrite tip growth rate, and corresponding tip undercooling, are plotted against front position in Fig. 6.6 and Fig. 6.7, respectively.

Figure 6.8 shows dendrite tip growth rate plotted against temperature gradient at the dendrite tip. This type of graph is frequently used in CET modelling when a Hunt analysis [60] is performed and is sometimes known as a 'Hunt plot'. Each plot on the graph is a locus of temperature gradient and growth rate evolution at the columnar tips. Each plot in Fig. 6.8 should be interpreted by following the loci (all of which start on the *x*-axis) initially travelling from left to right before looping around in a clockwise direction, and continuing from right to left in the general direction towards the *y*-axis of the graph.

Finally, Fig. 6.9 shows a plot of the undercooled width (extent of bulk undercooled liquid ahead of the marker) versus front position. The transition type markers ('↑', '♦' and 'CET'), listed in Table 6.1, are included in each figure to demarcate the principal microstructural transitions observed in each experiment. As noted previously, the numerical model simulates axial columnar growth only, i.e., the model is valid up to and including the initial marker locations (up arrow '↑' or 'CET' markers).
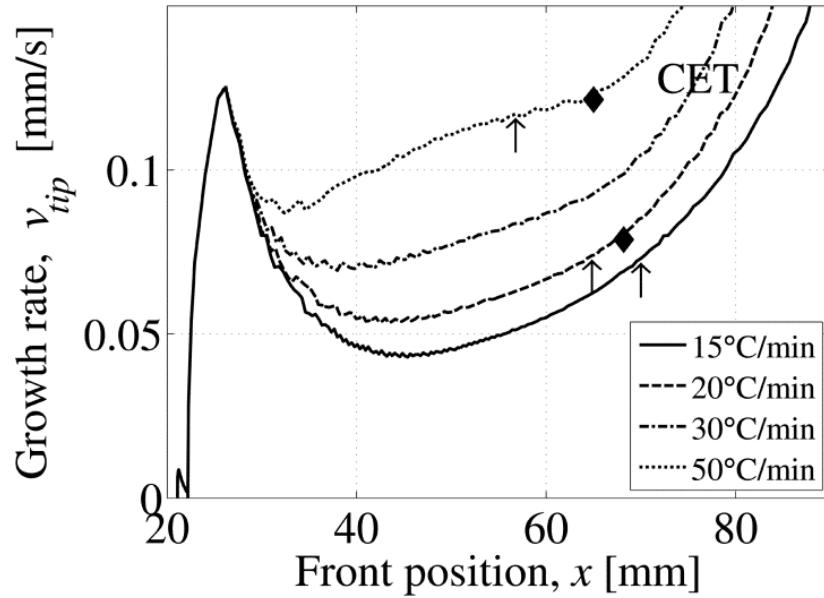
Fig. 6.6 Dendrite tip growth rate versus front position.
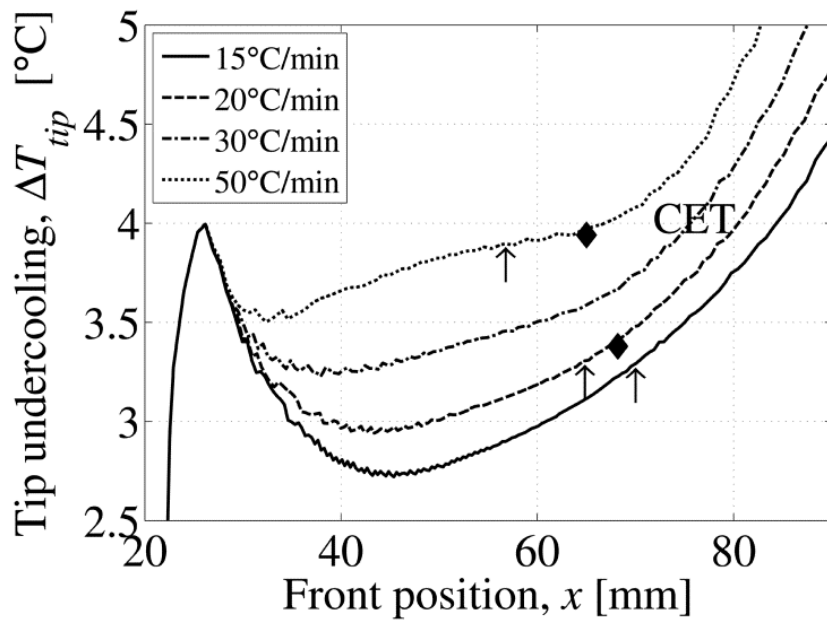
Fig. 6.7 Dendrite tip undercooling versus front position.
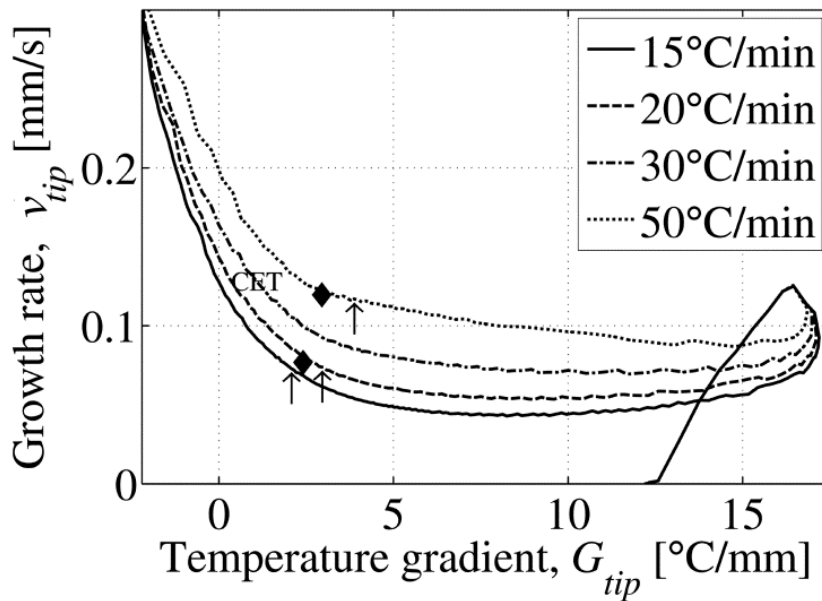
Fig. 6.8 Dendrite tip growth rate versus tip temperature gradient.
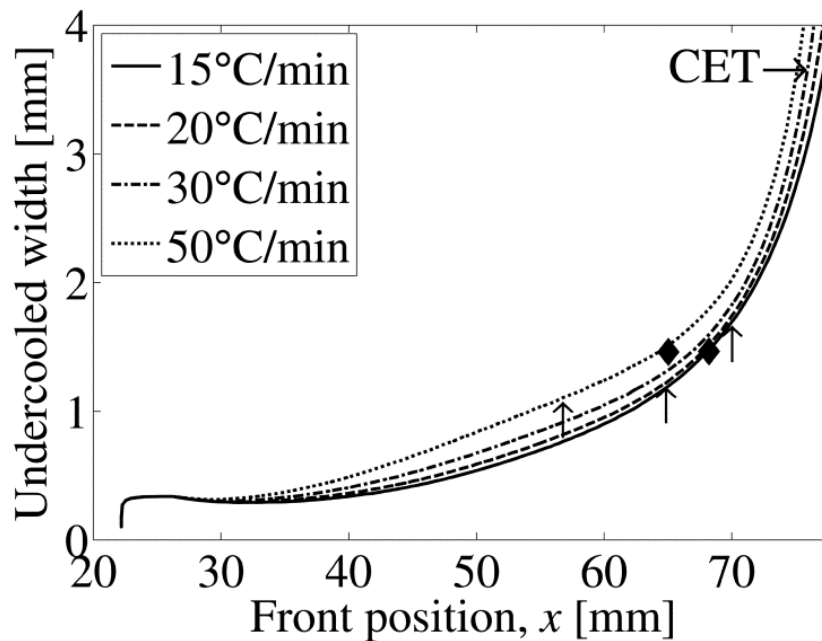
Fig. 6.9 Undercooled region width versus front position.

6.3 Discussion

6.3.1 Summary of experiment results

Only the dendritic primary β-phase was considered in the sample analysis. All of the samples revealed a distinguishable unmelted region approximately 14 mm long, labelled 'U' in Fig. 6.4, followed by period of columnar growth in the axial direction of the furnace, labelled 'C' in the same figure. Columnar to equiaxed transition was observed in only one of the four experimental samples (Fig. 6.4, image III) where the controlled cooling rate was 30 °C/min.

In the samples cooled at 20 °C/min and 50 °C/min, columnar growth in the radial direction was observed emanating from the circumference of the crucible. This led to 'choking' of axial columnar growth in these samples, so that *only* radial columnar microstructure was prevalent in the latter stages of solidification. Image 'IV' from Fig. 6.5 is reproduced below, in Fig. 6.10, with annotations to illustrate an example of such an occurrence. Axial columnar growth is overcome by radial columnar grains that appear to have nucleated at the circumference of the sample during solidification.
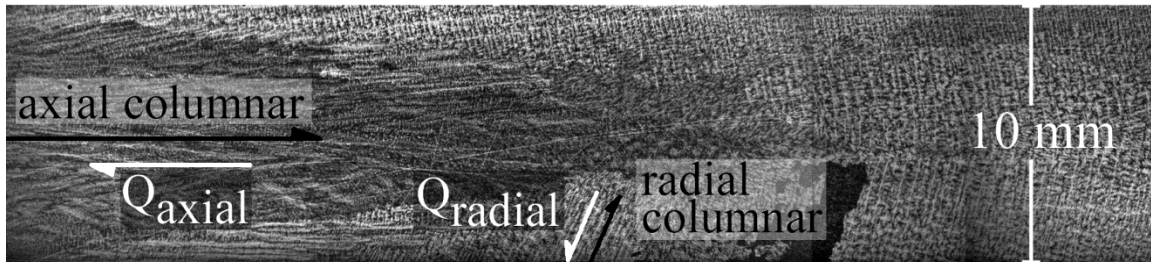
Fig. 6.10 Axial and radial columnar growth in the sample cooled at 50 °C/min.

In the sample cooled at 15 °C/min, axial columnar, radial columnar and equiaxed microstructures coexisted for a significant length of the sample until, eventually, a fully radial columnar microstructure was observed.

Similar results are found in the literature in directional solidification experiments using a gamma TiAl alloy of similar composition to that used in the experiments here. Mooney et al. [86] describe how radial columnar growth prevented the possibility of CET in power down experiments on board the MAXUS-8 sounding rocket. Kartavykh et al. [171] present terrestrial experiment results showing centreline segregation in cylindrical samples owing to radial temperature gradients.

6.3.2 Radial columnar growth

In directional solidification experiments investigating CET using the Bridgman or power down method, nucleation events at the circumference of the mould wall are normally an unwanted phenomenon. If the conditions allow, columnar grain growth in the radial direction can occur and subsequently interfere with the progress of columnar growth in the axial direction. In columnar grain growth, the preferred growth direction (100) is opposite to that of the heat flow. Figure 6.10 illustrates this, where the growth direction is shown and the heat flow direction is indicated by white arrows.

When a Bridgman furnace is used for directional solidification, a positive axial temperature gradient is desired so that heat flow occurs in the negative *x*-direction. In other words, when $dT/dx > 0$, heat flows axially to the cold zone (crystalliser). If a concurrent radial temperature gradient occurs at any axial position in the sample, i.e., $dT/dr \neq 0$, where *r* is the sample radius, heat may also flow in the radial direction. In this case, if $dT/dr > 0$ heat will flow radially into the sample from the surroundings and, conversely, if $dT/dr < 0$ heat will flow from the sample to the

surroundings. Note that, in accordance with Fourier's law, the direction of the axial (Q_{axial}) and radial (Q_{radial}) heat components occur in opposition to the sign of their respective temperature gradients.

Consider an axial section through the sample. The shape of the 2-dimensional columnar front (that joins all of the columnar dendrite tips in the section) is influenced by the direction of the radial heat flow component. A simple thought experiment shows that when both dT/dr and dT/dx are positive, one would expect a convex front shape, which will suppress radial columnar growth. This is illustrated in Fig. 6.11(a). Conversely, when dT/dx is positive and dT/dr is negative, one would expect a concave front shape which promotes radial columnar growth, as in Fig. 6.11(b). The latter case corresponds to the scenario observed in Fig. 6.10, and as such, is the undesirable case.

Fig. 6.11 Effect of radial heat flow direction on front shape: (a) desirable convex front shape, (b) unfavourable concave front shape.
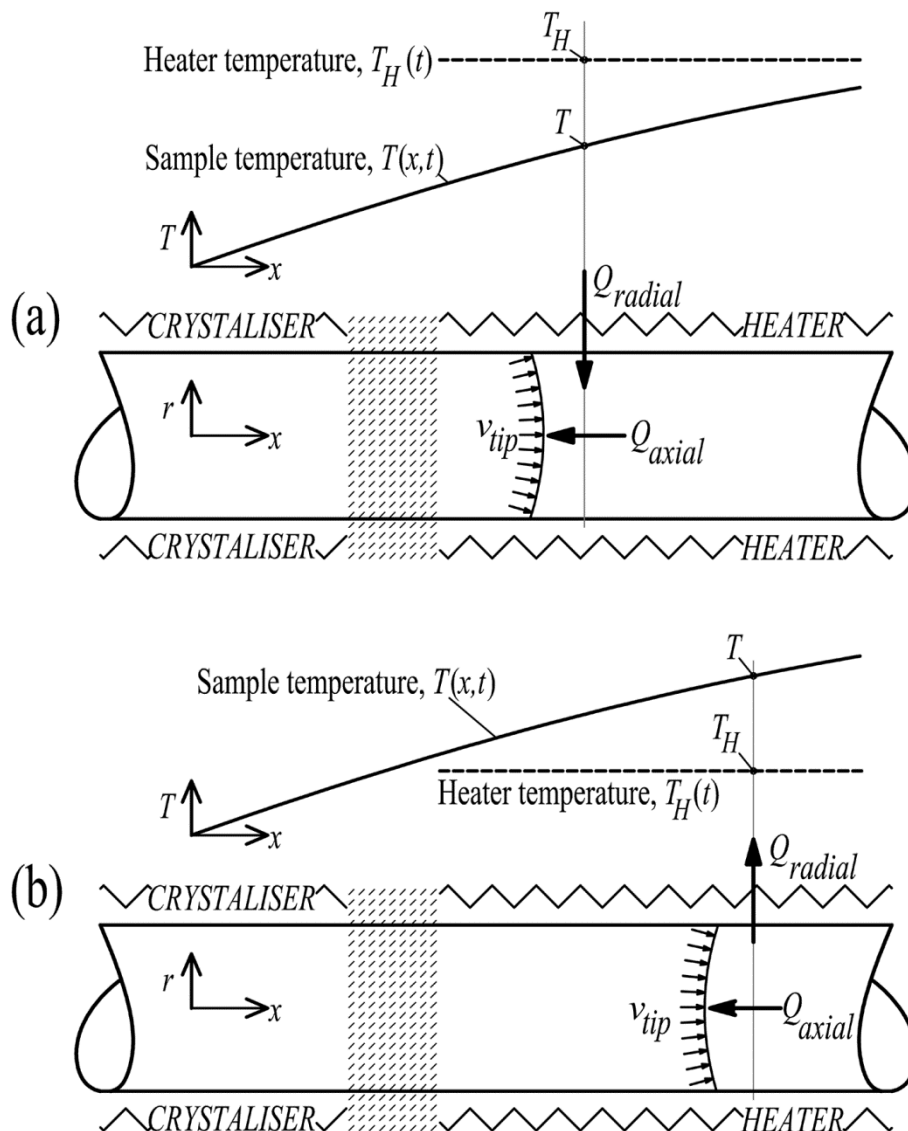
The BFFTM assumes that the temperature in a CV does not vary significantly in the radial direction. It does, however, account for heat flow at the circumference of the CV, i.e., radial heat

flow. This approach is suitable for situations, like the one presented here, with a low Biot number (less than 0.1). The direction of the axial and radial heat flow components—as predicted by the model—can be used to predict the most likely front shape to occur during solidification.

When the cooling phase begins the front is located at an axial location of approximately 25 mm, i.e., in the baffle region. Soon thereafter, the front moves into the hot region of the furnace (at 27 mm). At this point—in all simulations—the axial heat flow component, Q_{axial}, occurs in the negative x-direction, i.e., heat flows axially towards the cold zone, and Q_{radial} occurs in the negative r-direction, i.e., heat is received by the CV from the surroundings. This scenario is conducive to a convex (desirable) front shape, as illustrated in Fig. 6.11(a).

In the early stages of solidification, the front shape progresses in this convex manner. As cooling progresses, and the solidification front moves through the hot zone, at some point (due to the controlled cooling) the heater becomes cooler than the temperature at the front, $T_H < T$. In this case, the radial heat flow changes sign, and now radial heat flow (at the front position) is from the sample to the heater, i.e., Q_{radial} is in the positive r-direction. This is illustrated in Fig. 6.11(b). The BFFTM was used to determine the axial location at which the radial heat flow component—in the CV containing the front—changes sign, i.e., the position of *radial heat flow reversal*. The results of this exercise are given in Table 6.3. Three observations were made clear by this analysis: (1) radial heat flow reversal occurred in all samples, (2) the timing of the radial heat flow reversal lagged behind the moment the furnace switched from Bridgman to power down solidification, (3) radial heat flow reversal occurred earlier (closer to the cold zone) as the cooling rate was increased.

Table 6.3 Simulated positions of radial heat flow reversal.

	Simulation No.			
	I	II	III	IV
Position of radial flow reversal [mm]	63.0	58.8	52.9	46.0

No direct correlation is found by comparing radial heat flow reversal predictions with the onset of radial growth in the microstructures. It is considered that at the instant radial heat flow reverses, a zero radial gradient exists, and this should favour a flat solidification front. The radial growth will require some nucleation undercooling and a sufficient radial heat flow to initiate. However, it is clear that the radial heat flow reversal is a prerequisite for radial growth; therefore, the radial heat flow reversal is a necessary but insufficient condition for the onset of radial columnar growth.

It is interesting to note that the thermal scenario shown in Fig. 6.11(b) is difficult to achieve in traditional steady Bridgman solidification, since the heater temperature is always higher than that of the moving sample. Martorano et al. [172] did observe, however, radial columnar growth in experiments using the Bridgman method where large changes in pulling rate were applied, in other

words, transient Bridgman solidification. Both scenarios, (a) and (b) shown in Fig. 6.11, are possible when using the power down method in steady *or* transient conditions. The cooling rate influences the possibility of scenario 'Fig. 6.11(a)' leading to scenario 'Fig. 6.11(b)'. A low cooling rate delays the moment of radial heat flow reversal (causing it to occur further along the sample from the cold zone). A high cooling rate promotes an earlier onset of radial heat flow reversal with the reversal occurring closer to the cold zone.

6.3.3 Columnar to equiaxed transition

A full CET occurred in the sample cooled at 30 °C/min. It is well established in the literature that equiaxed nucleation and growth tends to occur ahead of columnar dendrites when growing at high growth rates and at low temperature gradients [48]. A high columnar growth rate implies that sufficient undercooling exists ahead of the columnar dendrites for equiaxed nucleation to occur. Although solutal undercooling at the columnar dendrite tip and constitutional undercooling in the liquid ahead of the tip are different, under constrained growth conditions, the undercooling at the tip gives a limiting value to the peak constitutional undercooling ahead of the tip. Figure 6.12 illustrates how the solutal undercooling at the tip and undercooling ahead of the tip are related (within a moving frame of reference, such that the x'-axis is fixed to the dendrite tip).
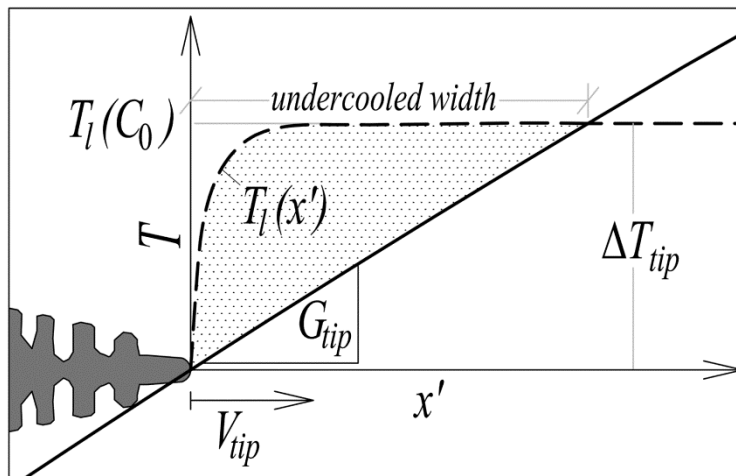
Fig. 6.12 The width of the undercooled region ahead of a columnar dendrite.

The dot-hatched region represents constitutionally undercooled liquid. In a positively partitioning system, the liquid in this region is enriched by solute rejected from the growing dendrite so that the equilibrium liquidus temperature, $T_l(x')$, is lower than its value for the original alloy composition, $T_l(C_0)$. Generally, if solutal undercooling at the columnar tip is increased or lowered, then the constitutional undercooling ahead of the tip is increased or lowered accordingly. In addition, if the temperature gradient decreases, then the undercooled width increases. Given a sufficient level of undercooling and the availability of nucleated particles in the melt, equiaxed crystals can nucleate and grow in the undercooled region ahead of the columnar tips. A low

gradient will reduce the likelihood of a strong preferential growth direction, hence leading to equiaxed growth.

The CET in the 30 °C/min sample occurred at the highest columnar growth rate, $v_{tip} = 0.128$ mm/s, and highest columnar tip undercooling, $\Delta T_{tip} = 4.0$ °C. However, this undercooling value is only marginally greater than the columnar tip undercooling values for the columnar to radial transitions in the other samples.

Figure 6.8 shows that the simulated temperature gradient is continually decreasing and approaching zero in all cases. The CET occurred at the lowest temperature gradient, $G_{tip} = 1.089$ °C/mm, when compared to the other columnar transitions (ranging from 2.073 °C/mm to 3.876 °C/mm). The lower temperature gradient increased the width of undercooled liquid ahead of the front, which in turn increased the likelihood of equiaxed grain nucleation in the undercooled liquid. The width of undercooled liquid ahead of the front at the position of CET was larger, at 3.7 mm, than that of the other columnar transitions: 1.0 mm to 1.6 mm. This is illustrated in Fig. 6.9.

6.3.4 Convection in the melt

Natural convection is defined as flow resulting from the effects of gravity on density differences, i.e., where a density gradient exists, in the liquid [9]. Such density differences in the liquid can be due to a temperature gradient (thermal convection), a concentration gradient (solutal convection), or both (thermo-solutal convection). The BFFTM does not consider heat transfer occurring due to natural convection in the liquid.

In the previous chapter (Section 5.5.3) some discussion is given on this. The discussion assumes that no radial temperature gradient exists in the liquid; and focusses on the fact that the crucible and sample do not move during the experimental procedure (resulting in a static columnar front). It is assumed that, since no growth is occurring, no solute is rejected at the columnar front, and any concentration gradient in the liquid has had time to equilibrate by chemical diffusion. Therefore, it is implied that no solutal convection exists. An axial thermal gradient does exist; but the gradient is aligned with the gravity vector (in a *vertical* Bridgman furnace), so that hotter (lower density) liquid overlays cooler (higher density) liquid, thereby providing an inherently stabilising effect on the liquid.

The situation, however, is different in the experimental procedure described in this chapter since the Bridgman apparatus is used for the purposes of directional solidification. While the thermal gradient is still aligned with the gravity vector), a concentration gradient in the liquid must exist during directional solidification. Whether the concentration gradient has a stabilising or destabilising effect on liquid depends on the density of solutes being rejected. The main elements contained in the solutes of alloy 455 (i.e., aluminium and niobium) both have a *destabilising* effect on the liquid during growth. Buoyant aluminium (less dense than titanium) is rejected at the columnar front, whilst—contrarily, but having the same effect on the density field—heavy niobium (more dense than titanium) is consumed from the melt during growth. However, partitioning is

weak in both cases: $k_{part} \approx 0.9$ for Al in Ti, and $k_{part} \approx 1.1$ for Nb in Ti. For this reason, it is appropriate to say that the results obtained in this chapter may contain a margin of error due to natural convection in the melt. The inclusion of natural convection in the current numerical model is a considerable undertaking and would be a logical next step in its development.

It should be noted that there are other mechanisms (apart from *natural* convection ahead of the columnar front) that can lead to convective flow in the Bridgman process. For example, flow in the mushy zone, shrinkage driven flow, and surface tension forces leading to Marangoni convection [9]. Incorporation of these mechanisms in the current model would, again, require considerable further effort.

6.4 Conclusion

Following a complete microstructural evaluation of all samples, and in consideration of the primary β-phase, it was found that CET occurred in the sample cooled at 30 °C/min only. The solidification modelling carried out explained the conditions that produced this CET, since, compared to the other microstructural transitions modelled, the CET position had the highest dendrite tip growth rate (v_{tip} = 0.128 mm/s), highest dendrite tip undercooling (ΔT_{tip} = 4.0 °C), the lowest temperature gradient (G_{tip} = 1.089 °C/mm) and the widest undercooled region (3.7 mm). In all of the other samples the axial columnar growth was interrupted by radial columnar growth, thus, preventing the possibility of CET in those samples.

The model highlights an important consideration for CET experiment designers who intend to use the power down method. High cooling rates can lead to a situation where the heater temperature is less than that of the liquid in the sample. This can subsequently lead to an unfavourable heat flow pattern that promotes radial columnar growth, thereby 'choking' undercooled liquid ahead of (axial) columnar grains and preventing the possibility of CET. Even though the radial temperature gradients, in the case presented here, were relatively small, the axial temperature gradient had to be decreased to a low value for CET, and, ultimately, the axial and radial gradients must have reached a similar order of magnitude.

In conclusion, CET studies using the power down method should utilise appropriate thermal modelling to ensure that the conditions promoting detrimental radial heat flow away from the sample in the hot zone are avoided. The use of large sample diameters and low cooling rates would delay the reversal of radial heat flow that is a precursor to radial growth. However, one should be mindful that sufficient undercooling in the liquid is required to allow for the nucleation and growth of equiaxed dendrites.

This chapter satisfies Objective 4 and Objective 5 of this thesis, as given in Section 1.2. The results presented in this chapter will directly assist in the preparations for microgravity experiments on-board the ESA sounding rocket mission: MAXUS-9 (planned for 2016), to investigate CET in gamma TiAl based alloys, as referred to by Lapin et al. [79].

Chapter 7

Discussion

This chapter provides a discussion on the dendrite kinetics growth law used to model columnar growth of alloy 455 in the BFFTM. This topic has not been discussed in any of the previous chapters. The discussion is given in three parts: background theory on dendrite kinetics for alloy 455, sensitivity analysis of dendrite kinetics, and discussion summary.

7.1 Background Theory on Dendrite Kinetics for Alloy 455

The dendrite kinetics growth law: $v_{tip} = 2.63 \times 10^{-6} \, \Delta T_{tip}^{2.79}$ {equation (5.14)}, is presented in Chapter 5 as a power law approximation for the columnar growth rate in alloy 455 as a function of tip undercooling. In this equation, C is the growth coefficient (equal to 2.63×10^{-6} m/s·°C^b) and b is the undercooling exponent (equal to 2.79). This growth law is applied in the BFFTM simulations described in Chapter 5 and Chapter 6. The values for C and b were obtained through a curve fitting exercise using individual data points for growth rate and tip undercooling calculated using the analytical KGT model, as applied to a constitutionally similar binary alloy (Ti–46at.%Al), after Rebow et al. [164]. Rebow et al. estimate the stability parameter (σ^*) in the KGT model to be equal to 0.0506, i.e., twice its normal value under the marginal stability criterion ($\sigma^*=1/4\pi^2$).

The reason for doubling the stability parameter in this way is explained and justified by Rebow and Browne [45]. Evidence exists to support dendrite tip radius selection according to the marginal stability criterion (where $\sigma^*=1/4\pi^2$) when growth is controlled by thermal diffusion [44]. For example, during the growth of a pure substance in an undercooled melt where the thermal properties of the liquid and solid are assumed equal. This is the *symmetric* model of diffusion. However, it is found that the marginal stability criterion underestimates the growth rate by a factor of two when growth is controlled by solutal diffusion [173][174]. For example, during the growth of an alloy from a supersaturated solution; in this case chemical diffusion in the liquid dominates and is negligible in the solid phase. This is the *asymmetric* model of diffusion.

In any case, the resulting growth law (with $\sigma^*=0.0506$) is an estimate at best since it is restricted to binary alloys. It is likely that the correct growth law parameter values for the multicomponent alloy 455 would vary somewhat from the values given in equation (5.14).

7.2   Sensitivity Analysis of Dendrite Kinetics

A very recent study by Mooney et al. [175] examines the effect of varying the growth law parameters values. Simulations of the power down experiment described in Chapter 6, for the sample cooled at 30 °C/min, are presented. (This is the experiment that produced a CET.) The growth law parameters are varied about the central values: $C = 2.63 \times 10^{-6}$ m/s·°C^b and $b = 2.79$, as taken from equation (5.14). Table 7.1 shows the range of values used. This represents a ±38% variation in C and a ±35% variation in b about the central values. Figure 7.1 shows how this gives a wide ranging spread in growth rate versus dendrite tip undercooling.

Table 7.1 Matrix of values for growth coefficient and undercooling exponent.

| | Undercooling exponent, b | | |
Growth coefficient, C [m/s·°C^b]	$b_1 = 1.79$ (*dotted*)	$b_2 = 2.79$ (dashed)	$b_3 = 3.79$ (solid)
$C_1 = 1.63 \times 10^{-6}$ (*grey*)	C_1, b_1 ········	C_1, b_2 - - - -	C_1, b_3 ———
$C_2 = 2.63 \times 10^{-6}$ (*dark grey*)	C_2, b_1 ········	C_2, b_2 - - - -	C_2, b_3 ———
$C_3 = 3.63 \times 10^{-6}$ (*black*)	C_3, b_1 ········	C_3, b_2 - - - -	C_3, b_3 ———
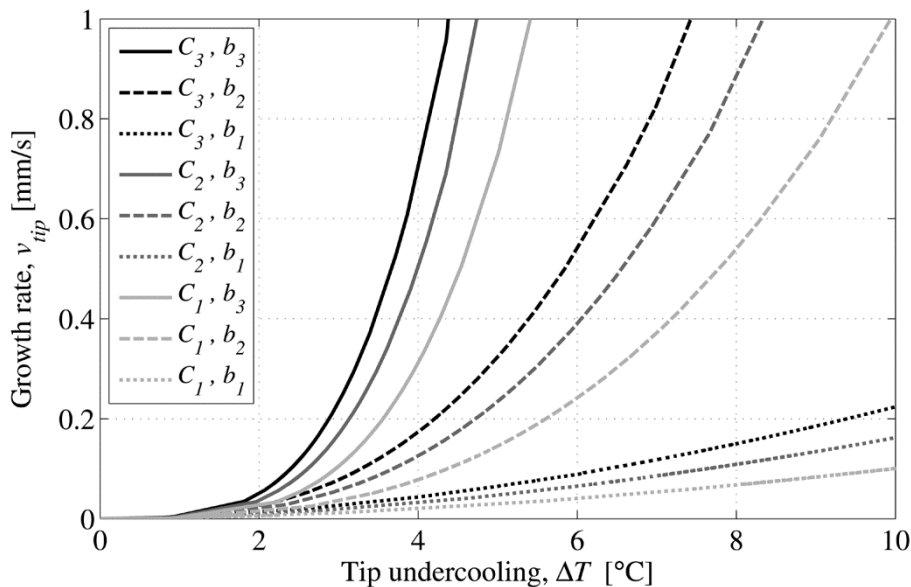
Fig. 7.1 Columnar dendrite tip growth rate versus dendrite tip undercooling for values of growth coefficient and undercooling exponent in Table 7.1.

Recalling Section 6.1.2, the experiment procedure steps were as follows: heating (step 1), stabilisation (step 2); pulling (step 3), controlled cooling (step 4), and uncontrolled cooling (step 5). In the simulation results that follow, the 'stabilisation' step begins at time, $t = 0$ s; the 'pulling' step begins at time, $t = 300$ s; and the 'controlled cooling' step begins at time, $t = 372$ s. Directional solidification begins at the start of the pulling period and continues in the controlled cooling period.

Figure 7.2 shows; (a) the simulated front position x, (b) the dendrite tip growth rate v_{tip}, and (c) the temperature gradient at the dendrite tip G_{tip}, plotted against simulation time t.
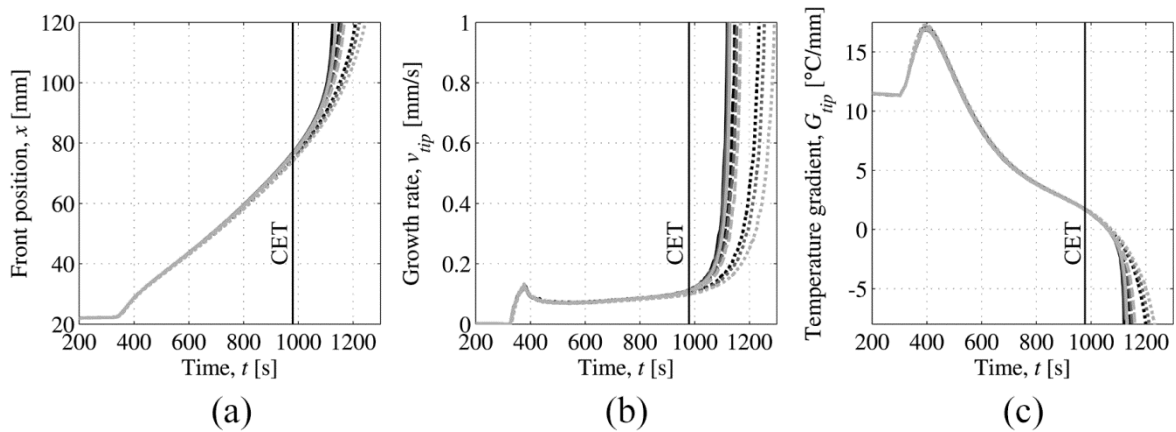
Fig. 7.2 Simulated front position (a), columnar tip growth rate (b) and tip temperature gradient (c) all versus time.

It is important to recall that the CET position measured by post mortem analysis in the experiment sample was $x = 76$ mm. Simulations are valid up to this position since the BFFTM simulates columnar growth only. According to the model predictions, the equivalent time taken for the columnar front to reach 76 mm is approximately 975 s, regardless of the growth parameters used. It is clear—from Fig. 7.2(a)—for $t < 975$ s, the simulated progress of the columnar front is practically unaffected by using different growth parameters. A similar outcome is observed in the simulated plots of tip growth rate, Fig. 7.2(b), and tip temperature gradient, Fig. 7.2(c).
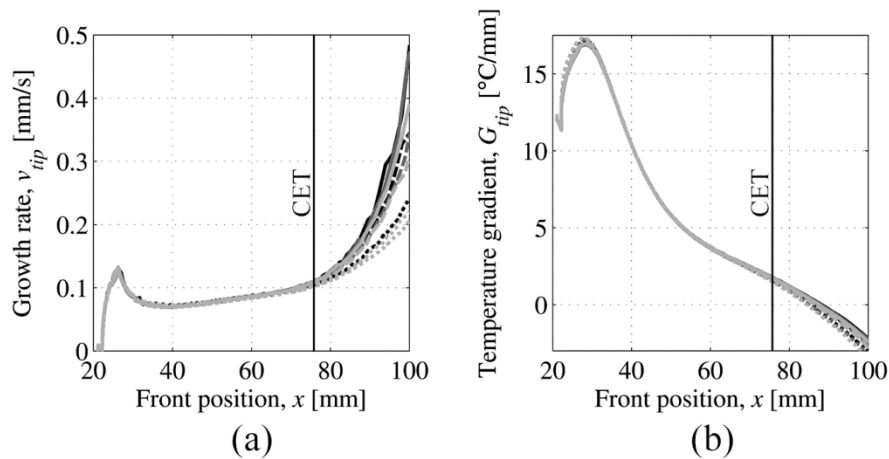
Fig. 7.3 Simulated tip growth rate (a) and tip temperature gradient (b) versus front position.

Figure 7.3 shows; (a) the simulated columnar dendrite tip growth rate, and (b) the simulated temperature gradient at the dendrite tip, plotted against columnar front position. In a similar manner to Fig. 7.2, the simulation results display an indifference to the various combinations of growth parameters, when plotted against front position, up to the point at which CET occurred. This observation is also well illustrated when the growth rate is plotted against temperature gradient, as in Fig. 7.4 (similar to a Hunt plot [60]). The position (on this plot) corresponding to the CET in the

sample is given by the intersection of each curve with the black line annotation labelled: 'CET (76 mm)'.
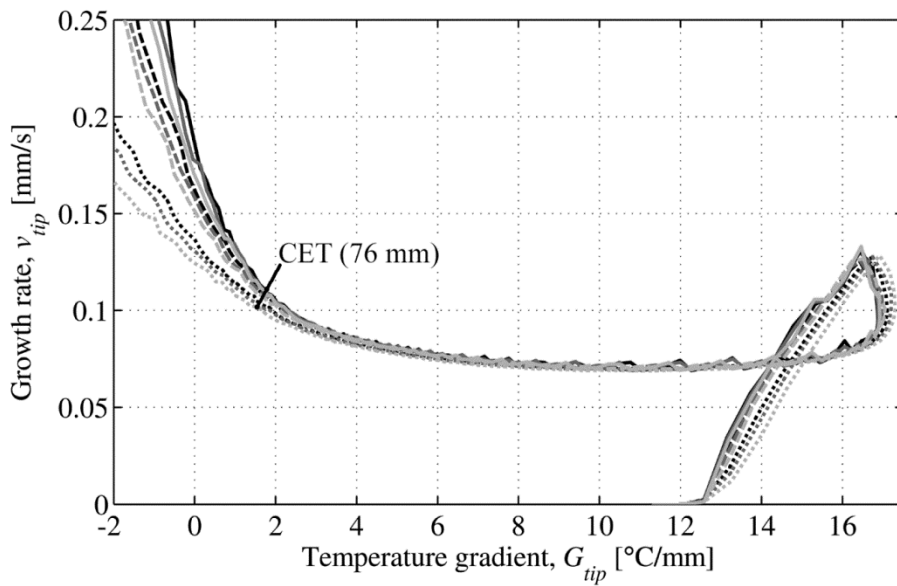
Fig. 7.4 Simulated columnar tip growth rate versus tip temperature gradient.

Figure 7.5 shows; (a) the simulated dendrite tip temperature, and (b) the undercooling at the dendrite tip, plotted against front position. The true effect of using different growth parameters is made clear in this figure. The plot lines do not overlap as before. The tip temperature, and consequently tip undercooling, vary accordingly so that the power law ($v_{tip}=C\Delta T^{b}$) delivers the growth rate required to satisfy the cooling conditions imposed on the sample by the process. Referring to Fig. 7.5(b), the simulated tip undercooling at CET for the central set of growth parameters (C_2, b_2) was 3.8 °C (*). The highest simulated tip undercooling at CET, ΔT = 10.1 °C (●), occurred with the lowest pair of growth parameters (C_1, b_1), and conversely, the lowest simulated tip undercooling at CET, ΔT = 2.5 °C (×), occurred for the highest pair of growth parameters (C_3, b_3).
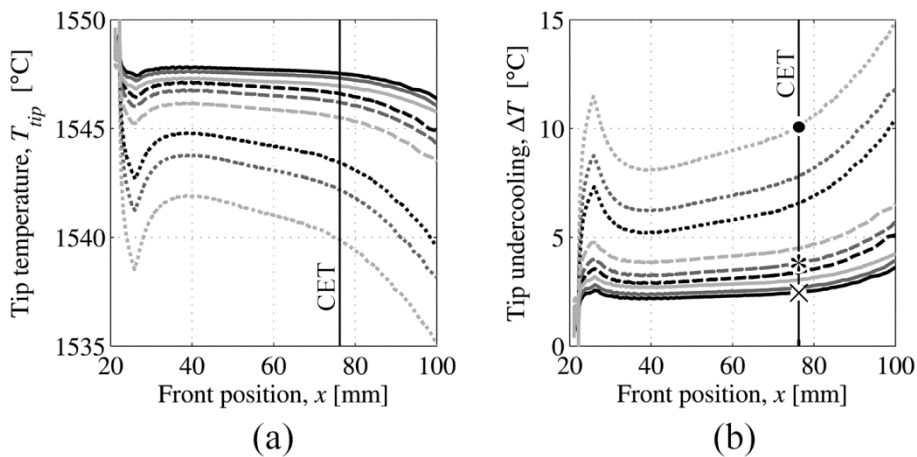
Fig. 7.5 Simulated tip temperature (a) and tip undercooling (b) versus front position.

Bearing in mind the magnitude of this variation, this is an important finding when considering the analysis of the microstructural transitions in the solidified sample, particularly when CET is present. It is accepted in the literature [56] that the condition of the bulk undercooled liquid ahead of the columnar front is important in predicting the onset of the equiaxed mushy zone and, hence, the CET. The extent of constitutional undercooling ahead of the columnar front is dependent on the tip undercooling and temperature gradient at the columnar front. Hence, accurate knowledge of the thermal conditions at the tip is required. It follows that having an accurate dendrite kinetic growth law for alloy 455 is important from the point of view of CET investigation.

Interestingly, these results demonstrate a particular shortcoming of the classic Hunt CET analysis, when applied to transient directional solidification. The Hunt analysis (developed for steady Bridgman solidification) considers the combination of G_{tip} and v_{tip} as the defining parameter set for predicting CET. In this case of CET, however, it is shown that the G_{tip}–v_{tip} plot is insensitive to a selection of dendrite growth parameters. Furthermore, the undercooling at the tip (which is an indicator of conditions for CET) is sensitive to the selected dendrite growth parameters. The analysis concludes that, for transient solidification conditions, a CET prediction criterion based on tip undercooling is preferable to one that uses growth rate.

7.3   Discussion Summary

The dendrite kinetics growth law used to simulate columnar growth in alloy 455 is discussed. The BFFTM employs a power law equation, in the form: $v_{tip}=C\Delta T_{tip}{}^{b}$, to estimate columnar growth rate (v_{tip}) as a function of dendrite tip undercooling (ΔT_{tip}). The genesis for calculating the growth parameters values (C and b) for alloy 455 is provided. The KGT model is applied to a constitutionally similar *binary* TiAl alloy where the stability parameter (σ^*) set to 0.0506 on the assumption of asymmetric chemical diffusion of solute during solidification. A power law curve fitting exercise is then carried out. The resulting growth law is an approximation. It is likely that the correct growth law parameter values for the *multicomponent* alloy 455 would vary somewhat from this approximation. This begs the question: what effect would varying these parameters have on the BFFTM simulations?

A sensitivity analysis on the growth law parameter values used to model alloy 455 is provided. Simulations are carried out of the power down experiment that yielded a CET in Chapter 6. A wide range of growth law parameter values are used in these simulations. The simulation results for front position, dendrite growth rate and tip temperature gradient show an indifference to the various combinations of growth parameter values up to the measured position of CET in the sample. The true effect of varying the growth parameter values manifests itself in the dendrite tip temperature and, hence, the tip undercooling. This is an important result when considering CET since the extent of constitutional undercooled liquid ahead of the columnar tip is dependent on tip undercooling. It follows that an accurate growth model is desirable when investigating CET.

Chapter 8

Conclusions and Future Work

8.1   Conclusions

A Bridgman furnace front tracking model (BFFTM) capable of modelling transient solidification conditions in a multicomponent TiAl alloy is presented in this thesis. The model developed employs a front tracking method from the literature to simulate columnar grain growth. The model is best described as a *hybrid* 1-dimensional model, since it permits 1-dimensional heat flow in the axial direction of a cylindrical sample, but also incorporates a radial heat flow component at the circumference of the sample. The radial component accounts for heat flowing to (or from) the tubular heat sink and heat source that make up the Bridgman furnace. The model is appropriate and useful for processes with a low Biot number, in other words, processes where an order of magnitude difference exists between the thermal resistance within the solidifying sample and the thermal resistance at its circumference. Hence, the model is applicable when radial temperature gradients are low. The model is capable of dealing with directional solidification using the traditional Bridgman method (where the sample is moved through the furnace) or using the power down method (where the sample is stationary and controlled cooling is applied to the sample by decreasing the heater temperatures). Both modes of solidification can be simulated using the model, as demonstrated in Chapter 6. The model permits steady or transient solidification and can be applied to any alloy given its thermophysical properties.

Referring to Section 1.2, the objectives of this thesis were as follows:

1. To develop a numerical model for transient Bridgman furnace solidification that incorporates a front tracking model from the literature.
2. Perform an order verification exercise on the numerical model using an analytical solution from the literature.
3. Characterise a Bridgman furnace experimental apparatus (in terms of heat transfer coefficients) using the numerical model and experimental data.
4. Apply the numerical model to directional solidification experiments (carried out in the same furnace) where the Bridgman method is combined in series with a power down method.

5. Use the numerical model to explain microstructural observations in the experiment samples and to provide insight into the experiment process.

Objective 1 was achieved in Chapter 3. A front tracking model from the literature was successfully adapted to numerically model Bridgman furnace solidification where transient conditions were applied (in this case, in the form of a step change in pulling rate). Practical issues for numerical implementation were explained, e.g., how to correctly deal with a front that moves bi-directionally (forward and backward) on a fixed grid during one time step in terms of latent heat release. Importantly, this chapter provides a useful procedure to find the initial temperature profile of a sample in a Bridgman furnace where the heat transfer coefficients in the hot and cold zones of the furnace are known. This procedure is of practical importance since it provides the initial condition temperature profile in the sample for the beginning of a Bridgman furnace experiment. The results obtained also demonstrated how columnar dendrite tip undercooling increased in response to a step change in pulling rate, a condition that can lead to CET in a real experiment.

Objective 2 was achieved in Chapter 4. Verification of the model for steady solidification of a pure material was carried out. The applied order verification procedure requires a suitable closed-form analytical solution to compare with the numerical results. It was not possible to find a solution from the literature for *transient* solidification of an *alloy* where the position of the dendrite tips could be predicted analytically. A solution does exist, however, for a *pure* material in a *steady* solidification scenario. This solution was successfully implemented in the order verification procedure. It was shown that global numerical error reduced with grid refinement and that the source of error was primarily truncation error. The BFFTM was verified as first order accurate in space.

Objective 3 was achieved in Chapter 5. A thorough characterisation exercise—which can be applied to any Bridgman furnace—was demonstrated that estimates the heat transfer coefficients at the sample circumference as a function of axial position. Other Bridgman furnace studies, references [26] and [143–148], assume fixed values for the heat transfer coefficient in the hot and cold zones, respectively; which may not accurately represent the furnace. The method presented in Chapter 5 is advantageous since it effectively provides tuned heat transfer coefficients from experimental data without the need for traditional calculation methods involving properties that are difficult to measure, e.g., spectral emissivity (when dealing with radiative heat transfer). The applied method gave the necessary data for further modelling, using the BFFTM, of subsequent experiments carried out in the same furnace.

Objective 4 and Objective 5 were achieved in Chapter 6. The results from the previous chapter were used to model the directional solidification experiments, carried out by Lapin et al. [79]. In these experiments the sample was initially translated through the furnace for a short period (traditional Bridgman method) before application of controlled cooling of the heater (power down method). The BFFTM was deemed suitable for modelling this procedure. Various solidification conditions, normally not measurable by experiment, were predicted using the model, e.g., columnar

dendrite tip growth rate, tip undercooling and temperature gradient at the tip. The modelling results were used to evaluate and provide insight into the microstructure observed in the solidified samples. The observed microstructures included CET and axial-columnar to radial-columnar transition. The analysis led to an important consideration for experiment designers when attempting to achieve CET using the power down method. Where high cooling rates are used—normally to achieve a high undercooling for equiaxed growth—a situation may arise where the direction of radial heat flow in the sample is reversed. In other words, heat flows radially from the sample towards the heater (in the hot zone). This leads to conditions that favour unwanted radial columnar growth, i.e., growth emanating from the circumference of the crucible wall. The reversal of radial heat flow at the sample circumference is proposed as an indicator for the onset of radial columnar growth in samples. In a general sense, the results provide useful insight into the power down process of directional solidification.

One advantage of the BFFTM is that temperature is not assumed *a priori*. This means that the temperature profile in the sample is not predetermined as an assumption; rather it is calculated within the BFFTM algorithm. This is particularly relevant to CET studies. It is common for models that examine the solutal field in the liquid melt, for example, in references [111] and [176], to assume a fixed thermal gradient in the liquid, on the basis that latent heat is extracted away from the liquid via columnar dendrites. Often in CET experiments, however, ideal conditions where a fixed temperature gradient can be correctly assumed are rare and difficult to prove; a point especially important when considering transient solidification. The BFFTM takes on this problem by continuously calculating (and recording) the temperature gradient at the columnar front.

Chapter 7 provides a detailed discussion on the dendrite kinetics used in the BFFTM to model columnar growth in the multicomponent alloy: alloy 455. The current growth model is based on an estimate for binary alloy solidification (of similar composition to alloy 455) and therefore requires further effort to accurately simulate dendritic growth of the multicomponent alloy. A sensitivity analysis exercise has shown that the effect of changing the growth law parameter values manifests itself in the simulated dendrite tip undercooling. The simulated growth rate and temperature gradient were practically unaffected up to the measured position of CET. This finding is important when considering the solidification conditions for CET, since equiaxed growth is strongly dependent on the degree of undercooling in the melt.

This work presented here is novel. Chapter 3 details the first adaption of the McFadden and Browne FTM [113] to Bridgman furnace solidification of a binary eutectic alloy, thereby creating the BFFTM. The BFFTM uses a new *hybrid* 1-dimensional heat flow treatment for processes with a low Biot number. The developed model can simulate transient solidification conditions, *viz.* by pulling rate changes in Bridgman solidification (as demonstrated in Chapter 3) and through changes in the furnace temperature gradient during power down solidification (as demonstrated in Chapter 6). In Chapter 4, the BFFTM was adapted for the first time—by necessity of model verification—to track the solid–liquid interface of a *pure* material. In Chapter 5, the

characterisation method used to determine heat transfer coefficients in a Bridgman furnace is novel. The approach of using a PID controller to solve the inverse heat transfer problem (and hence characterise the furnace) in this manner, has not been applied previously for this purpose. In addition, the furnace heat transfer coefficients are determined as a function of axial position, so the method used is more accurate than assuming a fixed heat transfer coefficient in each zone of the furnace. Also, latent heat release in a multicomponent peritectic alloy is dealt with for the first time (using the BFFTM) in this chapter. In Chapter 6, a unique solidification process is modelled; that is, Bridgman solidification in series with a power down technique. Finally, in Chapters 5 and 6, it is noted that the KGT model of dendrite kinetics is used in the BFFTM algorithm to estimate growth rate instead of the previously implemented Burden Hunt growth model [119] (inherited from the McFadden and Browne FTM [113]).

Some limitations of the current model are summarised next. From the beginning of model development it has been a prerequisite that the BFFTM is applied to processes with a low Biot number. This is clear limitation of the model. The BFFTM is not suitable to simulate columnar growth in samples of large diameter since the Biot number is a function of sample radius. For a fixed furnace heat transfer coefficient and a given material conductivity, if the sample radius is large enough the Biot number may have a value greater than 0.1; consequently, the 1-dimensional treatment of heat flow in the sample would not be valid. If the model were to be extended to 2-dimensional axisymmetric it would be possible to simulate columnar solidification in larger diameter samples.

Currently, the model has a radial heat component, applied in the 1-dimensional heat equation, equation (3.2), by way of lateral heat transfer at the sample circumference. Whilst this manages to account for heat supplied in the hot zone (or extracted in the cold zone), there is no means to calculate a radial temperature gradient *within* the sample. A 2-dimensional axisymmetric model would provide a means to calculate this. Following the discussion on convection in Chapter 6 (Section 6.3.4), this is an important point since radial temperature gradients in Bridgman solidification are known to lead to lateral density differences which produce convective flow regimes in the liquid [177][178]. A recent study by Kartavykh et al. [179] demonstrate the effect of this in a directionally solidified TiAl ternary alloy. Ultimately, the BFFTM is limited from a convection point of view; as convection (of any type) in the liquid is not treated.

8.2   Future Work

The capability of the BFFTM has been demonstrated in this thesis. The results are sufficiently encouraging to suggest future extension of the model. Initially, improvements to more accurately model the dendrite kinetics of a multicomponent peritectic alloy are suggested. This is followed by suggestions for other potential improvements to the BFFTM and other relevant modelling exercises.

Chapter 7 provides a detailed discussion centred on the dendrite kinetics growth law used to model columnar growth of a TiAl multicomponent alloy (alloy 455). A number of alternative, and potentially better, modelling approaches from the literature suitable to model columnar dendritic growth of alloy 455 are suggested next.

The KGT columnar growth model is widely applied in the solidification modelling of binary alloys, for example, in this thesis and in references [122] and [180]. This growth model is not easily applicable to multicomponent alloys (because of its binary origins) without significant assumptions. Cockcroft et al. [181] demonstrate a method where the KGT model is applied to the multicomponent single crystal alloy CMSX-4 [182]. Using this method, the liquidus slope (m_l) and partition coefficient (k_{part}) for each alloying element in the solvent material is extracted from the literature (or by other means, e.g., using CALPHAD methods) giving equivalent 'pseudo-binary' values of these parameters for the multicomponent alloy, according to the following equations:

$$\overline{C}_0 = \sum_j C_{0,j} \quad , \quad \overline{m}_{l,j} = \frac{\sum_j m_{l,j} \cdot C_{0,j}}{\overline{C}_0} \quad , \quad \overline{k}_{part} = \frac{\sum_j m_{l,j} \cdot C_{0,j} \cdot k_{part,j}}{\overline{m}_{l,j} \cdot \overline{C}_0} \quad , \quad (8.1)$$

where the subscript 'j' refers to the number of alloy components. These values are then used as normal in the KGT calculation. However, this method assumes that the solute fields at the dendrite tip for each solute species can be superimposed and that the diffusion coefficients each solute species are the same. This approach may be useful to model alloy 455 as an alternative to the model used in Chapter 5 and Chapter 6, however, at present this has not yet been tested.

Another, more advanced, modelling method potentially suitable to estimate the dendrite kinetics of alloy 455 is outlined by Hunziker [183]. In this approach any number of components can be considered and diffusive interactions between solutes in the liquid are accounted for. The model applies marginal stability theory, but effectively iterates to find the appropriate stability parameter, starting at $\sigma^* = 1/(2\pi)^2$. A limitation of this method is that it requires knowledge of the diffusion coefficients for each solute; currently this information is unknown for alloy 455.

Referring to Section 2.4.3, some existing peritectic growth models appear to be unreliable, working well with some alloys but not for others. The model outlined by Tourett and Gandin [71], however, incorporates the widely used KGT model to account for concomitant growth of the dendritic β-phase and peritectic α-phase. Whilst still restricted to binary alloys, this approach may be useful to accurately model the peritectic growth kinetics of alloy 455, since it considers the growth of the α-phase (not treated in this work).

Ultimately, the estimation of the stability parameter, σ^*, is a very important consideration for all of the above mentioned models, since this defines the product of dendrite tip radius squared times the dendrite tip growth rate for any given value to dendrite tip undercooling. Microsolvability theory—first applied to diffusion controlled growth by Kessler and Levine

[184]—provides an alternative method of independently calculating the stability parameter. The method takes into account the solid–liquid interface energy, γ, and crystalline anisotropy strength, ε. However, both interface energy and anisotropy strength tend to be difficult to measure; neither have been measured (in the literature) for alloy 455.

It is important to note that none of the above growth models have been tested or validated by the author for use with alloy 455. Therefore, it is inappropriate to comment as to which model would be most suited. To validate any of these models an experimental procedure capable of measuring columnar dendrite growth rate and temperature at the dendrite tip would be required. Ultimately, the motivating factor in finding an improved growth model would be to more accurately estimate dendrite tip undercooling in simulations (for the reasons given in Chapter 7).

Other suggested improvements to the BFFTM, in the generic sense of the model, are considered next. The existing model has been verified (using an order verification procedure) against a steady-state analytical model. It is desirable to verify the model in the transient case. An exact solution to the transient problem must be found to do this. At present the author is not aware of such a solution in the literature. Alternatively, transient verification could be overlooked through validation of a transient solidification scenario with appropriate experimental data. A study by Schmachtl et al. [185] provides such data. In this study an ultrasonic pulse-echo method is used to measure the position and growth rate of the solid–liquid interface during transient Bridgman solidification (by a step change in pulling rate) of a Cu–Mn binary alloy. Alternatively, the experiments that use synchotron x-ray videomicroscopy, e.g., as in references [22–25], could be used as validation data, since the position of the columnar dendrite front can be measured in real-time.

One significant improvement for the BFFTM would be to model heat flow in the axial *and* radial directions within the sample, as opposed to only in the axial direction. This would be possible by increasing the dimensionality for the governing process heat equation from hybrid 1-dimensional to 2- dimensional axisymmetric. While this would significantly improve the BFFTM in terms of radial heat flow estimation, a considerable effort would be required in terms of code re-design, re-writing, testing and code order verification.

Extension of the model to simulate columnar growth in a 2-dimemsional domain would provide a means to model natural convective flow in the liquid. The approach of Banaszek et al. [122] and, more recently, Mirihanage et al. [124] would be appropriate in this case since both of these studies have their genesis in the original FTM of Browne and Hunt [114]. To further treat convection in *multicomponent* alloys two studies are relevant; that of Trivedi et al. [168] and Anderson et al. [169].

The BFFTM model is of value to the industrial and research communities. As discussed in Section 1.1.2, the Bridgman method is used in industry for directional solidification, for example, to produce single crystal materials for semiconductors and photovoltaics, and also in metal purification. The model could be applied in industry to provide insight into the solidification

conditions in existing Bridgman processes and in the design of new furnaces. Also, as discussed in Section 1.1.3, the Bridgman method has been used in a wide spectrum of solidification research experiments. The BFFTM could be applied (further than this work) to model any of these studies.

A very recent study by Miller and Pollock [186] may be of particular interest for further modelling work. In their study, the authors examine the change in dendrite morphology and interface shape in two multicomponent alloys, solidified using the Bridgman method with liquid metal cooling (LMC). LMC provides enhanced radial heat extraction that can sometimes lead to *lateral* growth, in other words, radial columnar growth. They provide experimental and numerical results, and propose a criterion to predict lateral growth. It would be interesting to apply the BFFTM to these experiments and to compare their numerical results with the 'radial heat flow reversal' criterion proposed in Chapter 6.

Finally, with reference to the last paragraph of Section 6.4, and as part of the ESA GRADECET research group, the author intends to apply the BFFTM to model new experimental data from recent preparatory power down experiments with a re-designed version of the three zone furnace described in reference [86]. The new furnace has been modified to combat unwanted radial columnar growth in samples of gamma TiAl and will be launched on the MAXUS-9 sounding rocket in 2016.

Bibliography

[1]   P. W. Bridgman, "Certain physical properties of single crystals of tungsten, antimony, bismuth, tellurium, cadmium, zinc and tin," *Proc. of the American Academy of Arts and Sciences*, vol. 60, p. 303, 1925.

[2]   D. C. Stockbarger, "The production of large single crystals of lithium fluoride," *Review of Scientific Instruments*, vol. 7, no. 3, pp. 133–136, 1936.

[3]   W. Kurz and D. J. Fisher, *Fundamentals of solidification*. Aedermannsdorf: Trans Tech Publications, 1986.

[4]   J. A. Dantzig and M. Rappaz, *Solidification*, 1st ed. Lausanne: EPFL Press, 2009.

[5]   T. Duffar and L. Sylla, "Vertical Bridgman Technique and Dewetting," in *Crystal Growth Processes Based on Capillarity*, T. Duffar, Ed. John Wiley & Sons, Ltd, 2010, pp. 355–411.

[6]   A. Goetzberger and C. Hebling, "Photovoltaic materials, past, present, future," *Solar Energy Materials and Solar Cells*, vol. 62, no. 1, pp. 1–19, 2000.

[7]   Crystran, "Lithium Fluoride (LiF)." [Online]. Available: http://www.crystran.co.uk/optical-materials/lithium-fluoride-lif. [Accessed: 15-Jul-2014].

[8]   A. Kermanpur, N. Varahraam, E. Engilehei, P. Mohammadzadeh, and M. Davami, "Directional solidification of Ni base superalloy IN738LC to improve creep properties," *Materials Science and Technology*, vol. 16, no. 5, pp. 579–586, 2000.

[9]   D. M. Stefanescu, *Science and Engineering of Casting Solidification*, 2nd ed. Springer, 2008.

[10]   K. A. Jackson and J. D. Hunt, "Transparent compounds that freeze like metals," *Acta Metallurgica*, vol. 13, no. 11, pp. 1212–1215, Nov. 1965.

[11]   T. Sato, W. Kurz, and K. Ikawa, "Experiments on Dendrite Branch Detachment in the Succinonitrile-Camphor Alloy," *Transactions of the Japan Institute of Metals, Vol. 28 No. 12*, 1987. [Online]. Available: http://www.jim.or.jp/journal/e/28/12/1012.html. [Accessed: 26-Jan-2012].

[12]   G. L. Ding, W. D. Huang, X. Huang, X. Lin, and Y. H. Zhou, "On primary dendritic spacing during unidirectional solidification," *Acta Materialia*, vol. 44, no. 9, pp. 3705–3709, 1996.

[13]   J. E. Simpson, S. V. Garimella, and H. C. De Groh, "Experimental and numerical investigation of the Bridgman growth of a transparent material," *Journal of Thermophysics and Heat Transfer*, vol. 16, no. 3, pp. 324–335, 2002.

[14]   N. Bergeon, R. Trivedi, B. Billia, B. Echebarria, A. Karma, S. Liu, C. Weiss, and N. Mangelinck, "Necessity of investigating microstructure formation during directional solidification of transparent alloys in 3D," *Advances in Space Research*, vol. 36, no. 1, pp. 80–85, 2005.

[15] C. Weiss, N. Bergeon, N. Mangelinck-Noël, and B. Billia, "Declic scientific program - Directional solidification," in *AIAA 57th International Astronautical Congress, IAC 2006*, 2006, vol. 2, pp. 876–882.

[16] A. Ludwig and J. Mogeritsch, "In Situ Observation of Coupled Peritectic Growth," in *John Hunt International Symposium*, 2011, pp. 233–241.

[17] J. P. Mogeritsch, A. Ludwig, S. Eck, M. Grasser, and B. J. McKay, "Thermal stability of a binary non-faceted/non-faceted peritectic organic alloy at elevated temperatures," *Scripta Materialia*, vol. 60, no. 10, pp. 882–885, 2009.

[18] J. P. Mogeritsch and A. Ludwig, "In-situ observation of coupled growth morphologies in organic peritectics," *IOP Conference Series: Materials Science and Engineering*, vol. 27, p. 012028, Jan. 2012.

[19] J. Alkemper, S. Diefenbach, and L. Ratke, "Chill casting into aerogels," *Scripta Metallurgica et Materiala*, vol. 29, no. 11, pp. 1495–1500, 1993.

[20] J. Fricke and A. Emmerling, "Aerogels—Preparation, properties, applications," in *Chemistry, Spectroscopy and Applications of Sol-Gel Glasses*, vol. 77, R. Reisfeld and C. JJørgensen, Eds. Springer Berlin / Heidelberg, 1992, pp. 37–87.

[21] J. Alkemper, S. Sous, C. Stöcker, and L. Ratke, "Directional solidification in an aerogel furnace with high resolution optical temperature measurements," *Journal of Crystal Growth*, vol. 191, no. 1–2, pp. 252–260, 1998.

[22] R. H. Mathiesen and L. Arnberg, "X-ray radiography observations of columnar dendritic growth and constitutional undercooling in an Al–30wt%Cu alloy," *Acta Materialia*, vol. 53, no. 4, pp. 947–956, Feb. 2005.

[23] D. Ruvalcaba, R. H. Mathiesen, D. G. Eskin, L. Arnberg, and L. Katgerman, "In situ observations of dendritic fragmentation due to local solute-enrichment during directional solidification of an aluminum alloy," *Acta Materialia*, vol. 55, no. 13, pp. 4287–4292, Aug. 2007.

[24] D. Ruvalcaba, R. H. Mathiesen, D. G. Eskin, L. Arnberg, and L. Katgerman, "In-Situ analysis of coarsening during directional solidification experiments in high-solute aluminum alloys," *Metallurgical and Materials Transactions B: Process Metallurgy and Materials Processing Science*, vol. 40, no. 3, pp. 312–316, 2009.

[25] G. Reinhart, N. Mangelinck-Noël, H. Nguyen-Thi, T. Schenk, J. Gastaldi, B. Billia, P. Pino, J. Härtwig, and J. Baruchel, "Investigation of columnar–equiaxed transition and equiaxed growth of aluminium based alloys by X-ray radiography," *Materials Science and Engineering: A*, vol. 413–414, pp. 384–388, Dec. 2005.

[26] C. E. Chang and W. R. Wilcox, "Control of interface shape in the vertical bridgman-stockbarger technique," *Journal of Crystal Growth*, vol. 21, no. 1, pp. 135–140, 1974.

[27] R.J. Naumann, "An analytical approach to thermal modeling of Bridgman-type crystal growth: I. One-dimensional analysis," *Journal of Crystal Growth*, vol. 58, no. 3, pp. 554–568, 1982.

[28] R.J. Naumann, "An analytical approach to thermal modeling of bridgman-type crystal growth: II. Two-dimensional analysis," *Journal of Crystal Growth*, vol. 58, no. 3, pp. 569–584, 1982.

[29] C.-A. Gandin, R. J. Schaefer, and M. Rappax, "Analytical and numerical predictions of dendritic grain envelopes," *Acta Materialia*, vol. 44, no. 8, pp. 3339–3347, 1996.

[30] W. Kurz, B. Giovanola, and R. Trivedi, "Theory of microstructural development during rapid solidification," *Acta Metallurgica*, vol. 34, no. 5, pp. 823–830, 1986.

[31] D. H. Kim and R. A. Brown, "Modelling of the dynamics of HgCdTe growth by the vertical Bridgman method," *Journal of Crystal Growth*, vol. 114, no. 3, pp. 411–434, 1991.

[32] J. A. Burton, R. C. Prim, and W. P. Slichter, "The Distribution of Solute in Crystals Grown from the Melt. Part I. Theoretical," *The Journal of Chemical Physics*, vol. 21, no. 11, p. 1987, Nov. 1953.

[33] E. Scheil, "Bemerkungen zur schichtkristallbildungle," *Zeitschrift Fur Metallkunde*, no. 34, pp. 70–72, 1942.

[34] G. T. Neugebauer and W. R. Wilcox, "Convection in the vertical Bridgman-Stockbarger technique," *Journal of Crystal Growth*, vol. 89, no. 2–3, pp. 143–154, 1988.

[35] T.-W. Fu and W. R. Wilcox, "Rate change transients in Bridgman-Stockbarger growth," *Journal of Crystal Growth*, vol. 51, no. 3, pp. 557–567, 1981.

[36] R.-J. Su, W. A. Jemian, and R. A. Overfelt, "Transient effects in the directional solidification of Al-Cu alloys," *Journal of Crystal Growth*, vol. 179, no. 3–4, pp. 625–634, 1997.

[37] M. Saitou and A. Hirata, "Numerical calculation of two-dimensional unsteady solidification problem," *Journal of Crystal Growth*, vol. 113, no. 1–2, pp. 147–156, 1991.

[38] J. Eiken, M. Apel, V. T. Witusiewicz, J. Zollinger, and U. Hecht, "Interplay between α(Ti) nucleation and growth during peritectic solidification investigated by phase-field simulations," *Journal of Physics Condensed Matter*, vol. 21, no. 46, 2009.

[39] C.-Y. Li, S. V. Garimella, and J. E. Simpson, "Fixed-grid front-tracking algorithm for solidification problems, part I: Method and validation," *Numerical Heat Transfer, Part B: Fundamentals*, vol. 43, no. 2, pp. 117–141, 2003.

[40] C.-Y. Li, S. V. Garimella, and J. E. Simpson, "Fixed-grid front-tracking algorithm for solidification problems, part II: Directional solidification with melt convection," *Numerical Heat Transfer, Part B: Fundamentals*, vol. 43, no. 2, pp. 143–166, 2003.

[41] W. A. Tiller, K. A. Jackson, J. W. Rutter, and B. Chalmers, "The redistribution of solute atoms during the solidification of metals," *Acta Metallurgica*, vol. 1, no. 4, pp. 428–437, 1953.

[42] R. Trivedi and W. Kurz, "Dendritic growth," *International Materials Reviews*, vol. 39, no. 2, pp. 49–74, 1994.

[43] G. P. Ivantsov, "Temperature field around a spheroidal, cylindrical and acicular crystal growing in a supercooled melt," *Doklady Akademiya Nauk SSSR*, vol. 58, p. 567, 1947.

[44] J. S. Langer and H. Müller-Krumbhaar, "Theory of dendritic growth—I. Elements of a stability analysis," *Acta Metallurgica*, vol. 26, no. 11, pp. 1681–1687, Nov. 1978.

[45]   M. Rebow and D. J. Browne, "On the dendritic tip stability parameter for aluminium alloy solidification," *Scripta Materialia*, vol. 56, no. 6, pp. 481–484, Mar. 2007.

[46]   J. Lipton, M. E. Glicksman, and W. Kurz, "Dendritic growth into undercooled alloy metals," *Materials Science and Engineering*, vol. 65, no. 1, pp. 57–63, Jul. 1984.

[47]   C.-A. Gandin, "Experimental study of the transition from constrained to unconstrained growth during directional solidification," *ISIJ international*, vol. 40, no. 10, pp. 971–979, 2000.

[48]   J. A. Spittle, "Columnar to equiaxed grain transition in as solidified alloys," *International Materials Reviews*, vol. 51, no. 4, pp. 247–269, Aug. 2006.

[49]   J. Hutt and D. StJohn, "The origins of the equiaxed zone -Review of theoretical and experimental work," *International Journal of Cast Metals Research*, vol. 11, no. 1, pp. 13–22, 1998.

[50]   W. C. Winegard and B. Chalmers, "Supercooling and dendritic freezing in alloys," *Transactions of the American Society of Metals*, vol. 46, pp. 1214–1224, 1954.

[51]   B. Chalmers, "The structure of ingots," *Journal of the Australian Institute of Metals*, vol. 8, no. 3, pp. 255–263, 1963.

[52]   K. A. Jackson, J. D. Hunt, D. R. Uhlmann, and T. P. Seward, "On the origin of the equiaxed zone in castings," *Transactions of the Metallurgical Society of AIME*, vol. 236, pp. 151–158, 1966.

[53]   R. T. Southin, "Nucleation of the equiaxed zone in cast metals," *Transactions of the Metallurgical Society of AIME*, vol. 239, pp. 220–225, 1967.

[54]   A. Ohno, T. Motegi, and H. Soda, "Origin of the equiaxed crystals in castings," *Transactions of the Iron and Steel Institute of Japan*, vol. 11, no. 1, pp. 18–23, 1971.

[55]   S. McFadden, D. J. Browne, and J. Banaszek, "Prediction of the Formation of an Equiaxed Zone Ahead of a Columnar Front in Binary Alloy Castings: Indirect and Direct Methods," in *Materials Science Forum*, 2006, vol. 508, pp. 325–330.

[56]   S. McFadden, D. J. Browne, and C.-A. Gandin, "A Comparison of Columnar-to-Equiaxed Transition Prediction Methods Using Simulation of the Growing Columnar Front," *Metallurgical and Materials Transactions A*, vol. 40, no. 3, pp. 662–672, Jan. 2009.

[57]   C.-A. Gandin, "From Constrained to Unconstrained Growth During Directional Solidification," *Acta Materialia*, vol. 48, no. 10, pp. 2483–2501, Jun. 2000.

[58]   C. A. Siqueira, N. Cheung, and A. Garcia, "Solidification thermal parameters affecting the columnar-to-equiaxed transition," *Metallurgical and Materials Transactions A: Physical Metallurgy and Materials Science*, vol. 33, no. 7, pp. 2107–2118, 2002.

[59]   D. J. Browne, "A New Equiaxed Solidification Predictor from a Model of Columnar Growth," *ISIJ International*, vol. 45, no. 1, pp. 37–44, 2005.

[60]   J. D. Hunt, "Steady state columnar and equiaxed growth of dendrites and eutectic," *Materials Science and Engineering*, vol. 65, no. 1, pp. 75–83, 1984.

[61]   M. Avrami, "Granulation, Phase Change, and Microstructure Kinetics of Phase Change. III," *The Journal of Chemical Physics*, vol. 9, no. 2, p. 177, Dec. 1941.

[62]   W. U. Mirihanage, "Modelling of Columnar to Equiaxed Transition in Alloy Solidification (Thesis)," University College Dublin, 2010.

[63]   M. A. Martorano, C. Beckermann, and C.-A. Gandin, "A solutal interaction mechanism for the columnar-to-equiaxed transition in alloy solidification," *Metallurgical and Materials Transactions A: Physical Metallurgy and Materials Science*, vol. 34 A, no. 8, pp. 1657–1674, 2003.

[64]   W. D. Callister Jr., *Material Science and Engineering*, 3rd ed. John Wiley & Sons, 1994.

[65]   H. Fredrikksson, "Solidification of Peritectics," *ASM Handbook, Volume 15 - Casting*, pp. 125–129, 1988.

[66]   H. W. Kerr and W. Kurz, "Solidification of peritectic alloys," *International Materials Reviews*, vol. 41, no. 4, pp. 129–164, 1996.

[67]   H. Fredriksson, "On the Peritectic Reaction and Transformation in Metal Alloys," in *John Hunt International Symposium*, 2011, pp. 219–232.

[68]   W. P. Bosze and R. Trivedi, "On the Kinetic Expression for Growth of Precipitate Plates," *Metallurgical Transactions*, vol. 5, no. 2, pp. 511–512, 1974.

[69]   H. Fredriksson and T. Nylén, "Mechanism of peritectic reactions and transformations," *Metals Science*, vol. 16, pp. 283–294, 1982.

[70]   D. Phelan, M. Reid, and R. Dippenaar, "Kinetics of the peritectic reaction in an Fe–C alloy," *Materials Science and Engineering: A*, vol. 477, no. 1–2, pp. 226–232, 2008.

[71]   D. Tourret and C.-A. Gandin, "A generalized segregation model for concurrent dendritic, peritectic and eutectic solidification," *Acta Materialia*, vol. 57, no. 7, pp. 2066–2079, 2009.

[72]   E. A. Loria, "Gamma titanium aluminides as prospective structural materials," *Intermetallics*, vol. 8, no. 9–11, pp. 1339–1345, Sep. 2000.

[73]   D. M. Dimiduk, "Gamma titanium aluminide alloys—an assessment within the competition of aerospace structural materials," *Materials Science and Engineering: A*, vol. 263, no. 2, pp. 281–288, May 1999.

[74]   M.F. Ashby, *Materials Selection in Mechanical Design*. Pergamon Press, Oxford, 1992.

[75]   H. Wang, G. Djambazov, K. A. Pericleous, R. A. Harding, and M. Wickins, "Modeling of the Tilt-Casting Process for the Tranquil Filling of Titanium Alloy Turbine Blades," in *Proc. Modeling of Casting, Welding, and Advanced Solidification Processes XII*, 2009, pp. 53–60.

[76]   B. P. Bewlay, M. Weimer, T. Kelly, A. Suzuki, and P. R. Subramanian, "The Science, Technology, and Implementation of TiAl Alloys in Commercial Aircraft Engines," *MRS Proceedings*, vol. 1516, pp. 49–57, Jan. 2013.

[77]   "GEnx Aircraft Engine," 2014. [Online]. Available: http://www.ecomagination.com/portfolio/genx-aircraft-engine. [Accessed: 08-Apr-2014].

[78] H. Clemens and W. Smarsly, "Light-Weight Intermetallic Titanium Aluminides – Status of Research and Development," *Advanced Materials Research*, vol. 278, pp. 551–556, Sep. 2011.

[79] J. Lapin, Z. Gabalcová, U. Hecht, R. P. Mooney, and S. McFadden, "Columnar to Equiaxed Transition in Peritectic TiAl Based Alloy Studied by a Power-Down Technique," *Materials Science Forum*, vol. 790–791, pp. 193–198, 2014.

[80] J. L. Murray (Ed.), *Phase Diagrams of Binary Titanium Alloys*. Metals Park, OH: ASM International, 1987.

[81] H. Okamoto, "Al-Ti (aluminum-titanium)," *Journal of Phase Equilibria*, vol. 14, no. 1, pp. 120–121, Feb. 1993.

[82] H. Okamoto, "Al-Ti (aluminum-titanium)," *Journal of Phase Equilibria*, vol. 21, no. 3, pp. 311–311, May 2000.

[83] J. Schuster and M. Palm, "Reassessment of the binary Aluminum-Titanium phase diagram," *Journal of Phase Equilibria and Diffusion*, vol. 27, no. 3, pp. 255–277, 2006.

[84] V. T. Witusiewicz, A. A. Bondar, U. Hecht, S. Rex, and T. Y. Velikanova, "The Al–B–Nb–Ti system III. Thermodynamic re-evaluation of the constituent binary system Al–Ti," *Journal of Alloys and Compounds*, vol. 465, no. 1–2, pp. 64–77, Oct. 2008.

[85] D. J. Jarvis and D. Voss, "IMPRESS Integrated Project—An overview paper," *Materials Science and Engineering: A*, vol. 413–414, pp. 583–591, Dec. 2005.

[86] R. Mooney, D. Browne, O. Budenkova, Y. Fautrelle, L. Froyen, A. Kartavykh, S. McFadden, S. Rex, B. Schmitz, and D. Voss, "Review of the MAXUS 8 sounding rocket experiment to investigate solidification in a Ti-Al-Nb alloy," in *European Space Agency, (Special Publication) ESA SP*, 2011, vol. 700 SP, pp. 453–458.

[87] R. P. Mooney, S. McFadden, M. Rebow, and D. J. Browne, "A front tracking model of the MAXUS-8 microgravity solidification experiment on a Ti-45.5at.% Al-8at.%Nb alloy," *IOP Conference Series: Materials Science and Engineering*, vol. 27, no. 1, p. 12020, 2012.

[88] F. Lemoisson, S. McFadden, M. Rebow, D. J. Browne, L. Froyen, D. Voss, D. J. Jarvis, A. V. Kartavykh, S. Rex, W. Herfs, D. Groethe, J. Lapin, O. Budenkova, J. Etay, and Y. Fautrelle, "The Development of a Microgravity Experiment Involving Columnar to Equiaxed Transition for Solidification of a Ti-Al Based Alloy," *Materials Science Forum*, vol. 649, pp. 17–22, May 2010.

[89] F. Appel, J. D. H. Paul, and M. Oehring, *Gamma Titanium Aluminide Alloys: Science and Technology*. Weinheim, Germany: Wiley-VCH Verlag GmbH & Co. KGaA, 2011.

[90] F. Appel, M. Oehring, and R. Wagner, "Novel design concepts for gamma-base titanium aluminide alloys," *Intermetallics*, vol. 8, no. 9–11, pp. 1283–1312, Sep. 2000.

[91] H. Nickel, N. Zheng, A. Elschner, and W. J. Quadakkers, "The oxidation behaviour of niobium containing ?-TiAl based intermetallics in air and argon/oxygen," *Mikrochimica Acta*, vol. 119, no. 1–2, pp. 23–39, Mar. 1995.

[92] J. D. Bryant, L. Christodoulou, and J. R. Maisano, "Effect of TiB2 additions on the colony size of near gamma titanium aluminides," *Scripta Metallurgica et Materialia*, vol. 24, no. 1, pp. 33–38, Jan. 1990.

[93]   C. Scheu, E. Stergar, M. Schober, L. Cha, H. Clemens, A. Bartels, F.-P. Schimansky, and A. Cerezo, "High carbon solubility in a γ-TiAl-based Ti–45Al–5Nb–0.5C alloy and its effect on hardening," *Acta Materialia*, vol. 57, no. 5, pp. 1504–1511, Mar. 2009.

[94]   R. R. Boyer, "An overview on the use of titanium in the aerospace industry," *Materials Science and Engineering: A*, vol. 213, no. 1–2, pp. 103–114, 1996.

[95]   W. Voice, "The future use of gamma titanium aluminides by Rolls-Royce," *Aircraft Engineering and Aerospace Technology*, vol. 71, no. 4, pp. 337–340, Jan. 1999.

[96]   "Low density materials," 2014. [Online]. Available: http://www.rolls-royce.com/about/technology/material_tech/low_density_materials.jsp. [Accessed: 10-Apr-2013].

[97]   NASA and Boeing Commercial Airplanes, "(NASA CR-4234) High-Speed Civil Transport Study: Summary," 1989.

[98]   T. Tetsui, "Development of a TiAl turbocharger for passenger vehicles," *Materials Science and Engineering: A*, vol. 329–331, pp. 582–588, Jun. 2002.

[99]   K. Gebauer, "Performance, tolerance and cost of TiAl passenger car valves," *Intermetallics*, vol. 14, no. 4, pp. 355–360, Apr. 2006.

[100] William Kimberley, "EuroAuto: Advanced Material for Racing," *Automotive Design and Production*, Jun-2006.

[101] J. Aguilar, A. Schievenbusch, and O. Kättlitz, "Investment casting technology for production of TiAl low pressure turbine blades – Process engineering and parameter analysis," *Intermetallics*, vol. 19, no. 6, pp. 757–761, Jun. 2011.

[102] S. Biamino, A. Penna, U. Ackelid, S. Sabbadini, O. Tassa, P. Fino, M. Pavese, P. Gennaro, and C. Badini, "Electron beam melting of Ti–48Al–2Cr–2Nb alloy: Microstructure and mechanical properties investigation," *Intermetallics*, vol. 19, no. 6, pp. 776–781, Jun. 2011.

[103] T. Tetsui, K. Shindo, S. Kaji, S. Kobayashi, and M. Takeyama, "Fabrication of TiAl components by means of hot forging and machining," *Intermetallics*, vol. 13, no. 9, pp. 971–978, Sep. 2005.

[104] D. J. Browne, "Advanced Metal Casting Technology," *Transactions of the Institution of Engineers of Ireland*, vol. 18, pp. 20–39, 1993.

[105] M. Wu and A. Ludwig, "Using a Three-Phase Deterministic Model for the Columnar-to-Equiaxed Transition," *Metallurgical and Materials Transactions A*, vol. 38, no. 7, pp. 1465–1475, May 2007.

[106] M. A. Martorano and V. B. Biscuola, "Columnar front tracking algorithm for prediction of the columnar-to-equiaxed transition in two-dimensional solidification," *Modelling and Simulation in Materials Science and Engineering*, vol. 14, no. 7, pp. 1225–1243, Oct. 2006.

[107] A. Jacot, D. Maijer, and S. L. Cockcroft, "A two-dimensional model for the description of the columnar-to-equiaxed transition in competing gray and white iron eutectics and its application to calender rolls," *Metallurgical and Materials Transactions A*, vol. 31, no. 8, pp. 2059–2068, Aug. 2000.

[108] S. G. R. Brown and J. A. Spittle, "Computer simulation of grain growth and macrostructure development during solidification," *Materials Science and Technology*, vol. 5, no. 4, p. 7, 1989.

[109] G. Guillemot, C.-A. Gandin, H. Combeau, and R. Heringer, "A new cellular automaton—finite element coupling scheme for alloy solidification," *Modelling and Simulation in Materials Science and Engineering*, vol. 12, no. 3, pp. 545–556, May 2004.

[110] J. Li, J. Wang, and G. Yang, "Phase-field simulation of microstructure development involving nucleation and crystallographic orientations in alloy solidification," *Journal of Crystal Growth*, vol. 309, no. 1, pp. 65–69, Nov. 2007.

[111] H. B. Dong and P. D. Lee, "Simulation of the columnar-to-equiaxed transition in directionally solidified Al–Cu alloys," *Acta Materialia*, vol. 53, no. 3, pp. 659–668, Feb. 2005.

[112] J. Banaszek, P. Furmański, and M. Rebow, *Modelling of transport phenomena in cooled and solidifying single component and binary media*. Oficyna Wydawnicza Politechniki Warszawskiej, 2005.

[113] S. McFadden and D. J. Browne, "A front-tracking model to predict solidification macrostructures and columnar to equiaxed transitions in alloy castings," *Applied Mathematical Modelling*, vol. 33, no. 3, pp. 1397–1416, Mar. 2009.

[114] D. J. Browne and J. D. Hunt, "A Fixed Grid Front-Tracking Model of the Growth of a Columnar Front and an Equiaxed Grain During Solidification of an Alloy," *Numerical Heat Transfer Part B-Fundamentals*, vol. 45, no. 5, pp. 395–419, May 2004.

[115] R. E. Smallman, "Free energy of transformation," in *Modern Physical Mettalurgy*, Fourth., Butterworth-Heinemann Ltd, 1985.

[116] D. Turnbull and J. C. Fisher, "Rate of Nucleation in Condensed Systems," *The Journal of Chemical Physics*, vol. 17, no. 1, p. 71, Jan. 1949.

[117] L. Greer, "Control of grain size in solidification," in *Solidification and Casting*, B. Cantor and K. O'Reilly, Eds. Bristol: Institute of Physics Publishing, 2003, p. 199247.

[118] T. E. Quested and A. L. Greer, "Grain refinement of Al alloys: Mechanisms determining as-cast grain size in directional solidification," *Acta Materialia*, vol. 53, no. 17, pp. 4643–4653, 2005.

[119] M. H. Burden and J. D. Hunt, "Cellular and Dendritic Growth II," *Journal of Crystal Growth*, vol. 22, pp. 109–116, 1974.

[120] J. Banaszek and D. J. Browne, "Modelling Columnar Dendritic Growth into an Undercooled Metallic Melt in the Presence of Convection," *Materials Transactions*, vol. 46, no. 6, pp. 1378–1387, 2005.

[121] V. R. Voller, "An Overview of Numerical Methods for Solving Phase Change Problems," in *Advances in Numerical Heat Transfer, Volume 1*, W. J. Minkowycz and E. M. Sparrow, Eds. CRC Press, 1997, pp. 341–380.

[122] J. Banaszek, S. McFadden, D. J. Browne, L. Sturz, and G. Zimmermann, "Natural Convection and Columnar-to-Equiaxed Transition Prediction in a Front-Tracking Model of Alloy Solidification," *Metallurgical and Materials Transactions A*, vol. 38, no. 7, pp. 1476–1484, Jun. 2007.

[123] P. Andrzej J. Nowak, M. Seredyński, and J. Banaszek, "Front tracking approach to modeling binary alloy solidification," *International Journal of Numerical Methods for Heat & Fluid Flow*, vol. 24, no. 4, pp. 920–931, 2014.

[124] W. U. Mirihanage, S. McFadden, and D. J. Browne, "Prediction of columnar to equiaxed transition in alloy castings with convective heat transfer and equiaxed grain transportation," in *Shape Casting: 3rd International Symposium 2009*, 2009, pp. 257–264.

[125] A. Ludwig and M. Wu, "Modeling the columnar-to-equiaxed transition with a three-phase Eulerian approach," *Materials Science and Engineering: A*, vol. 413–414, pp. 109–114, Dec. 2005.

[126] R. P. Mooney, S. McFadden, M. Rebow, and D. J. Browne, "A Front Tracking Model for Transient Solidification of Al–7wt%Si in a Bridgman Furnace," *Transactions of the Indian Institute of Metals*, vol. 65, no. 6, pp. 527–530, 2012.

[127] A. Bejan, *Heat Transfer*, 1st ed. New York: John Wiley & Sons, 1993.

[128] F. P. Incropera, D. P. Dewitt, T. L. Bergman, and A. S. Lavine, *Fundamentals of Heat and Mass Transfer*, 6th ed. New York: John Wiley & Sons, 2007.

[129] H. S. Carslaw and J. C. Jaeger, *Conduction of Heat in Solids*, 2nd ed. London: Oxford University Press, 1959.

[130] S. V. Patankar, *Numerical Heat Transfer and Fluid Flow*. McGraw Hill, 1980.

[131] G. De Vahl Davis, "Natural convection of air in a square cavity: A bench mark numerical solution," *International Journal for Numerical Methods in Fluids*, vol. 3, no. 3, pp. 249–264, May 1983.

[132] R. P. Mooney and S. McFadden, "Order verification of a Bridgman furnace front tracking model in steady state," *Simulation Modelling Practice and Theory*, vol. 48, pp. 24–34, 2014.

[133] Oxford University Press, "verification, n.," *OED Online*. [Online]. Available: http://www.oed.com/view/Entry/222504. [Accessed: 08-Aug-2013].

[134] P. Knupp and K. Salari, *Verification of Computer Codes in Computational Science and Engineering*. Boca Raton: CRC Press, 2003.

[135] B. W. Boehm, *Software Engineering Economics*. New Jersey: Prentice-Hall, 1981.

[136] F. G. Blottner, "Accurate Navier-Stokes results for the hypersonic flow over a spherical nosetip," *Journal of Spacecraft and Rockets*, vol. 27, no. 2, pp. 113–122, Mar. 1990.

[137] P. J. Roache, "Verification of Codes and Calculations," *AIAA Journal*, vol. 36, no. 5, pp. 696–702, May 1998.

[138] S. Steinberg and P. J. Roache, "Symbolic manipulation and computational fluid dynamics," *Journal of Computational Physics*, vol. 57, no. 2, pp. 251–284, 1985.

[139] M. N. Özışık, *Finite difference methods in heat transfer*, 1st ed. Boca Raton: CRC Press, 1994.

[140] S. C. Chapra and R. P. Canale, *Numerical Methods for Engineers*, 6th ed. McGraw Hill, 2010.

[141] P. D. Lax and R. D. Richtmyer, "Survey of the stability of linear finite difference equations," *Communications on Pure and Applied Mathematics*, vol. 9, no. 2, pp. 267–293, May 1956.

[142] P. Moin, *Fundamentals of Engineering Numerical Analysis*, 2nd ed. Cambridge University Press, 2010.

[143] MathWorks, "fzero, Root of nonlinear function." [Online]. Available: http://www.mathworks.co.uk/help/matlab/ref/fzero.html. [Accessed: 12-Aug-2013].

[144] R. P. Mooney, S. McFadden, Z. Gabalcová, and J. Lapin, "An experimental–numerical method for estimating heat transfer in a Bridgman furnace," *Applied Thermal Engineering*, vol. 67, no. 1–2, pp. 61–71, 2014.

[145] D. Turnbull and B. G. Bagley, *Treatise on Solid State Chemistry, Vol. 5: Changes of state*. New York: Plenum, 1975.

[146] M. Banan, R. T. Gray, and W. R. Wilcox, "An experimental approach to determine the heat transfer coefficient in directional solidification furnaces," *Journal of Crystal Growth*, vol. 113, no. 3–4, pp. 557–565, 1991.

[147] W. Rosch, W. Jesser, W. Debnam, A. Fripp, G. Woodell, and T. K. Pendergrass, "A technique for measuring the heat transfer coefficient inside a Bridgman furnace," *Journal of Crystal Growth*, vol. 128, no. 1–4 part 2, pp. 1187–1192, 1993.

[148] W. Rosch, A. Fripp, W. Debnam, and T. K. Pendergrass, "Heat transfer measurements in the Bridgman configuration," *Journal of Crystal Growth*, vol. 137, no. 1–2, pp. 54–58, 1994.

[149] D. M. L. Bartholomew and A. Hellawell, "Changes of growth conditions in the vertical Bridgman-Stockbarger method for the solidification of aluminum," *Journal of Crystal Growth*, vol. 50, no. 2, pp. 453–460, Oct. 1980.

[150] S. Sen and W. R. Wilcox, "Influence of crucible on interface shape, position and sensitivity in the vertical Bridgman-Stockbarger technique," *Journal of Crystal Growth*, vol. 28, no. 1, pp. 36–40, Jan. 1975.

[151] P. C. Sukanek, "Deviation of freezing rate from translation rate in the Bridgman-Stockbarger technique I. Very low translation rates," *Journal of Crystal Growth*, vol. 58, no. 1, pp. 208–218, Jun. 1982.

[152] J. Lapin and Z. Gabalcová, "Solidification behaviour of TiAl-based alloys studied by directional solidification technique," *Intermetallics*, vol. 19, no. 6, pp. 797–804, Jun. 2011.

[153] J. M. Kay and R.M. Nedderman, *Fluid mechanics and transfer processes*. Cambridge University Press, 1985.

[154] H. R. N. Jones, *Radiation heat transfer*. Oxford University Press, 2000.

[155] MathWorks, "Piecewise Cubic Hermite Interpolating Polynomial (PCHIP)." [Online]. Available: http://www.mathworks.co.uk/help/matlab/ref/pchip.html. [Accessed: 16-Aug-2013].

[156] M. N. Özışık and H. R. B. Orlande, *Inverse Heat Transfer: Fundamentals and Applications*. New York: Taylor & Francis, 2000.

[157] A. N. Tikhonov and V. Y. Arsenin, *Solutions of ill posed problems*. Washington, D.C.: Wiley, 1977.

[158] O. M. Alifanov, "Solution of an inverse problem of heat conduction by iteration methods," *Journal of Engineering Physics and Thermophysics*, vol. 26, no. 4, pp. 471–476, Apr. 1974.

[159] J. V. Beck, B. Blackwell, and C. R. St. Clair Jr., *Inverse heat conduction: ill-posed problems*. New York: Wiley, 1985.

[160] D. E. Seborg, D. A. Mellichamp, T. F. Edgar, and F. J. Doyle III, *Process Dynamics and Control*, 3rd ed. Wiley, 2011.

[161] J. G. Ziegler and N. B. Nichols, "Optimum settings for automatic controllers," *Transactions of the ASME*, vol. 64, pp. 759–768, 1942.

[162] I. Egry, R. Brooks, D. Holland-Moritz, R. Novakovic, T. Matsushita, E. Ricci, S. Seetharaman, R. Wunderlich, and D. Jarvis, "Thermophysical Properties of γ-Titanium Aluminide: The European IMPRESS Project," *International Journal of Thermophysics*, vol. 28, no. 3, pp. 1026–1036, Aug. 2007.

[163] Y. S. Touloukian, R. W. Powell, C. Y. Ho, and P. G. Klemens, *Thermophysical Properties of Matter: Vol 2 Thermal Conductivity Nonmetallic Solids*. New York-Washington: IFI/Plenum, 1970.

[164] M. Rebow, D. J. Browne, and Y. Fautrelle, "Combined Analytical and Numerical Front Tracking Approach to Modeling Directional Solidification of a TiAl-Based Intermetallic Alloy for Design of Microgravity Experiments," *Materials Science Forum*, vol. 649, pp. 243–248, Aug. 2010.

[165] Thermo-Calc Software AB, "Thermo-Calc 3.0," 2013. [Online]. Available: http://www.thermocalc.com/Thermo-Calc.htm. [Accessed: 26-Feb-2013].

[166] Q. Chen and B. Sundman, "Computation of partial equilibrium solidification with complete interstitial and negligible substitutional solute back diffusion," *Materials Transactions JIM*, vol. 43, no. 3, pp. 551–559, 2002.

[167] T.-W. Fu, W. R. Wilcox, and D. J. Larson, "Rate change transients in Bridgman-Stockbarger growth of MnBi-Bi eutectic," *Journal of Crystal Growth*, vol. 57, no. 1, pp. 189–193, 1982.

[168] R. Trivedi, A. Karma, T. S. Lo, P. Mazumder, J. S. Park, and M. Plapp, "Dynamic Pattern Formation in the Two-Phase Region of Peritectic Systems," in *2nd Workshop on Solidification Microstructures*, 1998.

[169] D. M. Anderson, G. B. McFadden, S. R. Coriell, and B. T. Murray, "Convective instabilities during the solidification of an ideal ternary alloy in a mushy layer," *Journal of Fluid Mechanics*, vol. 647, p. 309, Mar. 2010.

[170] R. P. Mooney, U. Hecht, Z. Gabalcová, J. Lapin, and S. McFadden, "Numerical modelling of axial heat transfer and columnar growth in power down experiments using a TiAl alloy," *(submitted)*, 2014.

[171] A. V Kartavykh, V. P. Ginkin, and S. M. Ganina, "Numerical modeling of power-down directional solidification process of Ti–46Al–8Nb refractory alloy," *Journal of Alloys and Compounds*, no. 0, p. -, 2012.

[172] M. A. Martorano, J. B. F. Neto, T. S. Oliveira, and T. O. Tsubaki, "Refining of metallurgical silicon by directional solidification," *Materials Science and Engineering: B*, vol. 176, no. 3, pp. 217–226, Feb. 2011.

[173] H. Müller-Krumbhaar and J. S. Langer, "Sidebranching instabilities in a two-dimensional model of dendritic solidification," *Acta Metallurgica*, vol. 29, no. 1, pp. 145–157, Jan. 1981.

[174] C. Misbah, "Velocity selection for needle crystals in the 2-D one-sided model," *Journal de Physique Paris*, vol. 48, no. 8, pp. 1255–1263, 1987.

[175] R. P. Mooney and S. McFadden, "Sensitivity analysis of dendritic growth kinetics in a Bridgman furnace front tracking model," in *4th International Conference on Advances in Solidification Processes*, 2014.

[176] A. Badillo and C. Beckermann, "Phase-field simulation of the columnar-to-equiaxed transition in alloy solidification," *Acta Materialia*, vol. 54, no. 8, pp. 2015–2026, 2006.

[177] G. B. McFadden and S. R. Coriell, "Thermosolutal convection during directional solidification. II. Flow transitions," *Physics of Fluids*, vol. 30, no. 3, p. 659, Mar. 1987.

[178] C. J. Chang and R. A. Brown, "Radial segregation induced by natural convection and melt/solid interface shape in vertical bridgman growth," *Journal of Crystal Growth*, vol. 63, no. 2, pp. 343–364, Oct. 1983.

[179] A. Kartavykh, V. Ginkin, S. Ganina, S. Rex, U. Hecht, B. Schmitz, and D. Voss, "Convection-induced peritectic macro-segregation proceeding at the directional solidification of Ti–46Al–8Nb intermetallic alloy," *Materials Chemistry and Physics*, vol. 126, no. 1–2, pp. 200–206, Mar. 2011.

[180] M. F. Zhu and C. P. Hong, "A Modified Cellular Automaton Model for the Simulation of Dendritic Growth in Solidification of Alloys," *ISIJ International*, vol. 41, no. 5, pp. 436–445, 2001.

[181] S. L. Cockcroft, M. Rappaz, A. Mitchell, J. Fernihough, and A. J. Schmaltz, "An Examination of Some of the Manufacturing Problems of Large Single-Crystal Turbine Blades for use in Land-Based Gas Turbines," in *Materials for Advanced Power Engineering, Part II*, D. Coutsouradis, J. H. Davidson, J. Ewald, P. Greenfield, T. Khan, M. Malik, D. B. Meadowcroft, V. Regis, R. B. Scarlin, F. Schubert, and D. V. Thornton, Eds. Dordrecht, Netherlands: Kluwer Academic Publishers, 1994, pp. 1145–1154.

[182] "CMSX-4." [Online]. Available: http://www.c-mgroup.com/spec_sheets/CMSX_4.htm. [Accessed: 22-Jul-2014].

[183] O. Hunziker, "Theory of plane front and dendritic growth in multicomponent alloys," *Acta Materialia*, vol. 49, no. 20, pp. 4191–4203, Dec. 2001.

[184] D. Kessler and H. Levine, "Velocity selection in dendritic growth," *Physical Review B*, vol. 33, no. 11, pp. 7867–7870, Jun. 1986.

[185] M. Schmachtl, A. Schievenbusch, G. Zimmermann, and W. Grill, "Crystallization process control during directional solidification in a high-temperature-gradient furnace by guided

ultrasonic waves and real-time signal evaluation," *Ultrasonics*, vol. 36, no. 1–5, pp. 291–295, Feb. 1998.

[186] J. D. Miller and T. M. Pollock, "Stability of dendrite growth during directional solidification in the presence of a non-axial thermal field," *Acta Materialia*, vol. 78, pp. 23–36, Oct. 2014.

Appendix

A.1   Derivation of the 1-Dimensional Heat Flow Equation

      Adapted from Bejan [127]; consider a cylindrical rod of constant cross sectional area A, and radius r, having a fixed density ρ, and moving at a rate u along its axis, through a fixed cylindrical elemental volume of thickness Δx, and volume, V, as shown in Fig. A.1. The elemental volume is gaining heat radially, Q_{rad}, through its curved surface area A_{rad}, and heat is being internally generated due to the release of latent energy from a solidification process, Q_{latent}. Considering net heat by conduction (diffusion of heat); heat enters the volume at its west face, Q_x, and is leaving the volume at its east face, $Q_{x+\Delta x}$. Considering sensible energy carried by the moving mass (advection of heat); heat is advected into the volume at its west face, $\dot{m}cT_x$, and advected out of the volume at its east face, $\dot{m}cT_{x+\Delta x}$, where $\dot{m}$ is the mass flow rate of the rod through the volume, i.e., $\dot{m}=\rho Au$, where c is the specific heat capacity of the rod material, and T is the temperature of the rod at the west face T_x, or at the east face $T_{x+\Delta x}$.
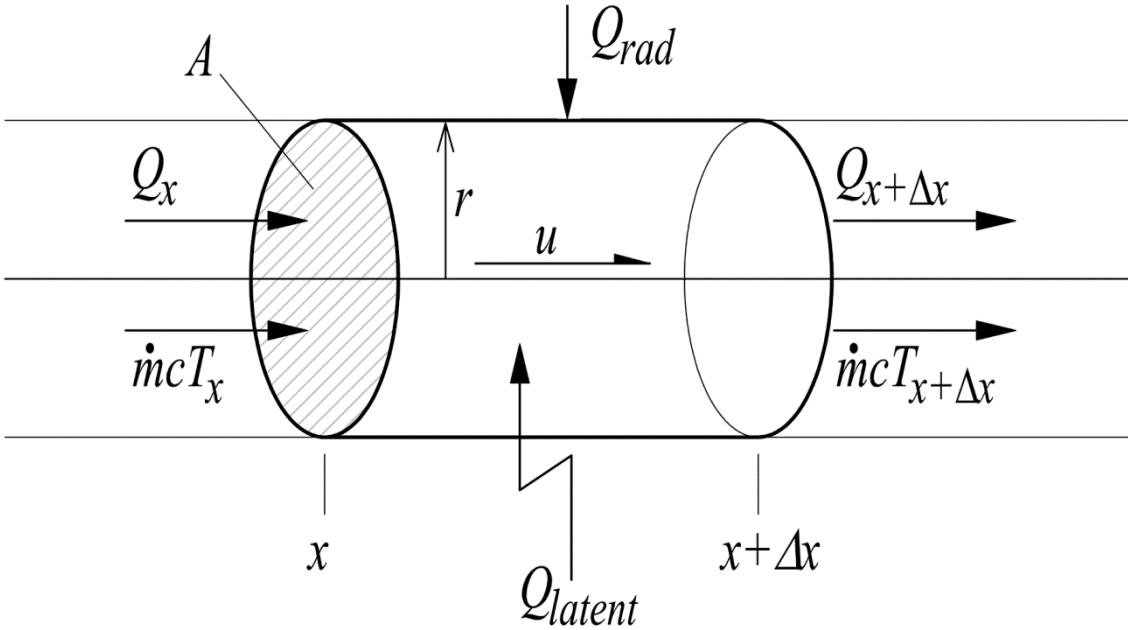

Fig. A.1 Conservation of energy in a cylindrical elemental fixed volume.

By conservation of energy in the elemental fixed volume;

Time rate of change of energy in the volume = Sum of heat energies acting on the volume

$$\frac{\partial}{\partial t}(\rho cT)V = Q_x - Q_{x+\Delta x} + \dot{m}cT_x - \dot{m}cT_{x+\Delta x} + Q_{rad} + Q_{latent} \quad , \tag{A.1}$$

By Fourier's law; $\quad Q_x = -kA\dfrac{dT}{dx}\Big|_x \quad$ and $\quad Q_{x+\Delta x} = -kA\dfrac{dT}{dx}\Big|_{x+\Delta x}$

so that, $\quad Q_x - Q_{x+\Delta x} = -\dfrac{dQ_x}{dx}\Delta x \quad$ and $\quad Q_x - Q_{x+\Delta x} = -\dfrac{d}{dx}\left(-kA\dfrac{dT}{dx}\right)\Delta x \quad .$

Sensible energy terms; $\dot{m}cT_x - \dot{m}cT_{x+\Delta x} = -\dot{m}c\dfrac{dT}{dx}\Delta x \quad .$

Latent heat term; $\quad Q_{latent} = \rho L_M \dfrac{\partial V_S}{\partial t} \quad ,$ where L_M is the latent heat of fusion per unit mass

for the material, and V_S is the volume of material solidified.

The radial heat term; $\quad Q_{rad} = A_{rad}q_{rad} \quad ,$ where $A_{rad}=2\pi r\Delta x$ and q_{rad} is the radial heat flux.

Now, substitute into the conservation equation, assuming a fixed density, fixed heat capacity, and a fixed mass flow rate;

$$\rho c\frac{\partial T}{\partial t}A\Delta x = \frac{\partial}{\partial x}\left(k\frac{\partial T}{\partial x}\right)A\Delta x - \rho Auc\frac{\partial T}{\partial x}\Delta x + 2\pi r\Delta x q_{rad} + \rho L_M\frac{\partial V_S}{\partial t} \quad . \qquad \text{(A.2)}$$

Divide across by, $A\Delta x$;

$$\rho c\frac{\partial T}{\partial t} = \frac{\partial}{\partial x}\left(k\frac{\partial T}{\partial x}\right) - \rho uc\frac{\partial T}{\partial x} + \frac{2\pi r}{A}q_{rad} + \frac{\rho L_M}{A\Delta x}\frac{\partial V_S}{\partial t} \quad . \qquad \text{(A.3)}$$

Since, $A=\pi r^2$, and defining E as latent heat released per unit volume, p as the volume perimeter, and $q_{rad}=-h(T-T_\infty)$, yielding;

$$\frac{\partial}{\partial t}(\rho cT) = \frac{\partial}{\partial x}\left(k\frac{\partial T}{\partial x}\right) - u\rho c\frac{\partial T}{\partial x} - \frac{hp}{A}(T-T_\infty) + E \quad . \qquad \text{(A.4)}$$

A.2 Discretisation of the 1-Dimensional Heat Flow Equation

As per Section 3.2.1, the heat equation for 1-dimensionsal heat flow in a moving rod is given by equation (3.2) as follows:

$$\frac{\partial}{\partial t}(\rho c T) = \frac{\partial}{\partial x}\left(k\frac{\partial T}{\partial x}\right) - u\rho c\frac{\partial T}{\partial x} - \frac{hp}{A}(T - T_\infty) + E \quad . \tag{A.5}$$

The control volume method [139] is applied to develop finite difference equations.
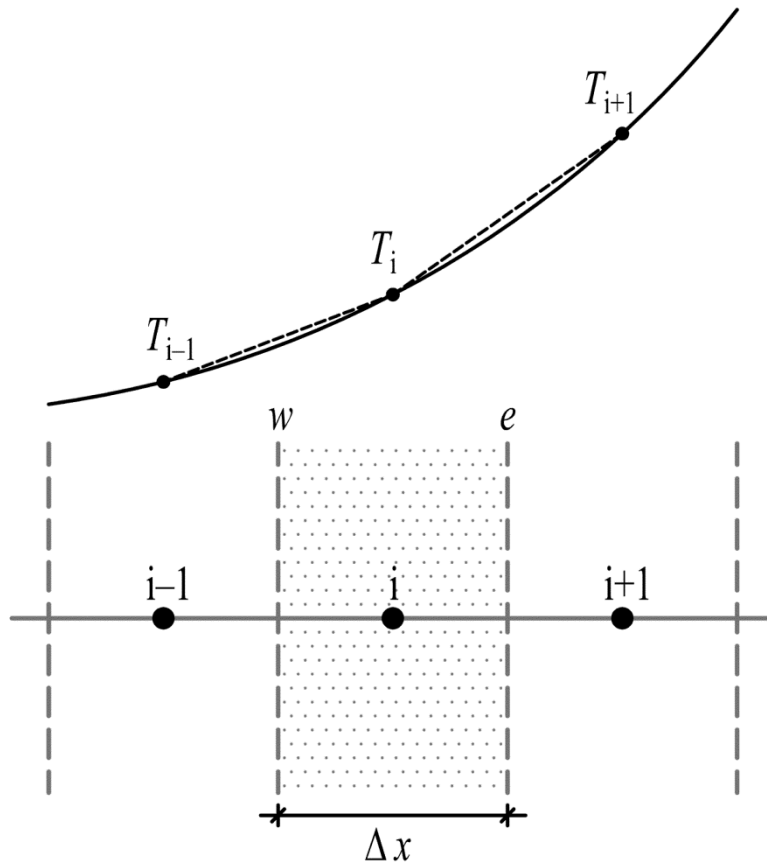

Fig. A.2 Control volume 'i'.

The heat equation is integrated over a cylindrical-shaped control volume ('i' in figure A.2) giving,

$$\overbrace{\int_{V_{CV}}\frac{\partial}{\partial t}(\rho c T)dV_{CV}}^{1} = \overbrace{\int_{V_{CV}}\frac{\partial}{\partial x}\left(k\frac{\partial T}{\partial x}\right)dV_{CV}}^{2} - \overbrace{\int_{V_{CV}}u\rho c\frac{\partial T}{\partial x}dV_{CV}}^{3} - \overbrace{\int_{V_{CV}}\frac{hp}{A}(T - T_\infty)dV_{CV}}^{4} + \overbrace{\int_{V_{CV}}EdV_{CV}}^{5} \quad . \tag{A.6}$$

The mean value theorem is applied to integrals 1, 4, and 5. This means that an average value is taken for each variable being integrated; denoted below by a bar ($^-$) over the averaged variable. The divergence theorem is applied to integrals 2 and 3. This converts a volume integral to a surface integral. The surface (S) over which the integration takes place is that through which heat is

132

permitted to flow into or out of the CV by diffusion (integral 2) and advection (integral 3), i.e., through the east and west faces of the CV, each having surface area A. This leads to the following form of the heat equation,

$$\rho c \frac{\partial \overline{T}}{\partial t} V_{CV} = \int\limits_{S\ w}^{e} k \frac{\partial T}{\partial x} dS - u\rho c \int\limits_{S\ w}^{e} T dS - \frac{hp}{A} \left(\overline{T} - T_\infty \right) V_{CV} + \overline{E} V_{CV} \quad , \tag{A.7}$$

where the sub-scripts 'e' and 'w' denote the east and west faces of the CV, respectively. Evaluating the integrals yields,

$$\rho c \frac{\partial \overline{T}}{\partial t} V_{CV} = \left\{ \left[k \frac{\partial T}{\partial x} \right]_e - \left[k \frac{\partial T}{\partial x} \right]_w \right\} A - u\rho c \left[T_e - T_w \right] A - \frac{hp}{A} \left(\overline{T} - T_\infty \right) V_{CV} + \overline{E} V_{CV} \quad , \tag{A.8}$$

Equation (A.8) is equivalent to equation (4.23), noting that; T_∞ and h are used in place of $T_{H,C}$ and $h_{H,C}$, respectively, and that, the final term on the RHS of both equations are equal. Next, Taylor series' expansions are introduced in place of the partial derivative terms giving,

$$\rho c \left[\frac{\left(T_i^{m+1} - T_i^m \right)}{\Delta t} + O(\Delta t) \right] V_{CV} = \left\{ k \left[\frac{T_{i+1} - T_i}{\Delta x} + O(\Delta x)^2 \right] - k \left[\frac{T_i - T_{i-1}}{\Delta x} + O(\Delta x)^2 \right] \right\} A ...$$
$$... - u\rho c (T_e - T_w) A - \frac{hp}{A} (T_i - T_\infty) V_{CV} + \overline{E} V_{CV} \tag{A.9}$$

In this equation, a *forward difference* approximation {equation (A.17)} is applied for the time derivative terms (having first order accuracy), and a *central difference* approximation {equation (A.24) and equation (A.25)} is used for the spatial derivative terms (having second order accuracy); see Appendix A.3 for details of these approximations. Divide by $V_{CV}=A\Delta x$ to get,

$$\rho c \left[\frac{\left(T_i^{m+1} - T_i^m \right)}{\Delta t} + O(\Delta t) \right] = \left\{ k \left[\frac{T_{i+1} - T_i}{(\Delta x)^2} + O(\Delta x)^2 \right] - k \left[\frac{T_i - T_{i-1}}{(\Delta x)^2} + O(\Delta x)^2 \right] \right\} ...$$
$$... - \frac{u\rho c}{\Delta x} (T_e - T_w) - \frac{hp}{A} (T_i - T_\infty) + \overline{E} \tag{A.10}$$

Rearranging gives,

$$\rho c \left[\frac{\left(T_i^{m+1} - T_i^m \right)}{\Delta t} + O(\Delta t) \right] = k \left[\frac{T_{i-1} + 2T_i - T_{i+1}}{(\Delta x)^2} + O(\Delta x)^2 \right] - u\rho c \frac{(T_e - T_w)}{\Delta x} - \frac{hp}{A} (T_i - T_\infty) + \overline{E} \quad , \tag{A.11}$$

133

Equation (A.11) is corresponds to equation (4.24) noting that, as before, T_∞ and h are used in place of with $T_{H,C}$ and $h_{H,C}$, respectively. The final term on the RHS of each equation is equivalent, and is evaluated as $\overline{E} = \rho L_M (\partial V_S / \partial t)$ with $\partial V_S/\partial t = g_S(\partial d/\partial t) + d(\partial g_S/\partial t)$. The partial derivative terms, that comprise $\partial V_S/\partial t$, are estimated using forward difference Taylor series approximations (having first order accuracy) as follows:

$$\frac{\partial V_S}{\partial t} = g_S \left[\frac{\left(d_i^{m+1} - d_i^m\right)}{\Delta t} + O(\Delta t) \right] + d \left[\frac{\left(g_{S_i}^{m+1} - g_{S_i}^m\right)}{\Delta t} + O(\Delta t) \right] \quad . \tag{A.12}$$

When all the Taylor series' truncation error terms are dropped from equation (A.11) it can be rearranged as follows:

$$\frac{\rho c \Delta x}{\Delta t} \left(T_i^{m+1} - T_i^m\right) = k \frac{(T_{i+1} - T)_i}{\Delta x} + k \frac{(T_{i-1} - T_i)}{\Delta x} - \frac{u \rho c}{2}\left(T_{i+1} - T_{i-1}\right)...$$
$$... - \Delta x \frac{2}{r} h_{H,C}\left(T_i - T_{H,C}\right) + \frac{\rho L_M}{V_{CV}} g_S^m \frac{\left(d_i^{m+1} - d_i^m\right)}{\Delta t} \Delta x + \frac{\rho L_M}{V_{CV}} d^m \frac{\left(g_{S_i}^{m+1} - g_{S_i}^m\right)}{\Delta t} \Delta x \quad , \tag{A.13}$$

where $P/A = 2/r$, $T_e - T_w = (T_{i+1} - T_{i-1})/2$, T_∞ is replaced with $T_{H,C}$, and h is replaced with $h_{H,C}$. Equation (A.13) corresponds to equation (3.4), reproduced below, recalling from Chapter 3 that, $r = r_2$ and q_2 is the radial heat flux at the circumference of the CV.

$$\frac{\rho c \Delta x}{\Delta t} \left(T_i^{m+1} - T_i^m\right) = q_{i-1} + q_{i+1} + q_{adv} + \Delta x \frac{2}{r_2} q_2 + q_a + q_t \quad . \tag{A.14}$$

A.3 Taylor Series Formulations for First Order Derivatives

Consider Taylor series expansions of a function $f(x)$ about a point x_0 in the *forward* (i.e., positive x) and *backward* (i.e., negative x) directions, respectively,

$$f(x_0 + \Delta x) = f(x_0) + \frac{df}{dx}\bigg|_{x_0}.\Delta x + \frac{d^2 f}{dx^2}\bigg|_{x_0}.\frac{(\Delta x)^2}{2!} + \frac{d^3 f}{dx^3}\bigg|_{x_0}.\frac{(\Delta x)^3}{3!} + \frac{d^4 f}{dx^4}\bigg|_{x_0}.\frac{(\Delta x)^4}{4!} + ... \quad , \quad (A.15)$$

$$f(x_0 - \Delta x) = f(x_0) - \frac{df}{dx}\bigg|_{x_0}.\Delta x + \frac{d^2 f}{dx^2}\bigg|_{x_0}.\frac{(\Delta x)^2}{2!} - \frac{d^3 f}{dx^3}\bigg|_{x_0}.\frac{(\Delta x)^3}{3!} + \frac{d^4 f}{dx^4}\bigg|_{x_0}.\frac{(\Delta x)^4}{4!} + ... \quad , \quad (A.16)$$

where Δx is the size of the step forward, or backward, from x_0. Rearranging the first expression for df/dx about x_0 gives the *forward difference* approximation for the first derivative of the function $f(x)$ as follows:

$$\frac{df}{dx}\bigg|_{x_0} = \frac{f(x_0 + \Delta x) - f(x_0)}{\Delta x} + O(\Delta x) \quad , \quad (A.17)$$

where,

$$O(\Delta x) = \frac{d^2 f}{dx^2}\bigg|_{x_0}.\frac{\Delta x}{2!} + \frac{d^3 f}{dx^3}\bigg|_{x_0}.\frac{(\Delta x)^2}{3!} + \frac{d^4 f}{dx^4}\bigg|_{x_0}.\frac{(\Delta x)^3}{4!} + ... \quad . \quad (A.18)$$

The "order of" notation, $O(\Delta x)$, characterises the truncation error for the finite difference approximation. This is the difference between the actual derivate and the value given by the approximation. In this case, the approximation is first order accurate.

Subtracting the *backward* direction Taylor series expansion from the *forward* direction Taylor series expansion gives the *central difference* approximation for the first derivative of the function $f(x)$ as follows:

$$f(x_0 + \Delta x) - f(x_0 - \Delta x) = 2\frac{df}{dx}\bigg|_{x_0}.\Delta x + 2\frac{d^3 f}{dx^3}\bigg|_{x_0}.\frac{(\Delta x)^3}{3!} + 2\frac{d^5 f}{dx^5}\bigg|_{x_0}.\frac{(\Delta x)^5}{5!} + ... \quad . \quad (A.19)$$

Rearranging the for df/dx about x_0 gives,

$$\frac{df}{dx}\bigg|_{x_0} = \frac{f(x_0 + \Delta x) - f(x_0 - \Delta x)}{2\Delta x} + O(\Delta x)^2 \quad , \quad (A.20)$$

where,

$$O(\Delta x)^2 = -\frac{d^3 f}{dx^3}\bigg|_{x_0}.\frac{(\Delta x)^2}{3!} - \frac{d^5 f}{dx^5}\bigg|_{x_0}.\frac{(\Delta x)^4}{5!} - ... \quad . \quad (A.21)$$

In this case, the approximation is second order accurate.

In Appendix A.2, the approximation to the first derivative of temperature with respect to x at the east and west faces of a CV {see figure A.2 and equation (A.9)} is made using the *central difference* formula where with the size of the step forward, and backward, from the CV face to the next CV node centre is equal to $\Delta x/2$. The appropriate formula in this case is determined by substituting $\Delta x/2$ for Δx in equation (A.20) to give,

$$\left.\frac{df}{dx}\right|_{x_0} = \frac{f(x_0 + \Delta x/2) - f(x_0 - \Delta x/2)}{\Delta x} + O(\Delta x)^2 \quad , \tag{A.22}$$

where,

$$O(\Delta x)^2 = -\left.\frac{d^3 f}{dx^3}\right|_{x_0} \cdot \frac{(\Delta x)^2}{24} - \left.\frac{d^5 f}{dx^5}\right|_{x_0} \cdot \frac{(\Delta x)^4}{1920} - \cdots \quad , \tag{A.23}$$

so that, in terms of the CV arrangement shown in figure A.2, the central difference approximation for the spatial first derivatives at the east and west faces of the CV are given by,

$$\left.\frac{\partial T}{\partial x}\right|_e = \frac{T_{i+1} - T_i}{\Delta x} + O(\Delta x)^2 \quad , \tag{A.24}$$

and

$$\left.\frac{\partial T}{\partial x}\right|_w = \frac{T_i - T_{i-1}}{\Delta x} + O(\Delta x)^2 \quad , \tag{A.25}$$

respectively.

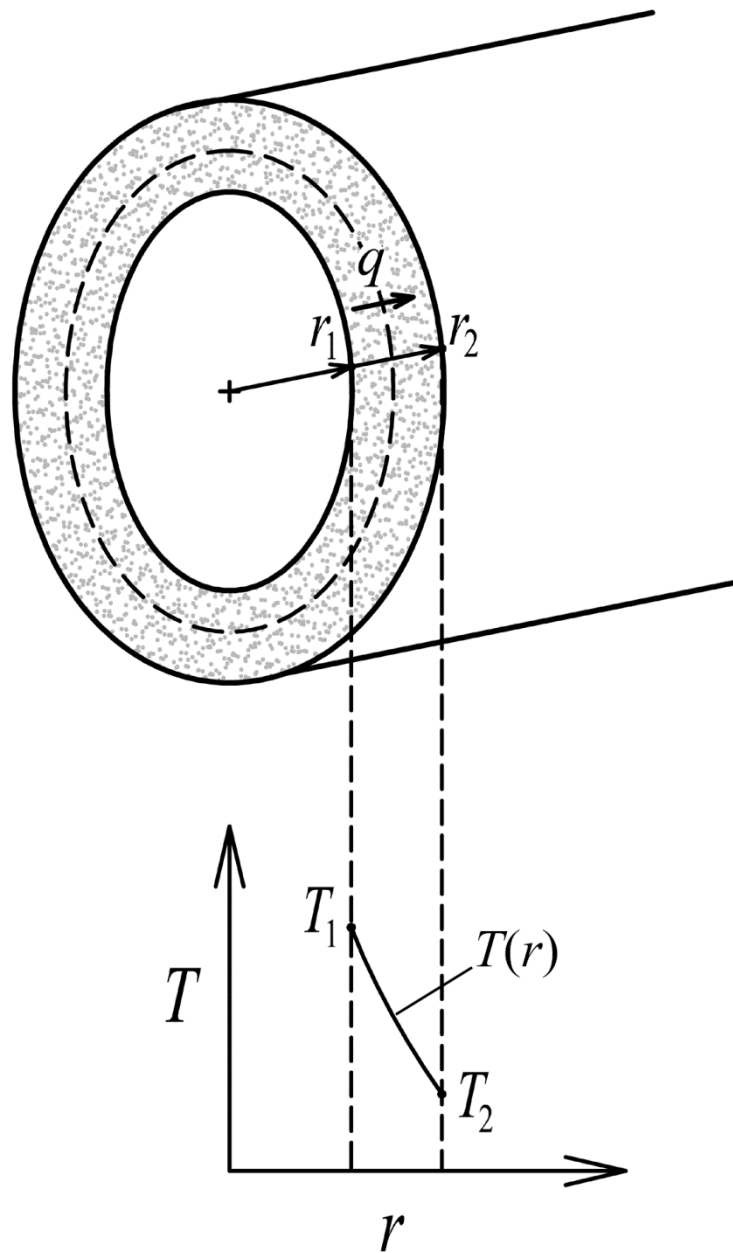## A.4 Radial Heat Flow in a Pipe (Crucible)

Fig. A.3 Heat flow in a pipe.

Consider steady-state radial heat flow (Q) in a solid pipe, with no internal heat generation, as shown in figure A.3. For continuity,

$$Q = 2\pi r L q \quad , \tag{A.26}$$

where L is the pipe length and q is the radial heat flux in the pipe at any radius r. Apply Fourier's law to give,

$$q = \frac{Q}{2\pi r L} = -k \frac{dt}{dr} \quad . \tag{A.27}$$

Integrate from r_1 to r_2,

$$\int_{r_1}^{r_2} \frac{Q}{2\pi r L} dr = \int_{r_1}^{r_2} -k \frac{dt}{dr} dr \quad . \tag{A.28}$$

$$\frac{Q}{2\pi L} [\ln r]_{r_1}^{r_2} = -k[T]_{r_1}^{r_2} \quad . \tag{A.29}$$

$$\frac{Q}{2\pi L} \ln \frac{r_2}{r_1} = k(T_1 - T_2) \quad . \tag{A.30}$$

Rearrange for T_2 with $Q=2\pi r_2 L q_2$, giving,

$$T_2 = T_1 - q_2 r_2 \frac{\ln(r_2/r_1)}{k} \quad . \tag{A.31}$$

Also, rearrange equation (A.30) for Q,

$$Q = \frac{2\pi L k(T_1 - T_2)}{\ln(r_2/r_1)} \quad . \tag{A.32}$$

$$q = \frac{k(T_1 - T_2)}{\ln(r_2/r_1)} \cdot \frac{1}{r} \quad , \tag{A.33}$$

since, $Q=2\pi r L q$. Equation (A.33) is gives q at any radius r.

To get $T(r)$, in equation (A.30) replace r_2 with r to get,

$$\frac{Q}{2\pi L} \ln \frac{r}{r_1} = k(T_1 - T(r)) \quad , \tag{A.34}$$

and divide by equation (A.30) to get,

$$\frac{T_1 - T(r)}{T_1 - T_2} = \frac{\ln(r/r_1)}{\ln(r_2/r_1)} \quad . \tag{A.35}$$